



Advanced Engineering Research

Theoretical and scientific-practical journal

Vol. **21**

ISSN 2687-1653 

no. **1**
2021

1

Mechanics

2

Machine Building and Machine Science

3

Information Technology, Computer Science, and Management

DOI 10.23947/2687-1653

vestnik-donstu.ru

Advanced Engineering Research

Vol. 21, no. 1

**Theoretical
and scientific-practical journal**

Published since 1999

4 issues a year
January-March 2021

ISSN 2687-1653
DOI: 10.23947/2687-1653

**Founder and publisher — Federal State Budgetary Educational Institution of Higher Education
Don State Technical University (DSTU)**

The journal was known as Vestnik of Don State Technical University (until August 2020)

Included in the list of peer-reviewed scientific editions where the basic research results of doctoral, candidate's theses should be published (State Commission for Academic Degrees and Titles List) in the following research areas:

01.02.01 – Analytical Mechanics (Engineering Sciences)
01.02.04 – Deformable Solid Mechanics (Engineering Sciences)
01.02.04 – Deformable Solid Mechanics (Physicomathematical Sciences)
01.02.06 – Dynamics, Strength of Machines, Gear, and Equipment (Engineering Sciences)
05.02.02 – Engineering Science, Drive Systems and Machine Parts (Engineering Sciences)
05.02.04 – Machine Friction and Wear (Engineering Sciences)
05.02.07 – Technology and Equipment of Mechanical and Physicotechnical Processing (Engineering Sciences)
05.02.08 – Engineering Technology (Engineering Sciences)
05.02.10 – Welding, Allied Processes and Technologies (Engineering Sciences)
05.02.11 – Testing Methods and Diagnosis in Machine Building (Engineering Sciences)
05.13.11 – Software and Mathematical Support of Machines, Complexes and Computer Networks (Engineering Sciences)
05.13.17 – Foundations of Information Science (Engineering Sciences)
05.13.18 – Mathematical Simulation, Numerical Methods and Program Systems (Engineering Sciences)

**The journal is indexed and archived in the Russian Science Citation Index (RSCI),
and in EBSCO International Database**

The journal is a member of Directory of Open Access Journals (DOAJ), Association of Science Editors and Publishers (ASEP) and Cross Ref

Certificate of mass media registration ЭЛ № ФС 77 – 78854 of 07.08.2020 is issued by the Federal Service for Supervision of Communications, Information Technology, and Mass Media

The issue is prepared by:

Inna V. Boyko, Gennady I. Rassokhin, Marina P. Smirnova (English version)

Founder's, Publisher's and Printery Address:

Gagarin Sq. 1, Rostov-on-Don, 344003, Russia. Phone: +7 (863) 2-738-372

E-mail: vestnik@donstu.ru <http://vestnik-donstu.ru/>



The content is available under Creative Commons Attribution 4.0 License

Editorial Board

Editor-in-Chief — **Besarion Ch. Meskhi**, Dr.Sci. (Eng.), professor, Don State Technical University (Russian Federation);
deputy chief editor — **Valery P. Dimitrov**, Dr.Sci. (Eng.), professor, Don State Technical University (Russian Federation);
executive editor — **Manana G. Komakhidze**, Cand.Sci. (Chemistry), Don State Technical University (Russian Federation);
executive secretary — **Nadezhda A. Shevchenko**, Don State Technical University (Russian Federation);

Evgeny V. Ageev, Dr.Sci. (Eng.), professor, South-Western State University (Russian Federation);
Sergey M. Aizikovich, Dr.Sci. (Phys.-Math.), professor, Don State Technical University (Russian Federation);
Kamil S. Akhverdiev, Dr.Sci. (Eng.), professor, Rostov State Transport University (Russian Federation);
Vladimir I. Andreev, member of RAACS, Dr.Sci. (Eng.), professor, National Research Moscow State University of Civil Engineering (Russian Federation);
Imad R. Antipas, Cand.Sci. (Eng.), Don State Technical University (Russian Federation);
Torsten Bertram, Dr.Sci. (Eng.), professor, TU Dortmund University (Germany);
Dmitry A. Bezuglov, Dr.Sci. (Eng.), professor, Rostov branch of Russian Customs Academy (Russian Federation);
Larisa V. Cherkesova, Dr.Sci. (Phys. -Math.), professor, Don State Technical University (Russian Federation);
Alexandr N. Chukarin, Dr.Sci. (Eng.), professor, Rostov State Transport University (Russian Federation);
Oleg V. Dvornikov, Dr.Sci. (Eng.), professor, Belarusian State University (Belarus);
Karen O. Egiazyryan, Dr.Sci. (Eng.), professor, Tampere University of Technology (Tampere, Finland);
Sergey V. Eliseev, corresponding member of Russian Academy of Natural History, Dr.Sci. (Eng.), professor, Irkutsk State Railway Transport Engineering University (Russian Federation);
Victor A. Eremeev, Dr.Sci. (Phys.-Math.), professor, Southern Scientific Center of RAS (Russian Federation);
Mikhail B. Flek, Dr.Sci. (Eng.), professor, "Rostvertol" JSC (Russian Federation);
Nikolay E. Galushkin, Dr.Sci. (Eng.), professor, Institute of Service and Business (DSTU branch) (Russian Federation);
LaRoux K. Gillespie, Dr.Sci. (Eng.), professor, President-elect of the Society of Manufacturing Engineers (USA);
Anatoly A. Korotkii, Dr.Sci. (Eng.), professor, Don State Technical University (Russian Federation);
Victor M. Kureychik, Dr.Sci. (Eng.), professor, Southern Federal University (Russian Federation);
Geny V. Kuznetzov, Dr.Sci. (Phys.-Math.), professor, Tomsk Polytechnic University (Russian Federation);
Vladimir I. Lysak, Dr.Sci. (Eng.), professor, Volgograd State Technical University, (Russian Federation);
Vladimir I. Marchuk, Dr.Sci. (Eng.), professor, Institute of Service and Business (DSTU branch) (Shakhty);
Igor P. Miroshnichenko, Cand.Sci. (Eng.), professor, Don State Technical University (Russian Federation);
Vladimir G. Mokrozub, Dr.Sci. (Eng.), associate professor, Rostov State Transport University (Russian Federation);
Murman A. Mukutadze, Cand.Sci. (Eng.), professor, Tambov State Technical University (Russian Federation);
Nguyen Dong Ahn, Dr.Sci. (Phys. -Math.), professor, Institute of Mechanics, Academy of Sciences and Technologies of Vietnam (Vietnam);
Petr M. Ogar, Dr.Sci. (Eng.), professor, Bratsk State University (Russian Federation);
Gennady A. Ougolnitsky, Dr.Sci. (Phys.-Math.), professor, Southern Federal University (Russian Federation);
Sergey G. Parshin, Dr.Sci. (Eng.), associate professor, St. Petersburg Polytechnic University (Russian Federation);
Valentin L. Popov, Dr.Sci. (Phys. -Math.), professor, Institute of Mechanics, Berlin University of Technology (Germany);
Nikolay N. Prokopenko, Dr.Sci. (Eng.), professor, Don State Technical University (Russian Federation);
Anatoly A. Ryzhkin, Dr.Sci. (Eng.), professor, Don State Technical University (Russian Federation);
Igor B. Sevostianov, Cand.Sci. (Phys. -Math.), professor, New Mexico State University (USA);
Vladimir N. Sidorov, Dr.Sci. (Eng.), Russian University of Transport (Russian Federation);
Arkady N. Solovyev, Dr.Sci. (Phys. -Math.), professor, Don State Technical University (Russian Federation);
Alexandr I. Sukhinov, Dr.Sci. (Phys.-Math.), professor, Don State Technical University (Russian Federation);
Mikhail A. Tamarkin, Dr.Sci. (Eng.), professor, Don State Technical University (Russian Federation);
Valery N. Varavka, Dr.Sci. (Eng.), professor, Don State Technical University (Russian Federation);
Igor M. Verner, Cand.Sci. (Eng.), Docent, Technion (Israel);
Batyr M. Yazyev, Dr.Sci. (Phys. -Math.), professor, Don State Technical University (Russian Federation);
Vilor L. Zakovorotny, Dr.Sci. (Eng.), professor, Don State Technical University (Russian Federation);

CONTENTS

IN MEMORY OF RYZHKIN

4

MECHANICS

- Mailyan L. R., Stel'makh S. A., Shcherban' E. M., Zharebtsov Yu. V., Al-Tulaikhi M. M.* Research of physicommechanical and design characteristics of vibrated, centrifuged and vibro-centrifuged concretes 5
- Salimov M. S., Merkuriev I. V.* Three-dimensional integral dry friction model for the motion of a rectangular body 14
- Artemov A. M., Baranovskii E. S., Verlin A. A., Syomka E. V.* Thick-walled spherical shell problem 22
- Kolesnikova G. P.* Material point physical model rationale while studying kinematic characteristics of a motor vehicle in case of oblique collision with side cable barriers 32

MACHINE BUILDING AND MACHINE SCIENCE

- Antypas I. R., Dyachenko A. G., Saeed B. I.* Inverse analysis method for mathematical modeling of hydrodynamic ballast in a drilling rig 43
- Khinikadze T. A., Rybak A. T., Popikov P. I.* Simulation of the hydraulic system of a device with self-adaptation for power and kinematic parameters on the working body 55
- Poloskov S. S., Erofeev V. A., Sholokhov M. A.* Consumable electrode – additional filler wire arc interaction control under surfacing (DE-GMAW) 62
- Koleda E. V., Kireev S. O., Korchagina M. V., Efimov A. V., Sperling J.* Strength analysis of the TWS 600 plunger pump body in Solid Works Simulation 71
- Berezhnoy S. B., Kurapov G. V.* Power analysis of chain transmission with gear chain and involute sprockets 82
- Peredelsky V. A., Harchenko V. Y., Chernogorov A. L., Tihinov S. V.* On detection of crack-like welding defects by existing quality control methods 89

INFORMATION TECHNOLOGY, COMPUTER SCIENCE, AND MANAGEMENT

- Gurskiy S. S., Mogilevskaya N. S.* On the modification of bit-flipping decoder of LDPC-codes 96
- Gabrielyan D. D., Kostoglotov A. A., Safaryan O. A., Cherckesova L. V., Dvornikov O. V.* Method for estimating time length using simultaneous phase measurements in the system of simultaneously and independently operating generators 105

IN MEMORY OF RYZHKIN



On January 27, 2021, at the 84th year of his life, a remarkable scientist, engineer and organizer, Doctor of Engineering Sciences, Professor Anatoly Andreevich Ryzhkin died a sudden death.

Anatoly A. Ryzhkin was Honored Worker of Science and Technology of the Russian Federation, Doctor of Engineering Sciences, Professor.

Anatoly Andreevich was born on January 21, 1938. He graduated from Rostov Institute of Agricultural Engineering (RISKHM) in 1960. All of his more than 60-year working career has been associated with his native university.

In the transition time for RISKHM and the entire Russian education, he headed the University – in February 1988, he was elected Rector and held this position until 2007. Anatoly A. Ryzhkin made a great contribution to the transformation of a branch institute of agricultural engineering into a technical university: a modern base for scientific and educational process was created, the number of specialties was increased, postgraduate programs were expanded, and doctoral programs were opened, social infrastructure facilities were developed. As a result, RISKHM has become a regional center of education, science, and culture. In 1992, on his initiative and under his personal leadership, by the decision of the Government of the Russian Federation, RISKHM was transformed into Don State Technical University (DSTU).

Anatoly A. Ryzhkin is a well-known scientist in the field of friction and wear under the conditions of cutting materials. He founded and headed the scientific direction “Physicochemical and thermodynamic fundamentals of wear resistance control of tool cutting materials”. A. A. Ryzhkin's applied research works were aimed at creating technologies for strengthening tool materials. The results of R&D are implemented at various enterprises of the Rostov region and are widely used in the training of students majoring in “Design and technological support of machine-building industries”.

A. A. Ryzhkin is the author of more than 450 scientific and method papers. More than 50 of them were published abroad in English, German, Polish, Spanish, and other languages. Over the years, Professor A. A. Ryzhkin had led the postgraduate and doctoral studies, was Chairman of the Dissertation Defence Board at Don State Technical University. Anatoly Andreevich personally prepared 16 candidates and 5 doctors of engineering sciences.

For more than 15 years, Anatoly A. Ryzhkin headed the Council of Rectors of Universities of the Rostov region, which, under his leadership, became an effective public and state body for governing the education sector of the Rostov Region.

In recent years, Anatoly Andreevich was Head of the Metal-Cutting Machines and Tools Department, as well as the Vice-president of the Association for Engineering Education of Russia, a member of the Problem Council for Mechanical Engineering under the Ministry of Education and Science of the Russian Federation.

For long-term and conscientious work, a great contribution to solving problems of higher education, large-scale scientific and public activities, Anatoly A. Ryzhkin was awarded various state awards and honorary titles: Veteran of Labor, Honorary Professor of DSTU, Honored Worker of Science and Technology of the Russian Federation, Honorary Worker of Higher School of the Russian Federation. He is laureate of awards of President of the Russian Federation and the Government of the Russian Federation in the field of education; holder of the Order of Merit for the Fatherland, IV degree, the Order of Friendship, the Badge of Honor, the Medal for Valiant Labor, the Order of Merit to the Rostov Region.

MECHANICS



UDC 691.328

<https://doi.org/10.23947/2687-1653-2021-21-1-5-13>

Research of physicomaterial and design characteristics of vibrated, centrifuged and vibro-centrifuged concretes

L. R. Mailyan¹, S. A. Stel'makh¹, E. M. Shcherban'¹, Yu. V. Zhrebtsov¹, M. M. Al-Tulaikhi²

¹Don State Technical University (Rostov-on-Don, Russian Federation)

²Ministry of Higher Education & Scientific Research (Baghdad, Iraq)



Introduction. Currently, the obtaining of lightweight concrete and reinforced concrete products and structures with the improved structure and characteristics is a challenge. This can be achieved through centrifugation or in a more advanced way — vibro-centrifugation. At the same time, the influence of centrifugal and centripetal forces of inertia in these types of technologies causes differences in the cross-section properties of concrete products and structures. To reflect this in the calculations, it is required to experimentally and analytically investigate the qualitative and quantitative patterns of such differences in the characteristics of concretes obtained through different technologies.

Materials and Methods. The study used the cross-section averaged characteristics of concrete — “integral characteristics of concrete”. The applicable raw materials included portland cement 500, crushed stone fraction 5-20, medium sand. Nine control samples of annular cross-section obtained through vibrating, centrifuging, and vibro-centrifugation were manufactured and tested. The essence of the technique was that each manufactured experimental control sample was used in several types of tests in-parallel. From the total annular section of each sample, three conditional quadrants were distinguished, from which standard samples of small size were cut out. Subsequently, they were tested for axial compression, tension, and flexural tension. The following test equipment was used: electronically controlled mechanical press IPS-10 — for compression testing of prisms, and the breaking machine R-10 — for testing samples for axial tension. Strain sensors and dial indicators were used to measure concrete deformations. Oscilloscopes were also used to obtain the deformative and strength properties of concrete, including full deformation diagrams with descending branches.

Results. We have analyzed the calculation results of the integral design characteristics of the concretes obtained through vibration, centrifugation and vibro-centrifugation. It is established that due to the influence of centrifugal and centripetal forces of inertia under centrifugation and vibration centrifugation, the characteristics of concrete in cross-section become different. In some cases, these differences can be very significant. We have developed and tested the following: a new method for evaluating the dependence of the integral (cross-section averaged) design characteristics of concrete (density, cubic and prismatic axial compressive strength); ultimate deformations under axial compression; axial tensile and flexural tensile strength; ultimate deformations under axial tension; elasticity modulus; diagram of “stress σ_b –strain ϵ_b ” under compression; diagram of “stress σ_{bt} –strain ϵ_{bt} ” under tension on the manufacturing technology (vibrating, centrifuging, vibration centrifugation).

Discussion and Conclusions. Based on the results of the research, conclusions are formulated on the positive effect of the proposed technology of joint vibrating and centrifuging. It consists in improving the integral design characteristics and structure of concrete from vibrating to centrifuging and from centrifuging to vibro-centrifuging.

Keywords: vibrating, centrifugation, vibro-centrifugation, column calculation, variatropic structure, integral characteristics of concrete, ultimate deformations, compressive strength, elasticity modulus.

For citation: L. R. Mailyan, S. A. Stel'makh, E. M. Shcherban', et al. Researches of physicomaterial and design characteristics of vibrated, centrifuged and vibro-centrifuged concretes. Advanced Engineering Research, 2021, vol. 21, no. 1, p. 5–13. <https://doi.org/10.23947/2687-1653-2021-21-1-5-13>

© Mailyan L. R., Stel'makh S. A., Shcherban E. M., Zhrebtsov Yu. V., Al-Tulaikhi M. M., 2021



Introduction. It is known that through vibro-centrifugation^{1,2,3} [1–11], it is possible to obtain concretes with improved structure and characteristics compared to those obtained through centrifugation and vibration.

However, in a few works on concrete and reinforced concrete annular structures, the influence of the type of technology on the average (general) cross-section characteristics of concrete was considered [12–15]. At the same time, it is obvious that due to the influence of centrifugal and centripetal forces of inertia under centrifugation and vibration centrifugation, the cross-sectional characteristics of concrete differ [16].

In this paper, we experimentally and analytically investigate the qualitative and quantitative patterns of such differences in the characteristics of concretes obtained through various technologies. Obviously, to account for these differences, it is required to introduce some averaged cross-sectional characteristics of the elements. For this purpose, we introduce the term “integral characteristics of concrete”.

Materials and Methods. In total, nine control annular samples made through vibration, centrifugation and vibro-centrifugation were produced and tested. Dimensions of these samples were as follows: outer diameter D — 450 mm, inner diameter d — 150 mm; total height H — 1200 mm.

The equipment and test methods used are described in [8–11].

Crushed stone fraction 5–20 was used as a filler, which brings the properties of the resulting concrete closer to the properties of fine-grained concrete.

In the experiments, the type of manufacturing technology varied, which was recorded in the designations of the samples: vibration — V, centrifugation — C, vibro-centrifugation — VC.

The problem of estimating the dependence of the integral (averaged over the cross-section) structural characteristics of concrete (density, axial compressive strength (cube and prism); ultimate deformations under axial compression; axial tension strength and flexural tension; ultimate deformations under axial tension; elasticity modulus; diagram of “stress σ_b – strain ε_b ” under compression; diagram of “stress σ_{bt} –strain ε_{bt} ” under tension) on the manufacturing technology (vibration, centrifugation, vibro-centrifugation) was considered.

Research Results. The test procedure differed in that each manufactured experimental control sample was used in several types of tests in-parallel. Control samples in a single copy were selected and tested on the 7th, 28th and 180th days.

From the total annular section of each sample, 3 conditional quadrants A , B and C were allocated, from which small-size samples were cut out. Subsequently, they were tested for axial compression, tension, and flexural tension (Fig. 1, 2).

Four cube samples with an edge of 15 cm were cut out of the quadrant A for compression and tension tests (levels 1–4), one prism (15×15×60 cm) — for flexural tension tests (level 5). For the axial compression tests, two prisms (15×15×60 cm) were cut out of the quadrant B (levels 1–2). Next, three prisms (15×15×60 cm) were cut out of the quadrant C for axial tension tests (levels 1–2).

After testing the cubes for axial compression, we obtained values $R_{b,cub}$, after testing the prisms for axial compression — values R_b , ε_{bR} , R_{bt} , ε_{btR} , $E_b=E_{bt}$ and the deformation diagram “ σ_b – ε_b ”; after testing the prisms for axial tension — values R_{bt} and the deformation diagram “ σ_{bt} – ε_{bt} ”; and after testing the prisms for flexural tension — values R_{btb} .

¹ Aksomitas GA. Strength of short centrifuged annular section columns with longitudinal reinforcement of class At-V under short-term compression: Cand.Sci. (Eng.) diss. Vilnius: VISI; 1984. 261 p. (In Russ.)

² Petrov VP. Technology and properties of centrifuged concrete with combined aggregate for overhead contact line supports: Cand.Sci. (Eng.) diss. Rostov-on-Don: RISI; 1983. 175 p. (In Russ.)

³ Rajan Suwal. Properties of centrifuged concrete and improvement of the design of centrifuged reinforced concrete poles for power transmission lines: Cand.Sci. (Eng.) diss. Rostov-on-Don: RGAS; 1997. 267 p. (In Russ.)

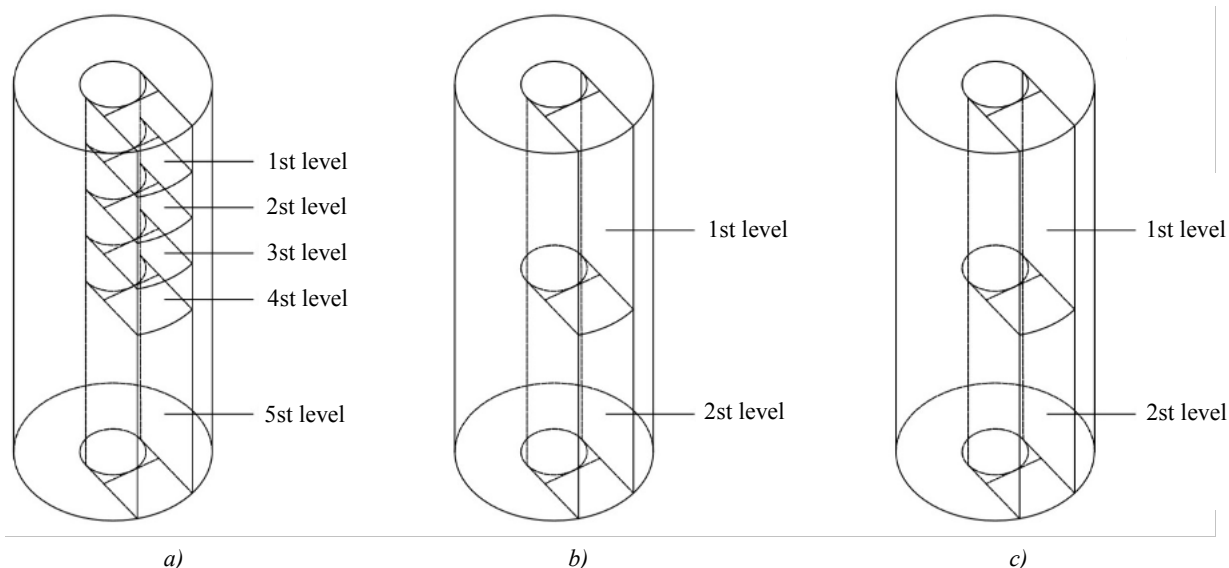


Fig. 1. Scheme of manufacturing small-size concrete samples from quadrants along the height of experimental control full-scale samples of annular cross-section for calculating integral characteristics: a) quadrant A; b) quadrant B; c) quadrant C

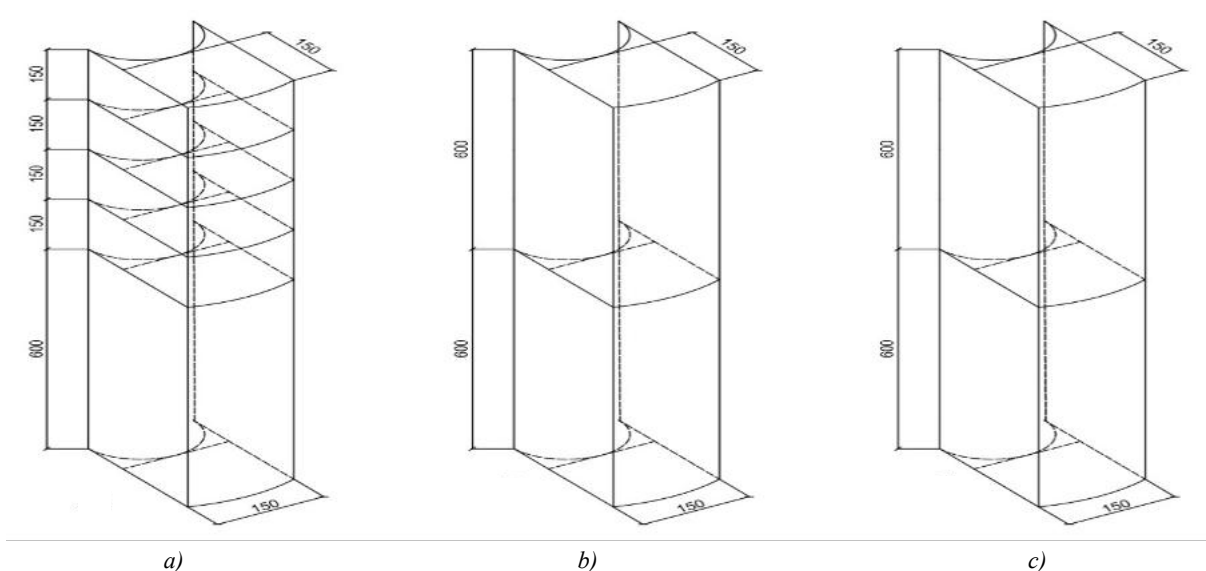


Fig. 2. Experimental small-size concrete samples from quadrants A, B, C of experimental control samples of full-scale annular cross-section for the analysis of integral structural characteristics a) quadrant A; b) quadrant B; c) quadrant C

The test procedure according to GOST 10 180 was applied. The following test equipment was used: IPS-10 — for testing prisms for compression, and P-10 — for testing samples for axial tension.

To measure concrete deformations, strain sensors with a measurement base of 50 mm and dial indicators with graduation 0.001 mm were used.

To obtain the deformative and strength properties of concrete, including complete deformation diagrams with descending branches, experiments were carried out using a constant deformation rate.

For this purpose, in addition to strain gauges, oscilloscopes were also used.

For tests with the same load feed rate, a loading step of $0.1R$ was selected, and the deformations of the prisms increased with a step of $0.1\varepsilon_R$ (Fig. 3).

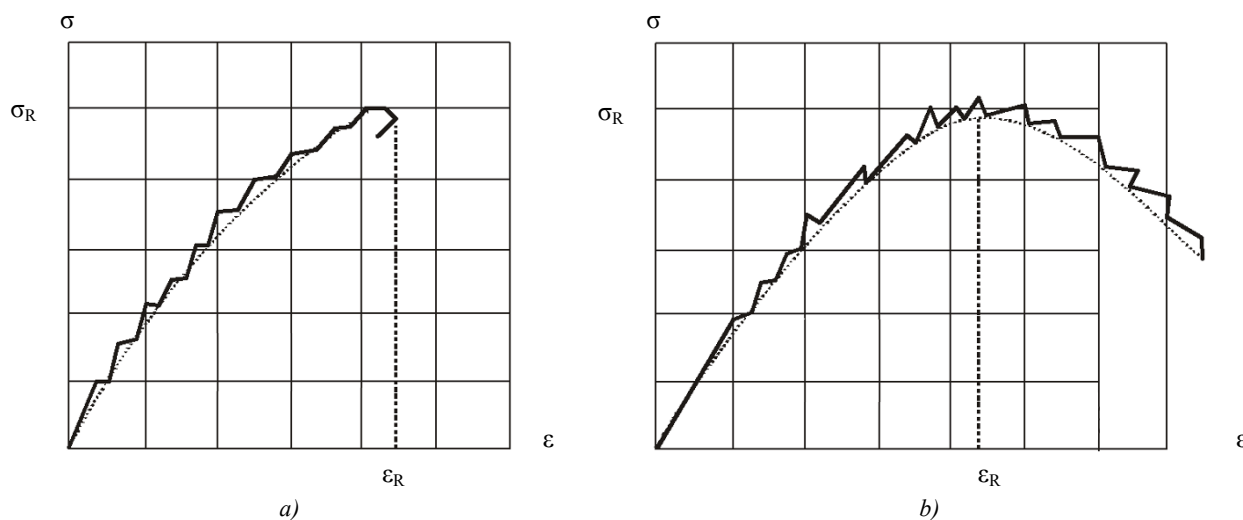


Fig. 3. Test modes of experimental small-size samples:
 a) — step-by-step, with constant loading rate ($\Delta\sigma = \text{const}$);
 b) — step-by-step, with constant deformation rate ($\Delta\epsilon = \text{const}$)

The final test mode consisted in increasing the load to the maximum and its subsequent decrease in the process of increasing deformation. Thus, during the tests, the descending branch of the concrete diagrams “ $\sigma - \epsilon$ ” was fixed, which has a fairly clear outline up to about the value of $\sigma = 0.8 R$, both under compression and tension. Subsequently, the dependence acquired a very unstable character

After analyzing the results obtained, we can draw conclusions about the influence of the sample manufacturing technology. The results of experimental studies of changes in the integral characteristics of experimental concrete samples, depending on the manufacturing technology, are shown in Fig. 4–10.

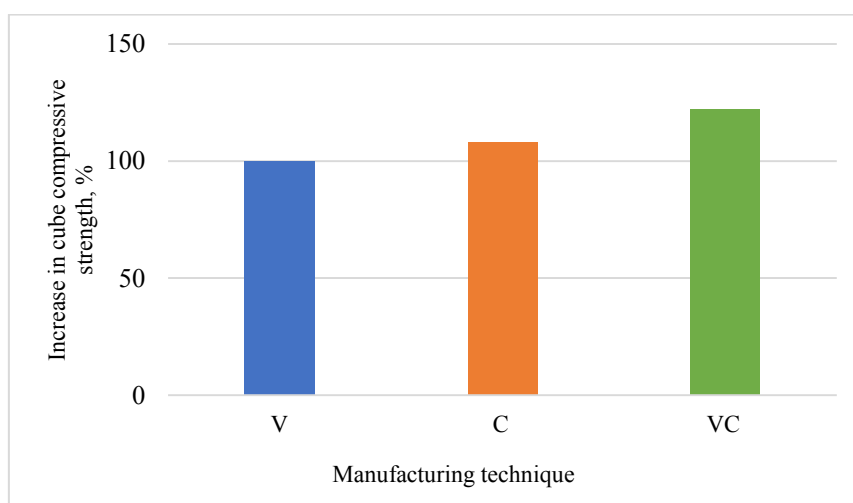


Fig. 4. Influence of manufacturing technique on increase in cube strength of concrete under compression

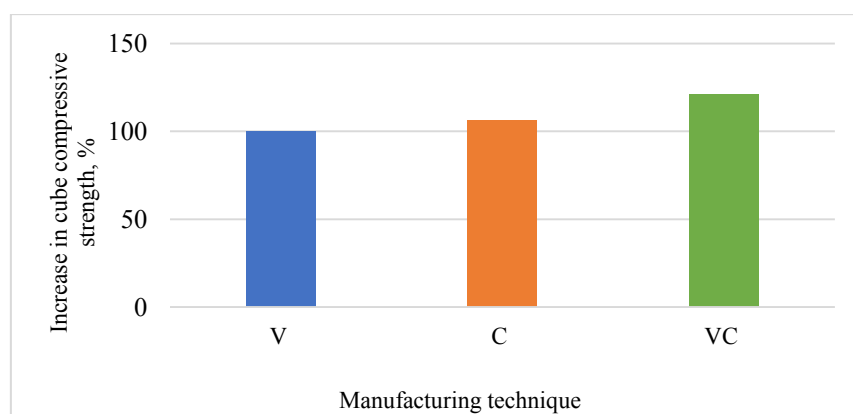


Fig. 5. Influence of manufacturing technology on increase in prism strength of concrete under axial compression

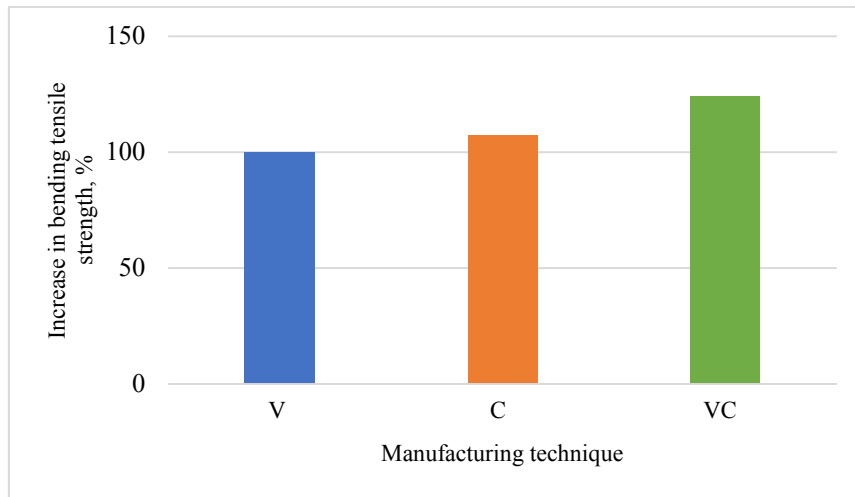


Fig. 6. Dependence of increase in bending tensile strength of concrete on manufacturing technique

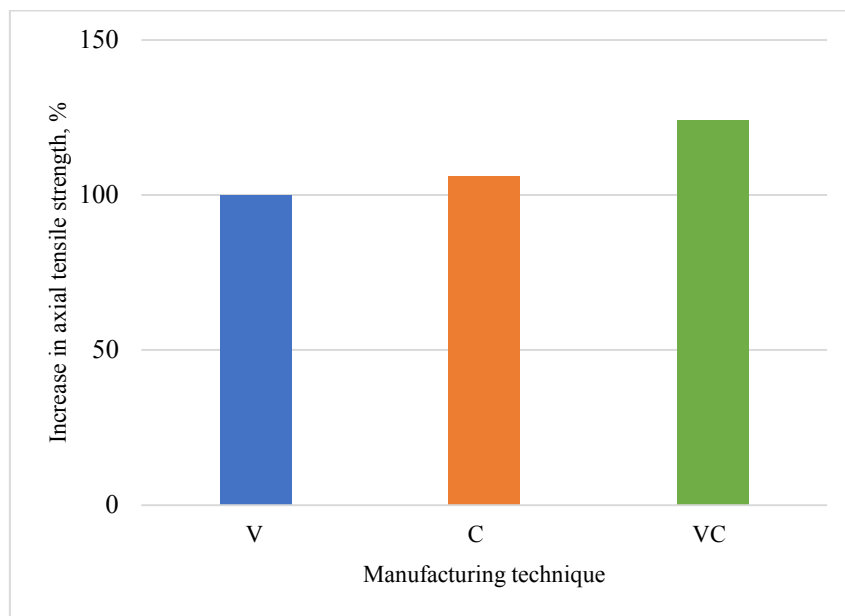


Fig. 7. Dependence of increase in axial tensile strength of concrete on manufacturing technique

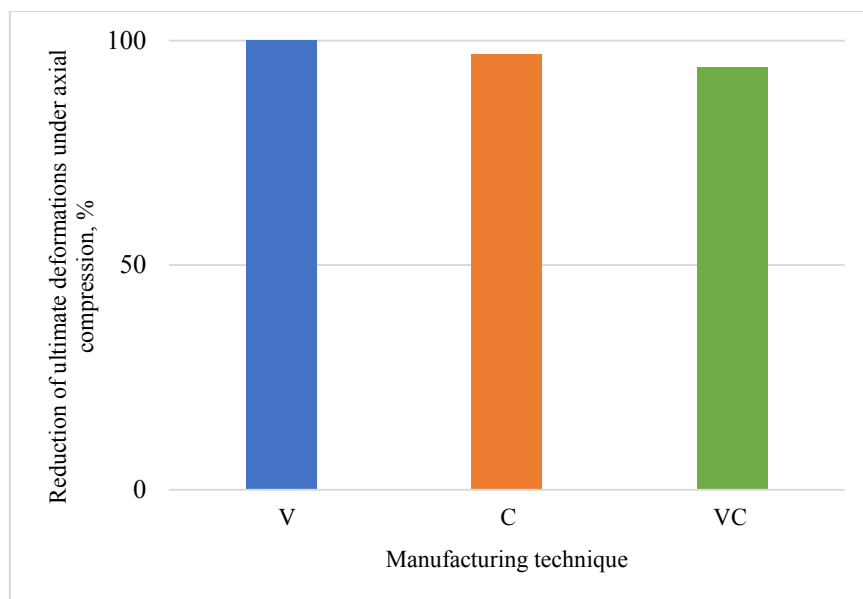


Fig. 8. Dependence of reduction of ultimate deformations under axial compression of concrete on manufacturing technique

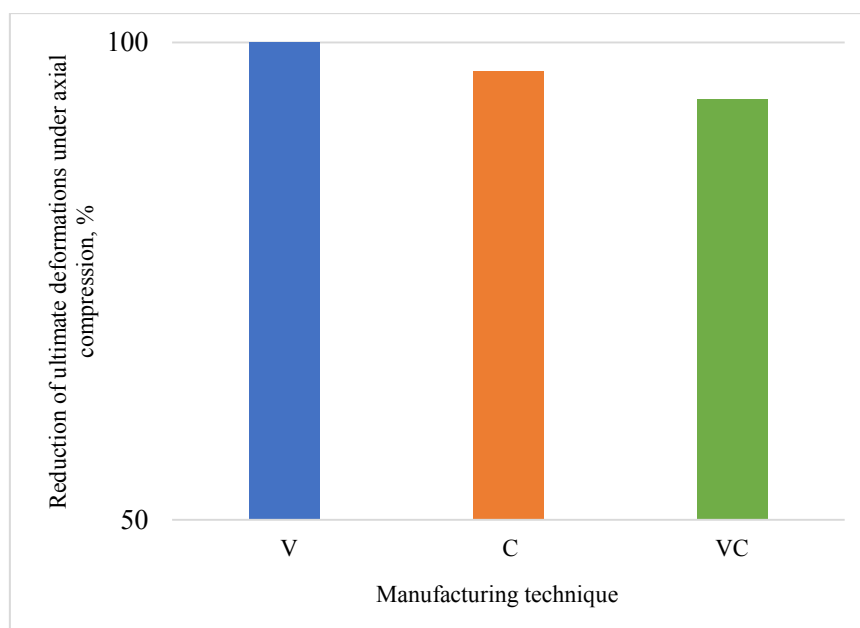


Fig. 9. Dependence of reduction of ultimate deformations under axial tension of concrete on manufacturing technique

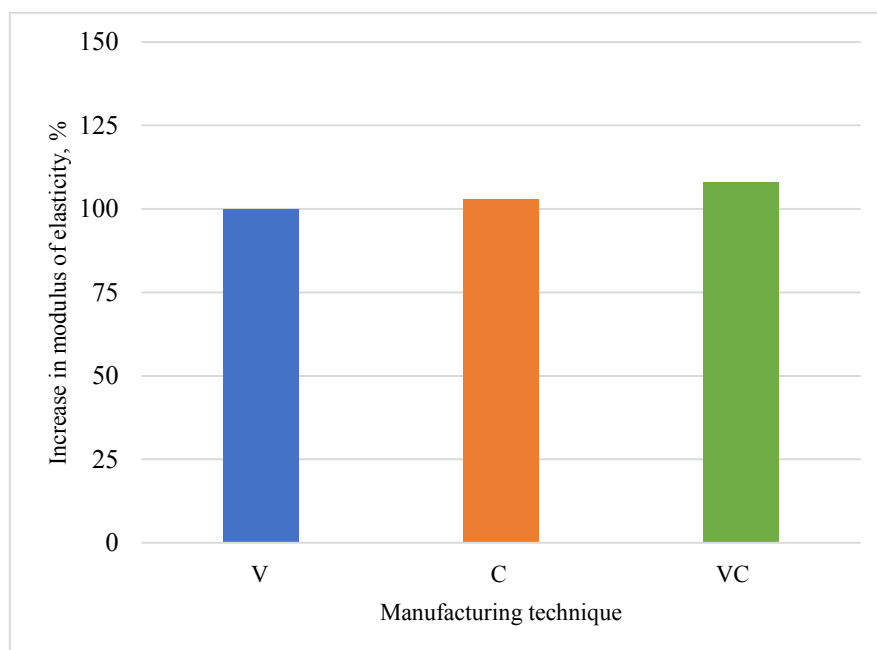


Fig. 10. Influence of manufacturing technique on increase in the concrete modulus of elasticity

Discussion and Conclusions. The influence of the sample manufacturing technology on the density at all ages was minimal (about 2 %), therefore, when calculating, the indicator “density” can be neglected.

Vibro-centrifugated concretes showed higher values in terms of “compressive strength” and “tensile strength” than vibrated and centrifuged concretes, namely: prism and cube compressive strength — up to 22.0 %, axial and flexural tensile strength — up to 27.0%.

Due to the ordering of the ongoing processes of hydration of cement stone, an increase in the compressive and tensile strengths of concrete with simultaneous vibration and centrifugation, in comparison with centrifuged and vibrated samples, with age occurs in the studied range of concrete age (7-180 days) and is practically within the same limits in all ages.

For vibro-centrifuged samples, there is a slight decrease (up to 6 %) in the ultimate deformations under axial compression and tension. This corresponds to the maximum strength of the concretes under study.

Vibro-centrifugated concretes, in comparison with vibrated and centrifuged concretes, showed the lowest ultimate deformations at any age.

The values of “compressive modulus E_b ” and “tensile modulus E_{bt} ” at all ages of concrete were up to 8.0 % higher in vibro-centrifuged concretes than in vibro-centrifuged and centrifuged concretes.

An increase in strength, with a parallel decrease in the ultimate deformations, was the reason for an increase in E_b and E_{bt} in concretes with simultaneous vibration and centrifugation, rather than in concretes with one of the types of compaction. This fact affected the “stress-strain” diagram — the maximum shifted up and to the left.

Differences in the stress-strain diagrams under compression and tension, characteristic of concretes with simultaneous centrifugation and vibration, at all ages are as follows:

- increase in strength and decrease in ultimate deformations (maximum shifts up and to the left);
- increase in the initial modulus of elasticity (increase at the ascending angle origin).

At all ages of concretes, the following tendency was characteristic: an increase in the lifting capacity of the ascending branch of the diagrams, a decrease in the descending branch in centrifuged and vibro-centrifuged concretes compared to vibrated ones.

According to this study, it is appropriate to draw the following conclusions.

1. Studies of the integral design characteristics under compression and tension of the considered types of concrete of various manufacturing techniques at the ages of 7, 28 and 180 days showed:

- concrete performance is improved from vibrating to centrifuging and from centrifuging to vibro-centrifuging;
- increase at all ages of compressive and tensile strengths (up to 23 %);
- reduction of all ultimate deformations (up to 8 %);
- increase in elastic modulus under various types of loading (up to 10 %).

2. For all integral diagrams of the “stress-strain” deformation of concrete with simultaneous vibration and centrifugation, the following is characteristic:

- moving the maximum up and to the left;
- increasing at the ascending angle origin;
- increasing the chart lift in the ascending branch.

3. Through numerous experimental studies, it has been established that simultaneous vibration and centrifugation contributes to the production of concretes with improved structure and characteristics, rather than concretes obtained by only one type of impact — centrifugation or on.

References

1. Akhverdov IN. Osnovy fiziki betona [Concrete physics fundamentals]. Moscow: Stroizdat; 1981. 464 p. (In Russ.)
2. Batashev VM. Issledovanie prochnosti i deformatsii zhelezobetonnykh ehlementov kol'tseвого secheniya pri izgibe, szhatii i rastyazhenii [Investigation of the strength and deformation of reinforced concrete elements of the annular section under bending, compression and tension]. Trudy instituta Ehnergoset'proekt. 1975;6:70–86. (In Russ.)
3. Podol'skii VI. Zhelezobetonnye opory kontaktnoi seti. Konstruktsiya, ehkspluatatsiya, diagnostika [Reinforced concrete supports of the contact network. Design, operation, diagnostics]. Moscow: Intekst; 2007. 152 p. (In Russ.)
4. Romanenko EY, Trubitsin MA. Sposoby povysheniya nadezhnosti tsentrifugirovannykh opor kontaktnoi seti [Methods of dependability improvement of contact network centrifuged supports]. Engineering Journal of Don. 2018;1(48):125. URL: <http://www.ivdon.ru/ru/magazine/archive/n1y2018/4680> (accessed: 12.10.2020). (In Russ.)
5. Mailyan LR, Stelmakh SA, Khalyushev AK, et al. Optimizatsiya parametrov tsentrifugirovannykh izdelii kol'tseвого secheniya na stadii uplotneniya [Optimization of parameters of centrifuged products of the annular section at the compaction stage]. Engineering Journal of Don. 2018;3(50):121. URL: <http://ivdon.ru/ru/magazine/archive/n3y2018/5123> (accessed: 12.10.2020). (In Russ.)
6. Mailyan LR, Stel'makh SA, Khalyushev AK, et al. Optimizatsiya tekhnologicheskikh parametrov dlya izgotovleniya tsentrifugirovannykh betonnykh obraztsov kol'tseвого secheniya [Optimization of technological

parameters for manufacturing centrifuged concrete samples of annular section]. Construction and Architecture. 2018;6(1):1–6. DOI: 10.29039/article_5abc8c1fa5cff2.77063965_(In Russ.)

7. Mailyan LR, Stel'makh SA, Shcherban' EM, et al. Determination and use of hidden strength reserves of centrifuged reinforced constructions by means of calculation and experimental methods. Russian Journal of Building Construction and Architecture. 2020;1(45):6–14. DOI: 10.25987/VSTU.2020.45.1.001

8. Stel'makh SA, Shcherban' EM, Shuyskiy AI, et al. Theoretical and Practical Aspects of the Formation of the Variational Structure of Centrifuged Products from Heavy Concrete. Materials Science Forum. 2018;931:502–507. DOI: 10.4028/www.scientific.net/msf.931.502

9. Tasevski D, Ruiz MF, Muttoni A. Compressive strength and deformation capacity of concrete under sustained loading and low stress rates. Journal of Advanced Concrete Technology. 2018;16:396–415. DOI: 10.3151/jact.16.396

10. Kim J-J, Yoo D-Y. Effects of fiber shape and distance on the pullout behavior of steel fibers embedded in ultra-high-performance concrete. Cement and Concrete Composites. 2019;103:213–223. DOI: 10.1016/j.cemconcomp.2019.05.006

11. Alani AH, Bunnori NM, Noaman AT. Durability performance of a novel ultra-high-performance PET green concrete (UHPPGC). Construction and Building Materials. 2019;209:395–405. DOI: 10.1016/j.conbuildmat.2019.03.088

12. Ferrotto MF, Fischer O, Cavalrti L. Analysis-oriented stress–strain model of CRFP-confined circular concrete columns with applied preload. Materials and Structures. 2018;51:44. Available from: <https://link.springer.com/article/10.1617%2Fs11527-018-1169-0> (accessed: 12.10.2020).

13. Kirthika SK, Singh SK. Durability studies on recycled fine aggregate concrete. Construction and Building Materials. 2020;250:118850. Available from: <https://doi.org/10.1016/j.conbuildmat.2020.118850> (accessed: 12.10.2020).

14. Maruyama I, Lura P. Properties of early-age concrete relevant to cracking in massive concrete. Cement and Concrete Research. 2019;123:105770. Available from: <https://www.sciencedirect.com/science/article/abs/pii/S0008884619303643?via%3Dihub> (accessed: 12.10.2020).

15. Yanovskaya AV, Shcherban EM, Stelmakh SA. Povyshenie ehkspluatatsionnykh kharakteristik betona svainykh fundamentov za schet retsepturno-tekhnologicheskikh priemov [Improving the operational characteristics of concrete pile foundations due to composition and technological methods]. Young Researcher of the Don. 2020;3(24):110–115. (In Russ.)

16. Karnoub A, Nezhizhimov DB, Shirinyan KS. Issledovanie i modelirovanie mnogosloinogo kompozitnogo materiala s primeneniem bazal'tovoi tkani [Research and modeling of a multilayer composite material using basalt fabric]. Vestnik of DSTU. 2020;20(1):5–14. (In Russ.)

Submitted 30.11.2020

Scheduled in the issue 08.02.2021

About the Authors:

Mailyan, Levon R., professor of the Motorways Department, Don State Technical University (1, Gagarin sq., Rostov-on-Don, 344003, RF), Dr.Sci. (Eng.), professor, ScopusID: 57192662909, ResearcherID: [AAO-9095-2020](https://orcid.org/0000-0003-0162-2699), ORCID: <https://orcid.org/0000-0003-0162-2699>, lrn@aanet.ru

Stel'makh, Sergei A., associate professor of the Engineering Geology, Primary Structures and Footings Department, Don State Technical University (1, Gagarin sq., Rostov-on-Don, 344003, RF), Cand.Sci. (Eng.), associate professor, ScopusID: 57197736878, ResearcherID: [AAG-6076-2020](https://orcid.org/0000-0002-0364-5504), ORCID: <https://orcid.org/0000-0002-0364-5504>, sergej.stelmax@mail.ru

Zherebtsov, Yuriy V., graduate student of the Technological Engineering and Expertise in Building Industry Department, Don State Technical University (1, Gagarin sq., Rostov-on-Don, 344003, RF), ORCID: <https://orcid.org/0000-0002-6162-0049>, yuri.zherebtsov@gmail.com

Shcherban', Evgenii M., associate professor of the Engineering Geology, Primary Structures and Footings Department, Don State Technical University (1, Gagarin sq., Rostov-on-Don, 344003, RF), Cand.Sci. (Eng.), associate professor, ScopusID: 57197730793, ResearcherID: [AAG-6070-2020](https://orcid.org/0000-0001-5376-247X), ORCID: <https://orcid.org/0000-0001-5376-247X>, au-geen@mail.ru

Al-Tulaikhi Mustafa Mokhammed otman, Master of Engineering and Technology in Construction, Ministry of Higher Education & Scientific Research (Mohatextradeltd, Ministry of Higher Education & Scientific Research, Baghdad, Iraq. 00964, Al-Mustansyriah, Iraq), ORCID: <https://orcid.org/0000-0001-7261-4560>, engmustafa95@yandex.ru

Claimed contributorship

L. R. Mailyan: basic concept formulation; approval of the final version of the paper before submitting it for publication. E. M. Shcherban': collection, analysis and interpretation of the material for the paper. S. A. Stel'makh: computational analysis; text preparation; formulation of conclusions. Yu. V. Zherebtsov: plotting graphs and tables for the paper. M. M. Al-Tulaikhi: translation of the abstract and keywords into English, review of foreign literature sources.

All authors have read and approved the final manuscript.

MECHANICS



UDC 531.36

<https://doi.org/10.23947/2687-1653-2021-21-1-14-21>

Three-dimensional integral dry friction model for the motion of a rectangular body



M. S. Salimov, I. V. Merkuriev

National Research University "MPEI" (Moscow, Russian Federation)

Introduction. A three-dimensional dry friction model in the interaction of a rectangular body and a horizontal rough surface is considered. It is assumed that there is no separation of the body from the horizontal surface. The body motion occurs under the conditions of combined dynamics when, in addition to the longitudinal movement, the body participates in twisting.

Materials and Methods. Linear fractional Pade approximations are proposed, which replaced the cumbersome analytical expressions that most accurately describe the motion of bodies on rough surfaces. New mathematical models describing sliding and twisting of bodies with a rectangular base are proposed.

Results. Analytical expressions of the principal vector and moment of friction for rectangular contact areas are developed and scientifically established. A friction model that takes into account the relationship between sliding and twisting speeds, which provides finding solutions for Pade dependences, is developed. After numerical solution to the equations of motion, the dependences of the sliding speed and angular velocity on time were obtained and constructed. Graphs of the dependences of the friction forces and their moment on two parameters (angular velocity and slip velocity) were constructed, which enabled to compare the integral and normalized models of friction. The comparison results showed good agreement of the integral model and the model based on Pade approximations.

Discussion and Conclusions. The results obtained provide considering the dynamic coupling of components, which determines the force interaction of a rectangular body and a horizontal surface. These results can be used in mobile robotics. The analyzed motion of the body occurs through the motion control of a material point inside the body. Such mobile robots can be used when solving a wide class of problems: when creating autonomous robots for the exploration of outer space and planets; in the diagnosis and treatment in case of passing through complex structures of veins and arteries; in research under water, in places of large differential temperature; in underground operations.

Keywords: dry friction, rectangular body, solid body, dynamics, sliding, twisting, friction force, Pade approximations.

For citation: M. S. Salimov, I. V. Merkuriev. Three-dimensional integral dry friction model for the motion of a rectangular body. Advanced Engineering Research, 2021, vol. 21, no. 1. — p. 14–21. <https://doi.org/10.23947/2687-1653-2021-21-1-14-21>

© Salimov M. S., Merkuriev I. V., 2021



Introduction. The study of the movement of a rectangular body is a challenge in the mobile robotics [1]. This movement is due to the control of the material point inside the body. Such mobile robots can be used to solve a wide range of tasks. For example, when creating autonomous robots for the exploration of outer space and planets; for medical purposes, in diagnosis and treatment, for example, in case of passing through complex structures of veins and arteries; as well as for underground work and research under difficult conditions, for example, under water and in places of large differential temperature [1, 2].

Thus, more and more challenges are being set for robotics, which require theoretical research, including studying models of friction between the body and the surface under the conditions of combined dynamics [3, 4]. Since the movement of the mobile robot occurs in different directions, it is required to consider the longitudinal movement and rotation. Thus, in the structure of the friction model, it is required to provide the relationship between the sliding and twisting speeds [5]. An important development in the description of this relationship was made in [6]. Its author

managed to solve the equations for the principal moment and the vector of friction forces where a rectangle was considered as a contact area. Such analytical expressions enable to most accurately describe the motion of bodies on rough surfaces, but they are cumbersome and complex since they contain integral expressions. Hence, the authors of [7] constructed linear fractional Pade approximations, which made it possible to find solutions for the resulting dependences.

Pade approximation can be used to explain the effects of combined dry friction for linear and angular velocities. On the basis of Pade approximations, it became possible to create new models of friction [8, 9], which later began to be classified for better interpretation [10]. The classification occurs depending on the number of parameters. Thus, in [11], the authors introduced the notions of dimension and order of the dry friction model depending on the order of the used Pade approximations.

The model of sliding and twisting friction, which is proposed in the paper [12], provides considering the dynamic connection of the components that determine the force interaction of a rectangular body and a horizontal surface [13].

Problem Statement. We consider a solid body of mass m_0 , which is a rectangular body with uniform faces of length a , width b and height $2h$. A fixed coordinate system $Oxyz$, associated with the body (Fig. 1) is introduced. Point O is located on the horizontal plane. The system. $O_1x_1y_1z_1$ starts at a point O_1 , that corresponds to the geometric center of the body. The axis O_1z_1 is parallel to the axis Oz . The axis O_1x_1 is parallel to the long edge of the body. We introduce the unit vectors e_x, e_y of the axes O_1y_1 and O_1x_1 , respectively.

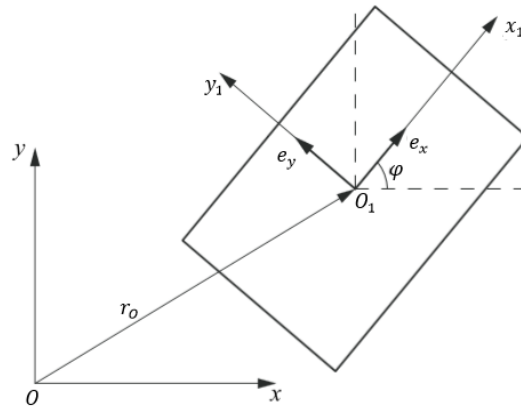


Fig. 1. Coordinate systems

Consider the continuous motion of the body on the surface (Fig. 2), which consists of translational movement and rotation about the axis O_1z_1 . Three coordinates determine the position of the body. The coordinates x_0 , y_0 and h set the origin of the coordinate system $O_1x_1y_1z_1$ in the coordinates $Oxyz$. The rotation of the body relative to its initial position on the axis O_1x_1 is specified by the angle φ . This paper considers the case when the center of mass of the body G and the center of mass of the system O_1 coincide (Fig. 2) [14].

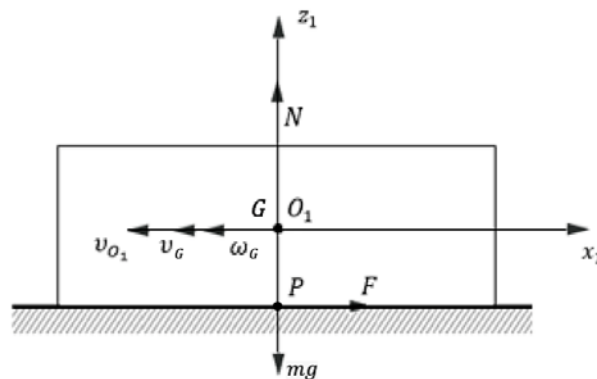


Fig. 2. Movement of the system body

Materials and Methods. The contact area is a rectangle with sides a and b , in which the normal voltage depends on the distance from the point P to the faces of the rectangle (Fig. 3).

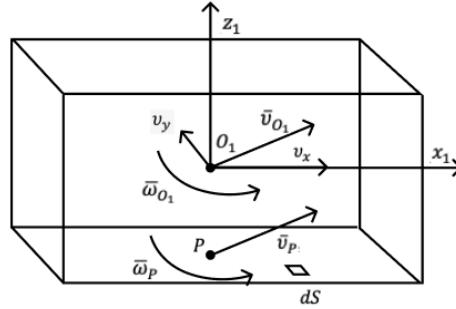


Fig. 3. Velocities of the points O_1 and P

Consider an infinitesimal area dS at an arbitrary point M on the contact surface. We introduce the angle φ between the relative sliding velocity and the axis O_1x_1 . Let us draw the radius vector \vec{r}_{MP} from the point P to the point M . The velocity vector of the point M is denoted v_M , and to find it, we use the Euler formula describing the velocity distribution in a perfectly rigid body:

$$v_M = v_P + \omega \cdot \vec{r}_{MP}.$$

The sliding speed at the point M is decomposed into two components along the axes O_1x_1 and O_1y_1 :

$$v_{Mx} = v_x - y\omega;$$

$$v_{My} = v_y + x\omega.$$

Using Coulomb's law, we find a small increment of the friction force directed against the relative velocity at the point M [15]:

$$d\vec{F} = -f\sigma(x, y) \frac{v_M}{|v_M|} dS,$$

where f — coefficient of friction; $\sigma(x, y)$ — contact stress distribution function depending on the x and y coordinates; $dS = dxdy$ — small area increment [15].

We rewrite the differential of the friction force and the moment of this force in projections on the axes under consideration:

$$dF_x = -f\sigma(x, y) \frac{v_{Mx}}{|v_M|} dxdy;$$

$$dF_y = -f\sigma(x, y) \frac{v_{My}}{|v_M|} dxdy;$$

$$dM_z = \begin{bmatrix} i & j & k \\ x & y & 0 \\ dF_x & dF_y & 0 \end{bmatrix} = xdF_y - ydF_x.$$

As a special case, we consider a uniform distribution of stress in the absence of internal masses in the body, then these stresses will be equal to: $\sigma = \frac{m_0g}{ab}$, but then we will continue the record in general form: $\sigma(x, y)$.

Having integrated the expressions for the friction forces, we obtain:

$$F_x = -f \int_{-a/2}^{a/2} \int_{-b/2}^{b/2} \sigma(x, y) \frac{v_x - y\omega}{|v_M|} dxdy; \quad (1)$$

$$F_y = -f \int_{-a/2}^{a/2} \int_{-b/2}^{b/2} \sigma(x, y) \frac{v_y + x\omega}{|v_M|} dxdy. \quad (2)$$

Relative slip module $|v_M|$ is calculated from the formula:

$$|v_M| = \sqrt{v_{Mx}^2 + v_{My}^2} = \sqrt{v_x^2 + v_y^2 + \omega^2(x^2 + y^2) + 2\omega(v_yx - v_xy)}. \quad (3)$$

Imagine the relative positions of the vectors of variable sliding speed v and the components of the friction force: F_{\parallel} — the component opposite to the sliding speed v ; F_{\perp} — the component perpendicular to the instantaneous slip velocity. At the same time, imagine the coordination of this system with respect to the axes O_1x_1 and O_1y_1 (Fig. 4).

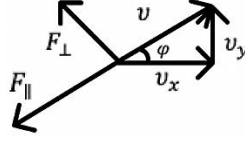


Fig. 4. Components of the friction force and velocity

We will make a transition from the projections of the sliding speed:

$$\begin{cases} v_x = v \cos \varphi, \\ v_y = v \sin \varphi, \end{cases} \quad (4)$$

to the speed module and the sliding angle:

$$\begin{cases} F_{\parallel} = F_x \cos \varphi + F_y \sin \varphi, \\ F_{\perp} = F_x (-\sin \varphi) + F_y \sin \varphi. \end{cases} \quad (5)$$

We will integrate the moment of the friction force on the contact area:

$$M_z = -f \int_{-a/2}^{a/2} \int_{-b/2}^{b/2} \sigma(x, y) \frac{v(x \sin \varphi - y \cos \varphi) + \omega(x^2 + y^2)}{\sqrt{v^2 + \omega^2(x^2 + y^2) + 2\omega v(x \sin \varphi - y \cos \varphi)}} dx dy.$$

Let us substitute the expressions (1)–(3) into the system (5), and also rewrite the expression for the moment of force. As a result, we obtain a three-dimensional model of friction sliding and twisting:

$$F_{\parallel} = -f \int_{-a/2}^{a/2} \int_{-b/2}^{b/2} \sigma(x, y) \cdot \frac{v(\cos^2 \varphi + \sin^2 \varphi) - \omega(y \cos \varphi + x \sin \varphi)}{\sqrt{v^2 + \omega^2(x^2 + y^2) + 2\omega v(x \sin \varphi - y \cos \varphi)}} dx dy; \quad (6)$$

$$F_{\perp} = -f \int_{-a/2}^{a/2} \int_{-b/2}^{b/2} \sigma(x, y) \cdot \frac{\omega(y \sin \varphi + x \cos \varphi)}{\sqrt{v^2 + \omega^2(x^2 + y^2) + 2\omega v(x \sin \varphi - y \cos \varphi)}} dx dy; \quad (7)$$

$$M_z = -f \int_{-a/2}^{a/2} \int_{-b/2}^{b/2} \sigma(x, y) \cdot \frac{v(x \sin \varphi - y \cos \varphi) + \omega(x^2 + y^2)}{\sqrt{v^2 + \omega^2(x^2 + y^2) + 2\omega v(x \sin \varphi - y \cos \varphi)}} dx dy. \quad (8)$$

In order not to solve cumbersome integrals, we use the replacement of the corresponding Pade expansions [16, 17]. Thus, based on the Pade theory [18], these expressions can be formulated as the ratio of two functions of several variables in the entire domain of definition, provided that the functions must have the same order [7]. To define these functions, it is required to determine the behavior of integral expressions (6)–(8) under the following conditions:

$$\frac{\partial F_{\parallel}}{\partial v} \Big|_{v=0} = -\frac{f}{\omega} \int_{-a/2}^{a/2} \int_{-b/2}^{b/2} \sigma(x, y) \cdot \frac{\sqrt{x^2 + y^2}(x^2 + y^2) + (y \cos \varphi + x \sin \varphi)(x \sin \varphi - y \cos \varphi)}{(x^2 + y^2)^2} dx dy = -\frac{f}{\omega} I_0;$$

$$\frac{\partial M_z}{\partial v} \Big|_{v=0} = -\frac{f}{\omega} \int_{-a/2}^{a/2} \int_{-b/2}^{b/2} \sigma(x, y) \cdot \frac{(2y^2 x \sin \varphi - 2y^3 \cos \varphi)}{(x^2 + y^2)^2} dx dy = -\frac{f}{\omega} I_3;$$

$$M_z \Big|_{\omega \rightarrow \infty} = -f \int_{-a/2}^{a/2} \int_{-b/2}^{b/2} \sigma(x, y) \cdot \frac{x^2 - y^2}{\sqrt{x^2 + y^2}} dx dy = -f I_6;$$

$$F_{\perp} \Big|_{\omega \rightarrow \infty} = -f \int_{-a/2}^{a/2} \int_{-b/2}^{b/2} \sigma(x, y) \cdot \frac{y \sin \varphi + x \cos \varphi}{\sqrt{x^2 + y^2}} dx dy = f I_9;$$

$$\frac{\partial F_{\parallel}}{\partial v} \Big|_{\omega=0} = \frac{\partial F_{\parallel}}{\partial \omega} \Big|_{v=0} = \frac{\partial F_{\parallel}}{\partial \omega} \Big|_{\omega=0} = F_{\parallel} \Big|_{\omega \rightarrow \infty} = \frac{\partial F_{\perp}}{\partial v} \Big|_{\omega=0} = \frac{\partial F_{\perp}}{\partial \omega} \Big|_{v=0} =$$

$$= F_{\perp} \Big|_{\omega \rightarrow \infty} = \frac{\partial F_{\perp}}{\partial \omega} \Big|_{\omega=0} = \frac{\partial M_z}{\partial v} \Big|_{\omega=0} = \frac{\partial M_z}{\partial \omega} \Big|_{v=0} = M_z \Big|_{v \rightarrow \infty} = 0.$$

Values of the expressions $\frac{\partial F_{\perp}}{\partial v}|_{v=0}$ and $\frac{\partial M_z}{\partial \omega}|_{\omega=0}$ are not involved in finding the subsequent Pade approximants, therefore, their writing is omitted due to their cumbersomeness. The identical equality to zero is realized under the condition that the voltage σ is symmetric about the center of the rectangular contact spot, i.e., the point P .

An accurate three-dimensional integral model [13] (6)–(8) provides a logical description of dry friction phenomena, but for solving problems of dynamics, such a model is difficult to accept due to the need to calculate impressive integrals [10]. To avoid this procedure, we use [6] to replace the exact integral system with the corresponding expressions using Pade approximations in the whole range of variables. Linear fractional Pade expansions give a three-dimensional model of first-order sliding and twisting friction [19]:

$$F_{\parallel} = F_0 \frac{v+b_1\omega}{v+d_1\omega}; \quad (9)$$

$$M_z = M_0 \frac{\omega+b_2v}{\omega+d_2v}; \quad (10)$$

$$F_{\perp} = F_0 \frac{\omega+b_3v}{\omega+d_3v}. \quad (11)$$

To determine the Pade coefficients, it is required to study the properties of this model at the boundary points by analogy with integral expressions. To do this, we differentiate the parameters F_{\parallel} , F_{\perp} , M_z and thus satisfy the corresponding integral expressions:

$$\begin{cases} F_{\parallel} = -fI_1 \frac{v}{v + \frac{I_0}{I_1}\omega} \\ M_z = -fI_6 \frac{\omega}{\omega + \frac{I_3}{I_9}v} \\ F_{\perp} = -fI_9 \frac{\omega}{\omega + \frac{I_3}{I_9}v} \end{cases}.$$

The system of equations of motion has the form:

$$\begin{aligned} J \frac{d\omega_{O_1}}{dt} &= M_z; \\ (m_0 + m_1) \frac{dv_x}{dt} &= F_x + (m_0 + m_1)v_y\omega_{O_1}; \\ (m_0 + m_1) \frac{dv_y}{dt} &= F_y - (m_0 + m_1)v_x\omega_{O_1}. \end{aligned} \quad (12)$$

We express the time derivatives of the sliding speed and the angular speed using the formulas (3)–(5):

$$\begin{aligned} \frac{dv}{dt} &= \frac{1}{2\sqrt{v_x^2 + v_y^2}} \left(2v_x \frac{dv_x}{dt} + 2v_y \frac{dv_y}{dt} \right); \\ \frac{d\varphi}{dt} &= \frac{1}{m_0 + m_1} \left(-\frac{v \sin \varphi}{v^2} F_x + \frac{v \cos \varphi}{v^2} F_y \right). \end{aligned}$$

We rewrite these equations using the formulas (3)–(5) for $\omega_{O_1} = \omega/a$ and add the first equation from the system (12):

$$\begin{aligned} J \frac{d\omega}{dt} &= M_z a; \\ (m_0 + m_1) \frac{dv}{dt} &= F_{\parallel}; \\ (m_0 + m_1) v \dot{\varphi} &= F_{\perp}. \end{aligned} \quad (13)$$

Research Results. Next, we calculate the integral expressions of the parameters I_0 , I_1 , I_3 , I_6 , I_9 c using the Wolfram Mathematica software package for the following values:

$$f = 1; a = 0.5 \text{ m}; b = 0.2 \text{ m}; m_0 = 1 \text{ kg}, \sigma = \frac{m_0 g}{ab} = 87 \text{ kg/s}^2\text{m}$$

and substitute in the system of equations (13). Based on numerical expressions, we build graphs of integral and normalized functions depending on the parameter $= v/\omega$. Fig. 5 shows graphs of the functions of the integral friction (11)–(13), as well as models based on Pade approximations (14)–(16).

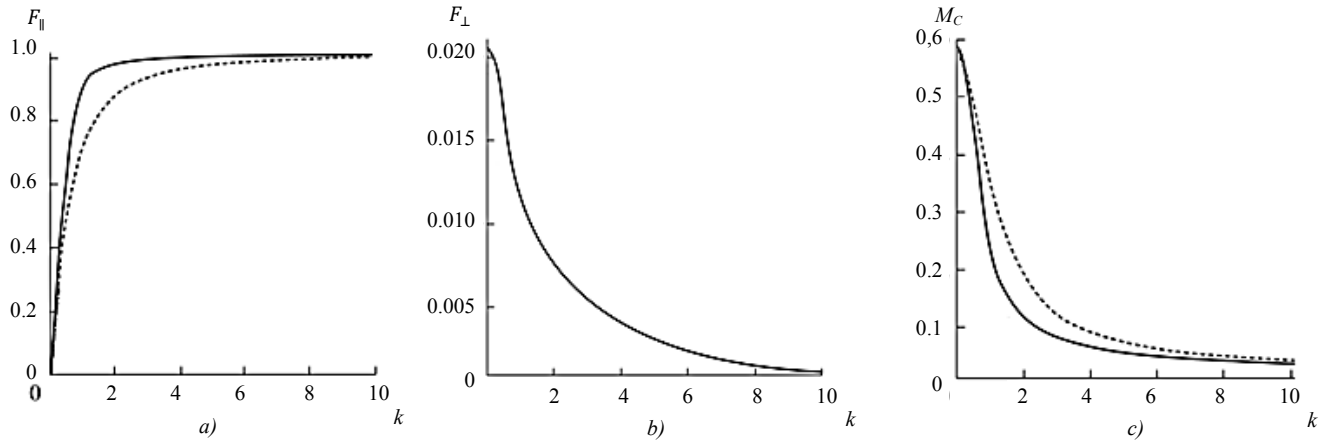


Fig. 5. Graphs of integral (solid lines) and normalized (dotted lines) functions of the tangent (a), normal (b) components of friction force and friction moment (c)

Based on the graphs of the functions (Fig. 5), we can talk about good matching of the considered models. Next, we obtain graphs of the dependences of the characteristic parameters on time (Fig. 6).

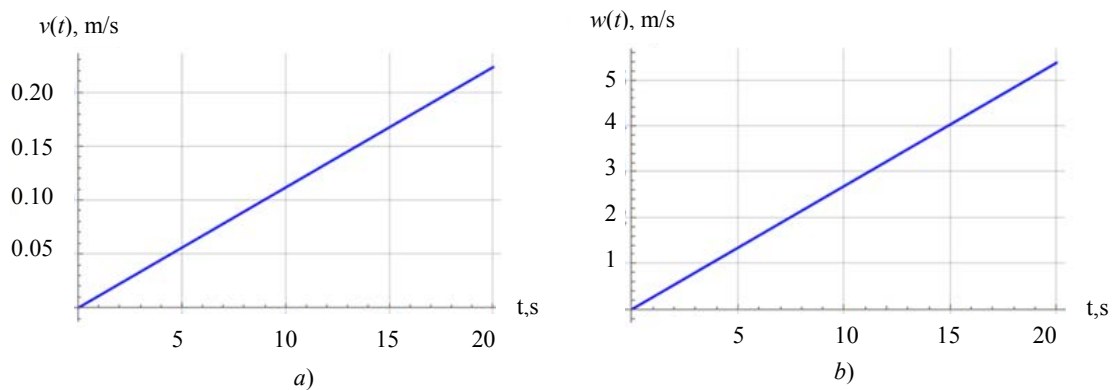


Fig. 6. Dependences of sliding velocity v (a) and angular velocity w (b) on time t

Discussion and Conclusions. The movement of the mobile robot, starting from the contact of its body and the reference plane, under the conditions of combined dynamics, when there is sliding and twisting, is described. Analytical integral expressions are obtained for the tangent and normal components of the friction force [19] and the moment of friction applied to a rectangular contact area. The corresponding Pade approximations are determined for the obtained expressions. The integral and normalized models are compared through plotting the dependences of the friction forces and the moment of friction on the angular velocity and the slip velocity. The comparison results showed good matching of the integral model and the model based on the Pade decompositions. The graphs correspond to the logical behavior when a rectangular body moves, since the sliding speed and angular velocity increase according to the specified parameters. Consequently, the combined friction model implemented using Pade approximations can be applied to solve problems related to mobile robots with a rectangular base.

References

1. Salimov MS, Ramzin NS. Dvizhenie tela na vibriruyushchei poverkhnosti v sluchae sukhogo treniya [Element movement on vibrating surface in case of dry friction]. Engineering and Automation Problems. 2019;4:100–104. (In Russ.)

2. Munitsyn LV. Vibrations of a Rigid Body with Cylindrical Surface on a Vibrating Foundation. *Mech. Solids*. 2017;52(6):675–685.
3. Voldrich J. Modelling of the three-dimensional friction contact of vibrating elastic bodies with rough surfaces. *Appl. Comput. Mech.* 2009;3(1):241–252.
4. Chowdhury MA, et al. Sliding friction of steel combinations. *Open Mech. Eng. J.* 2014;8(1):364–369.
5. Martinovs A, Gonca V. Descriptive model of sliding friction processes. *Vide. Tehnologija. Resursi.* = *Environment. Technology. Resources*. 2009;2:227–233.
6. Zhuravlev VF. O modeli sukhogo treniya v zadache kacheniya tverdykh tel [The model of dry friction in the problem of the rolling of rigid bodies]. *Journal of Applied Mathematics and Mechanics*. 1998;62(5):762–767. (In Russ.)
7. Andronov VV, Zhuravlev VF. Sukhoe trenie v zadachakh mekhaniki [Dry friction in mechanical problems] Moscow. Izhevsk: R&C Dynamics; 2010. 184 p. (In Russ.)
8. Acary V, Brémond M, Huber O. On solving contact problems with coulomb friction: Formulations and numerical comparisons. In: *Transactions of the European Network for Nonsmooth Dynamics on Advanced Topics in Nonsmooth Dynamics*. Springer International Publishing; 2018. P. 375–457.
9. Haslinger J, Kučera R, Sassi T. A domain decomposition algorithm for contact problems with Coulomb's friction. *Lect. Notes Comput. Sci. Eng.* 2014;98:889–897.
10. Kireenkov AA. Svyazannaya model' treniya skol'zheniya i vercheniya [Related model of sliding and twisting friction]. *Doklady Akademii Nauk*. 2011;441(6):750–755. (In Russ.)
11. Zhuravlev VF, Kireenkov AA. O razlozheniyakh Pade v zadache o dvumernom kulonovom trenii [Pade expansions in the two-dimensional model of Coulomb friction]. *Mechanics of Solids*. 2005;2:3–13. (In Russ.)
12. Santos AP, et al. Granular packings with sliding, rolling, and twisting friction. *Phys. Rev. E*. 2020;102(3):032903.
13. Kireenkov AA. Trekhmernye modeli treniya [Three-dimensional friction models]. *Vestnik of Lobachevsky University of Nizhni Novgorod*. 2011;4(2):174–176. (In Russ.)
14. Sakharov AV. Povорот tela bez vneshnikh dvizhitelei pri pomoshchi rotora A. V. [Rotation of a body without external propellers using rotor]. *Trudy MFTI*. 2014;6(2):80–91. (In Russ.)
15. Zhuravlev VF. Zakonomernosti treniya pri kombinatsii skol'zheniya i vercheniya [Friction laws in case of combination of slip and spin]. *Mechanics of Solids*. 2003;4:81–89. (In Russ.)
16. Kireenkov AA. Zakon Kulona v obobshchennoi differentsial'noi forme v zadachakh dinamiki tverdykh tel s kombinirovannoi kinematikoi [Coulomb law in generalized differential form in problems of dynamics of rigid bodies with combined kinematics]. *Mechanics of Solids*. 2010;2:15–26. (In Russ.)
17. Gluzman S, Yukalov VI. Self-similarly corrected Pade approximants for nonlinear equations. *Int. J. Mod. Phys. B*. 2020;33(29):1–23.
18. Baker GA, Graves-Morris P. Pade approximations. In: *Encyclopedia of Mathematics and its Applications*, Series no. 59, 2nd ed. Cambridge University Press; 1996. 764 p.
19. Kireenkov AA. Svyazannaya model' treniya skol'zheniya i kacheniya v dinamike tel na sherokhovatoi ploskosti [Combined model of sliding and rolling friction in dynamics of bodies on a rough plane]. *Mechanics of Solids*. 2008;3:116–131. (In Russ.)

Submitted 16.11.2020

Scheduled in the issue 04.02.2021

About the Authors:

Salimov, Maxim S., postgraduate student of the Robotics, Mechatronics, Dynamics and Strength of Machines Department, National Research University “MPEI” (14, Krasnokazarmennaya St., Moscow, 111250, RF), CID: <https://orcid.org/0000-0001-6109-1362>, SalimovMS@mpei.ru

Merkuriev, Igor V., Head of the Robotics, Mechatronics, Dynamics and Strength of Machines Department, National Research University “MPEI” (14, Krasnokazarmennaya St., Moscow, 111250, RF), Dr.Sci. (Eng.), associate professor, Author ID 35422634900, ORCID: <https://orcid.org/0000-0001-7682-2228>, MerkuryevIV@mpei.ru

Claimed contributorship

M. S. Salimov: basic concept formulation; research objectives and tasks; computational analysis; text preparation; formulation of conclusions. I. V. Merkuriev: academic advising; analysis of the research results; the text revision; correction of the conclusions.

All authors have read and approved the final manuscript.

MECHANICS



UDC 539.377: 004.942

<https://doi.org/10.23947/2687-1653-2021-21-1-22-31>
Thick-walled spherical shell problem**A. M. Artemov¹, E. S. Baranovskii¹, A. A. Verlin¹, E. V. Syomka²**¹ Voronezh State University (Voronezh, Russian Federation)² Military Educational and Scientific Center of the Air Force “N. E. Zhukovsky and Y. A. Gagarin Air Force Academy” (Voronezh, Russian Federation)

Introduction. Cylindrical and spherical shells are extensively used in engineering. They face internal and/or external pressure and heat. Stresses and strains distribution in elastoplastic shells has been studied by many scientists. Numerous works involve the use of the von Mises yield conditions, maximum shear stress, maximum reduced stress. These conditions do not include the dependence on the first invariant of the stress tensor and the sign of the third invariant of the stress deviator. In some cases, it is possible to obtain numerical-analytical solutions for stresses, displacements and deformations for bodies with spherical and cylindrical symmetry under axisymmetric thermal and force action.

Materials and Methods. The problem on the state of a thick-walled elastoplastic shell is solved within the framework of the theory of small deformations. A plasticity condition is proposed, which takes into account the dependence of the stress tensor on three independent invariants, and also considers the sign of the third invariant of the stress deviator and translational hardening of the material. A disconnected thermoelastoplastic problem is being solved. To estimate the stresses in the region of the elastic state of a spherical shell, an equivalent stress is introduced, which is similar to the selected plasticity function. The construction of the stress vector hodograph is used as a method for verification of the stress state.

Results. The problem has an analytical solution for linear plasticity functions. A solution is obtained when the strengthening of the material is taken into account. Analytical and graphical relationships between the parameters of external action for the elastic or elastoplastic states of the sphere are determined. For a combined load, variants are possible when the plastic region is generated at the inner and outer boundaries of the sphere or between these boundaries.

Discussion and Conclusions. The calculation results have shown that taking into account the plastic compressibility and the dependence of the plastic limit on temperature can have a significant impact on the stress and strain state of a hollow sphere. In this case, taking into account the first invariant of the stress tensor under the plasticity condition leads to the fact that not only the pressure drop between the outer and inner boundaries of the spherical shell, but the pressure values at these boundaries, can vary within a limited range. In this formulation of the problem, when there is only thermal action, the hollow sphere does not completely pass into the plastic state. The research results provide predicting the behavior of an object (a hollow sphere) that experiences centrally symmetric distributed power and thermal external influences.

Keywords: hollow sphere, thick-walled spherical shell, thermoelastoplastic state, equivalent stress, associated plastic deformation law, stress hodograph, model behavior control parameters.

For citation: A. M. Artemov, E. S. Baranovskii, A. A. Verlin, et al. Thick-walled spherical shell problem. Advanced Engineering Research, 2021, vol. 21, no. 1, p. 22–31. <https://doi.org/10.23947/2687-1653-2021-21-1-22-31>

© Artemov A. M., Baranovskii E. S., Verlin A. A., Syomka E. V., 2021



Introduction. The solution to the problem of a thick-walled spherical shell experiencing different external influences is given in the monographs [1, 2] and a number of scientific papers on the theory of elasticity, plasticity, and thermoelastic plasticity [3-9]. Usually, the case is considered when the loading process is simple.

The problem of a thick-walled spherical shell is one of the simplest elastoplastic problems when the fields of external actions and internal parameters have central symmetry. Due to the central symmetry in the plastic region, the regime of complete plasticity is performed. For an ideal plastic body, the problem is statically definable, which allows it to be solved under any plasticity conditions. In the monograph [1], the most complete solution to the spherical shell problem is given, when the dependence of the plastic limit on temperature is not taken into account, and the plasticity condition does not depend on the first invariant of the stress tensor and the sign of the third invariant of the stress deviator. The cases of only thermal and combined loading are considered, when the temperature on the walls of the sphere is set, the pressure on the inner walls is set, and there is no pressure on the outer wall. In [10-13], thermoelastoplastic state of various objects was studied, and in [3-9], the process of thermal loading and unloading of a sphere free from external forces and a hollow sphere for the Tresca condition was considered with account for the dependence of the plastic limit on temperature. The solution to this and similar problems is of interest since it is possible to obtain an analytical or partially analytical solution for various mathematical models. An analytical solution can be obtained through selecting piecewise linear plasticity functions [11, 13]. Mathematical modeling of objects enables to predict their state and behavior depending on the values of the initial parameters [14, 15].

Materials and Methods. Problem Statement. We consider the problem of a thick-walled spherical shell (a hollow sphere) experiencing centrally symmetric external influences: pressure p_b on the outer wall at $\rho = b$ and pressure p_a on the inner wall at $\rho = a$. The thermal effect on the sphere is also considered: temperature T_a is maintained at the boundary $\rho = a$, temperature T_b is maintained at the boundary $\rho = b$. It is assumed that the sphere exhibits elastic and plastic properties. The desired state parameters at each point of the sphere are the components of the stress tensor, the components of the strain tensors, and the displacement vectors. In the elastic state region, the elastic deformations are complete (there are no residual deformations).

Basic Ratios. All relations are reduced to a dimensionless form. The outer radius of the sphere b is selected as a length scale. All values having the stress dimension are assigned to the plastic limit under uniaxial tension k . The scale unit for temperature is 1 C.

Due to the specified symmetry of external actions, in the spherical coordinate system ρ, θ, ϕ of the matrix, the components of the stress and strain tensor will have the form:

$$(\sigma) = \begin{pmatrix} \sigma_\rho & 0 & 0 \\ 0 & \sigma_\theta & 0 \\ 0 & 0 & \sigma_\phi \end{pmatrix}, \quad (\varepsilon) = \begin{pmatrix} \varepsilon_\rho & 0 & 0 \\ 0 & \varepsilon_\theta & 0 \\ 0 & 0 & \varepsilon_\phi \end{pmatrix}.$$

In this case, the equalities $\sigma_\theta = \sigma_\phi$, $\varepsilon_\theta = \varepsilon_\phi$ are fulfilled.

If the plasticity functions do not depend on the first invariant of the stress tensor and the sign of the third invariant of the stress deviator, then, when solving the sphere problem, the plasticity functions will be reduced to the form:

$$f = |\sigma_\theta - \sigma_\rho| = k. \quad (1)$$

Consider the plasticity condition:

$$f(\sigma_\rho, \sigma_\theta, \varepsilon_\rho^p, \varepsilon_\theta^p) = \frac{\zeta((\sigma_\rho - \delta\varepsilon_\rho^p)^w + 2(\sigma_\theta - \delta\varepsilon_\theta^p)^w)^{\frac{1}{w}}}{\zeta + \eta(1 + \alpha)^{1/m}} + \frac{\eta(|\sigma_\theta - \sigma_\rho - \delta(\varepsilon_\theta^p - \varepsilon_\rho^p)|^m + \alpha(\sigma_\rho - \sigma_\theta - \delta(\varepsilon_\rho^p - \varepsilon_\theta^p))^m)^{\frac{1}{m}}}{\zeta + \eta(1 + \alpha)^{1/m}} = k(T), \quad (2)$$

where ε_ρ^p , ε_θ^p — components of the plastic strain tensor; T — temperature.

When the parameters have the values: $\zeta = 0, \eta = 1, \delta = 0, \alpha = 0, m = 1, \mu = 0, k = k_0$, the condition (2) implies the condition (1). In Fig. 1, the plane σ_p, σ_θ shows the plasticity curves determined from the formula (2) for different values of the numerical coefficients in the plasticity function.

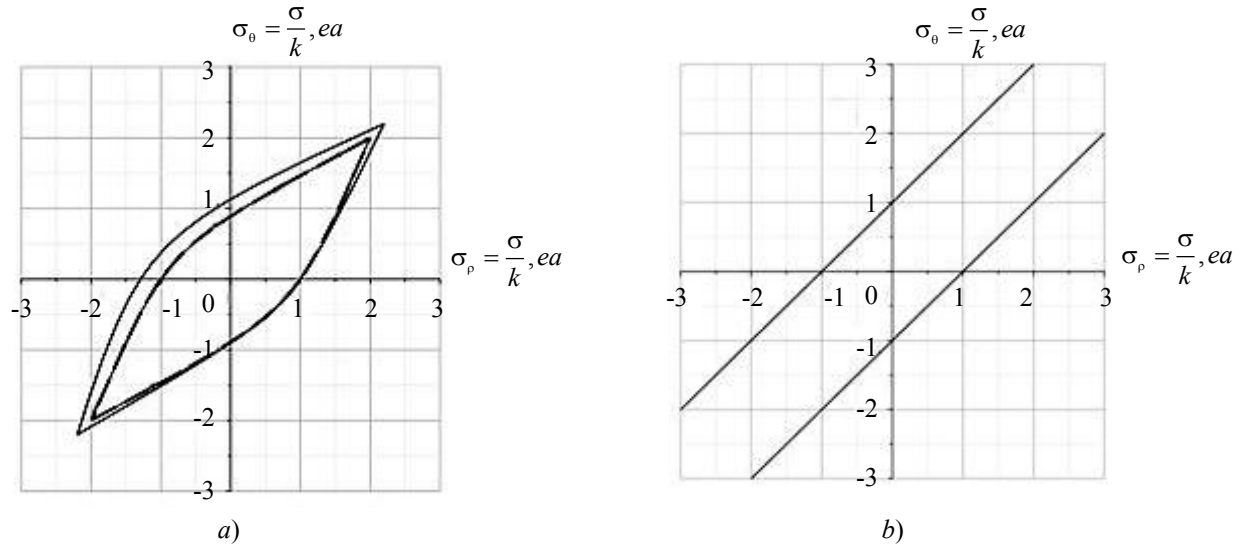


Fig. 1. Plasticity curves: a) for parameters: $\zeta = 0, 2; w = 2; \eta = 0, 5; \delta = 0; m = 3; k = 1$; solid line $\alpha = 0, 5$; dotted line $\alpha = 0$; b) for parameters: $\alpha = 0; \zeta = 0; \delta = 0; k = 1$

The results presented in Fig. 1 show that when the first invariant of the stress tensor is taken into account, the radial and circumferential stresses can vary in a limited range when the point of the sphere is in an elastic state. Accordingly, the pressure on the boundaries of the sphere should also be limited. When the first invariant in the plasticity condition is not taken into account, the elastic state is possible for any pressure value at the boundaries of the sphere, but the pressure drop is limited $\Delta p = p_a - p_b$. Taking into account the sign of the third invariant of the stress deviator, as noted above, affects the values of the plasticity limits.

If the values of the state parameters σ_p, σ_θ determine the point of the region bounded by the plasticity curve, it is assumed that the defining equations connecting stresses and deformations are the relations of the Duhamel-Neumann law [1, 2]:

$$E\varepsilon_\theta = (1-\nu)\sigma_\theta - \nu\sigma_p + E\alpha T, \quad E\varepsilon_p = \sigma_p - 2\nu\sigma_\theta + E\alpha T, \quad (3)$$

where the Young's modulus E and the Poisson's ratio ν are constants.

If the state parameters σ_p, σ_θ determine the points on the plasticity curve, then an additive representation of the total deformations in terms of reversible and irreversible deformations is assumed:

$$\varepsilon_\theta = \varepsilon_\theta^e + \varepsilon_\theta^p, \quad \varepsilon_p = \varepsilon_p^e + \varepsilon_p^p. \quad (4)$$

Complete deformations are determined through displacements from the formulas:

$$\varepsilon_\theta = \frac{u}{\rho}, \quad \varepsilon_p = \frac{du}{d\rho}. \quad (5)$$

Complete deformations are bound by the condition of compatibility of deformations:

$$r \frac{d\varepsilon_\theta}{dr} + \varepsilon_\theta - \varepsilon_p = 0. \quad (6)$$

Increments of irreversible deformations are related to stresses by the normal law:

$$\frac{d\varepsilon_\theta^p}{\partial f / \partial \sigma_\theta} = \frac{d\varepsilon_p^p}{\partial f / \partial \sigma_p}. \quad (7)$$

The relation (7) is generally non-integrable when choosing nonlinear plasticity functions [16]. In the quasi-static approximation, the stresses must satisfy the equilibrium equation:

$$\rho \frac{d\sigma_p}{d\rho} + 2(\sigma_p - \sigma_\theta) = 0. \quad (8)$$

Equivalent Stress. The equivalent stress is the convex isotropic scalar functions of the stress tensor. In special cases, the term “equivalent stress” is synonymous with other terms, for example, “stress intensity” [17]. In this paper,

the equivalent stress coincides with the plasticity function. In this case, the equivalent stress will not have a discontinuity at the elastic-plastic boundary.

Temperature Field. The temperature field in the sphere is found from the solution to the boundary value problem [1]:

$$\begin{cases} \rho \frac{d^2 T}{d\rho^2} + 2 \frac{dT}{d\rho} = 0, \\ T|_{\rho=a} = T_a, \quad T|_{\rho=b} = T_b. \end{cases} \quad (9)$$

The solution to the problem (9) is presented in the form:

$$T = T_b + \frac{a\Delta T}{(b-a)} \left(\frac{b}{\rho} - 1 \right), \quad \Delta T = T_a - T_b. \quad (10)$$

Elastic Area. In the region of the elastic state of a hollow sphere, the formulas for stresses have the form:

$$\sigma_r = A + \frac{B}{\rho^3} - \frac{\lambda}{\rho}, \quad \sigma_\theta = A - \frac{B}{2\rho^3} - \frac{\lambda}{2\rho}, \quad \lambda = \frac{abE\alpha\Delta T}{(1-\nu)(b-a)}.$$

Plastic Area. We select the conditions (1). Let us consider the case of only the thermal effect (10). Then, the plastic region will originate at the inner boundary of the shell under the condition [1]:

$$\beta = \frac{E\alpha}{(1-\nu)} |\Delta T| = \beta_1 = \frac{2(a^2 + ab + b^2)k}{b(a+2b)}.$$

Denote by c_1 — the radius of the elastic-plastic boundary $\rho = c_1$. During the loading process, when $\beta > \beta_1$, the plastic area $a \leq \rho \leq c_1$ increases. When the condition (1) is selected, the stresses in the region $a \leq \rho \leq c_1$ are calculated from the formulas:

$$\sigma_r^{(1)} = 2\kappa_1 k \ln(\rho/a), \quad \sigma_\theta^{(1)} = \sigma_r^{(1)} + \kappa_1 k, \quad \kappa_1 = \text{sign}(\sigma_\theta - \sigma_r),$$

where $\kappa_1 = \text{sign}(\sigma_\theta - \sigma_r)|_{\rho=c_1}$. If $\Delta T > 0$, then $\kappa_1 = -1$, if $\Delta T < 0$, then $\kappa_1 = +1$.

If the region $c_1 \leq \rho \leq b$ remains elastic, then the values A , B and radius of the elastic-plastic boundary c_1 are determined from the conditions of continuity of stresses at the elastoplastic boundary, and the boundary condition $\sigma|_{\rho=b} = 0$. So, if A and B are determined only from the conditions of continuity of stresses at the elastoplastic boundary, then, the following expressions take place:

$$A = 2\kappa_1 k \left(\ln\left(\frac{c_1}{a}\right) + \frac{1}{3} \right) + \frac{\lambda}{3c_1}, \quad B = \frac{\lambda c_1^2}{3} - \frac{2}{3} \kappa_1 k c_1^3. \quad (11)$$

The equation to calculate c_1 will have the form:

$$2\kappa_1 k \left(\ln\left(\frac{c_1}{a}\right) + \frac{1}{3} - \frac{2c_1^3}{3b^3} \right) + \left(\frac{2}{3c_1} + \frac{c_1^2}{3b^3} - \frac{1}{b} \right) \lambda = 0. \quad (12)$$

If A and B are determined from the conditions of continuity of stresses at the elastoplastic boundary, and the conditions $\sigma|_{\rho=b} = 0$, then the following expressions take place:

$$A = \left(1 - \frac{c_1^2}{3b^2} \right) \frac{\lambda}{b} + \frac{2\kappa_1 k c_1^3}{3b^3}, \quad B = \frac{\lambda c_1^2}{3} - \frac{2}{3} \kappa_1 k c_1^3. \quad (13)$$

The choice of formulas (11) or (13) affects the steps of the algorithm for solving the problem, but does not affect the final results.

A second plastic region will be generated at the boundary $\rho = b$ if the following condition is met:

$$(\sigma_\theta - \sigma_r)|_{\rho=b} = \kappa_2 k, \quad \kappa_2 = -\kappa_1. \quad (14)$$

To determine the value $\Delta T = \Delta T_1$, when the condition (14) is satisfied, it is required to combine the system of equations (12), (14). Since the parameter β enters the equations (13) and (1) linearly, it is possible to obtain a separate equation for determining the radius of the elastoplastic boundary:

$$2\kappa_1 k \ln\left(\frac{c_1}{a}\right) + \frac{4\kappa_1 k_0 (b-c_1)(c_1^2 - b^2)}{3(b+c_1)bc_1} = 0, \quad (15)$$

as well as the formula for calculating the parameter β :

$$\beta = \beta_2 = \frac{2k_0(\kappa_2 b^3 - \kappa_1 c_1^3)(b-a)}{(b^2 - c_1^2)ab}. \quad (16)$$

Under further loading, when the inequality $\beta > \beta_2$ is satisfied, the sphere region $c_2 \leq \rho \leq b$ goes into a plastic state at the boundary $\rho = b$.

A hollow sphere when exposed to heat. Consideration of material hardening. Consider the case when the plasticity condition has the form:

$$f(\sigma_\rho, \sigma_\theta, \varepsilon_\rho^p, \varepsilon_\theta^p) = |\sigma_\theta - \sigma_\rho - \delta(\varepsilon_\theta^p - \varepsilon_\rho^p)| = k. \quad (17)$$

If there are no residual deformations in the sphere before loading, then as a result of thermal heating, the plastic zone will be generated at the inner boundary $\rho = a$, when the conditions (15), (16) are met. With further loading, plastic region $a \leq \rho \leq c_1$ is formed. To find the stresses in this region, it is required to get the corresponding equations from the system of equations (3-6), (8), (17):

$$\begin{cases} \rho^2 \frac{d^2 \sigma_\rho}{d\rho^2} + 4\rho \frac{d\sigma_\rho}{d\rho} - \frac{6}{1+3\delta(1-\nu)} \left(k + \frac{\delta ab E \alpha \Delta T}{\rho(b-a)} \right) = 0, \\ \sigma_\theta = \frac{\rho}{2} \frac{d\sigma_\rho}{d\rho} + \sigma_\rho. \end{cases} \quad (18)$$

The solution to the system (18) is written as:

$$\begin{aligned} \sigma_\rho &= \frac{1}{1+3\delta(1-\nu)} \left(2k \ln \rho - \frac{3\delta ab E \alpha \Delta T}{\rho(b-a)} \right) - \frac{C_1}{\rho^3} + C_2, \\ \sigma_\theta &= \frac{1}{1+3\delta(1-\nu)} \left(k + 2k \ln \rho - \frac{3\delta ab E \alpha \Delta T}{2\rho(b-a)} \right) + \frac{C_1}{2\rho^3} + C_2. \end{aligned} \quad (19)$$

The values C_1, C_2 , included in the formulas (19), are determined from the boundary condition $\sigma_\rho|_{\rho=a} = 0$ and the condition for the absence of plastic deformations at the elastic-plastic boundary $\rho = c_1$:

$$\begin{aligned} C_1 &= 2\kappa_1(k - k_\delta)c_1^3 - 3E\alpha N_\delta c_1^2, \\ C_2 &= 2\kappa_1 k_\delta \ln a + \frac{2\kappa_1(k - k_\delta)c_1^3}{3a^3} + \frac{E\alpha N_\delta}{a} \left(3 - \frac{c_1^2}{a^2} \right), \\ N_\delta &= \frac{\delta ab \Delta T}{(1+3\delta(1-\nu))(b-a)}. \end{aligned} \quad (20)$$

As a result of substituting (20) in (19), we get:

$$\begin{aligned} \sigma_\rho &= \frac{1}{1+3\delta(1-\nu)} \left(2\kappa_1 k \ln \frac{\rho}{a} + \frac{3\delta ab E \alpha \Delta T}{b-a} \left(\frac{1}{a} - \frac{1}{\rho} \right) - \right. \\ &\quad \left. - \left(\frac{2\kappa_1 k c_1^3}{3} + \frac{\delta ab c_1^2 E \alpha \Delta T}{b-a} \right) \left(\frac{1}{a^3} - \frac{1}{\rho^3} \right) \right) + \frac{2\kappa_1 k c_1^3}{3} \left(\frac{1}{a^3} - \frac{1}{\rho^3} \right), \\ \sigma_\theta &= \frac{1}{1+3\delta(1-\nu)} \left(\kappa_1 k + 2\kappa_1 k \ln \frac{\rho}{a} + \frac{3\delta ab E \alpha \Delta T}{b-a} \left(\frac{1}{a} - \frac{1}{2\rho} \right) - \right. \\ &\quad \left. - \left(\frac{\kappa_1 k c_1^3}{3} + \frac{\delta ab c_1^2 E \alpha \Delta T}{2(b-a)} \right) \left(\frac{2}{a^3} + \frac{1}{\rho^3} \right) \right) + \frac{\kappa_1 k c_1^3}{3} \left(\frac{2}{a^3} + \frac{1}{\rho^3} \right). \end{aligned}$$

From the solution to the elastic problem, it follows: if $\Delta T > 0$, then $\kappa_1 = -1$; if $\Delta T < 0$, then $\kappa_1 = +1$.

Accounting for plastic compressibility. Consider the case when the plasticity function is linear with respect to the components of the stress tensor:

$$\begin{aligned} \zeta(2\sigma_\theta + \sigma_\rho) + \kappa(\sigma_\theta - \sigma_\rho) + \eta(\sigma_\theta - \sigma_\rho) &= k_0(1 - \chi T), \\ \kappa &= \text{sign}(\sigma_\theta - \sigma_\rho). \end{aligned} \quad (21)$$

The plasticity condition (21) can be represented as:

$$\begin{aligned} \alpha \sigma_\theta + \beta \sigma_\rho &= k(1 - \chi T), \\ \alpha &= 2\zeta + \kappa - \eta, \\ \beta &= \zeta - \kappa + \eta. \end{aligned}$$

Taking into account the introduced notation, to determine the stresses in the plastic region, we obtain the problem:

$$\begin{cases} \alpha\sigma_\theta + \beta\sigma_\rho = k(1-\chi T), \\ \rho \frac{d\sigma_\rho}{d\rho} + 2(\sigma_\rho - \sigma_\theta) = 0, \\ \sigma_\rho|_{\rho=a} = -p_a. \end{cases} \quad (22)$$

The solution to the problem (22) has the form:

$$\begin{aligned} \sigma_\rho &= \left(-p_a + \frac{(M_\chi - 1)k_0}{\alpha + \beta} + \frac{2N_\chi k_0}{a(\alpha + 2\beta)} \right) \left(\frac{a}{\rho} \right)^{2+2\beta/\alpha} - \left(\frac{M_\chi - 1}{\alpha + \beta} + \frac{2N_\chi}{\rho(\alpha + 2\beta)} \right) k_0, \\ \sigma_\theta &= -\frac{\beta}{\alpha} \left(-p_a + \frac{(M_\chi - 1)k_0}{\alpha + \beta} + \frac{2N_\chi k_0}{a(\alpha + 2\beta)} \right) \left(\frac{a}{\rho} \right)^{2+2\beta/\alpha} - \left(\frac{M_\chi - 1}{\alpha + \beta} + \frac{N_\chi}{\rho(\alpha + 2\beta)} \right) k_0, \end{aligned} \quad (23)$$

where the notation is introduced: $M = T_b - \frac{a\Delta T}{b-a}$, $N = \frac{ab\Delta T}{b-a}$, $M_\chi = \chi M$, $N_\chi = \chi N$.

To get the correct result from (20), when, for example, $\alpha + \beta = 0$, it is required to perform a limit transition when solving (22). It is easier to obtain the correct result directly in (23), while taking into account that the condition $\alpha + \beta = 0$ is met. In this case $\zeta = 0$, so we get:

$$\begin{aligned} \sigma_\rho &= \frac{2k_0}{\alpha} \left((1 - M_\chi) \ln \frac{\rho}{a} + \left(\frac{1}{\rho} - \frac{1}{a} \right) N_\chi \right) - p_a, \\ \sigma_\theta &= \frac{k_0}{\alpha} \left((1 - M_\chi) \left(1 + \ln \frac{\rho}{a} \right) + N_\chi \left(\frac{1}{\rho} - \frac{2}{a} \right) \right) - p_a. \end{aligned}$$

During the loading process, the plastic zone originates at the boundary $\rho = a$, when the following condition is met:

$$\Delta T = k_0(1 - \chi T_b) / \left(k_0 \chi - \frac{(2\zeta + \kappa - \eta)(a + 2b)bE\alpha}{2(1 - \nu)(a^2 + ab + b^2)} \right).$$

Research Results. Fig. 2 shows stress graphs and stress vector hodographs, when the sphere region corresponding to the condition $a \leq \rho \leq c_1$, is in a plastic state, and the sphere region corresponding to the condition $c_1 \leq \rho \leq b$, is in an elastic state.

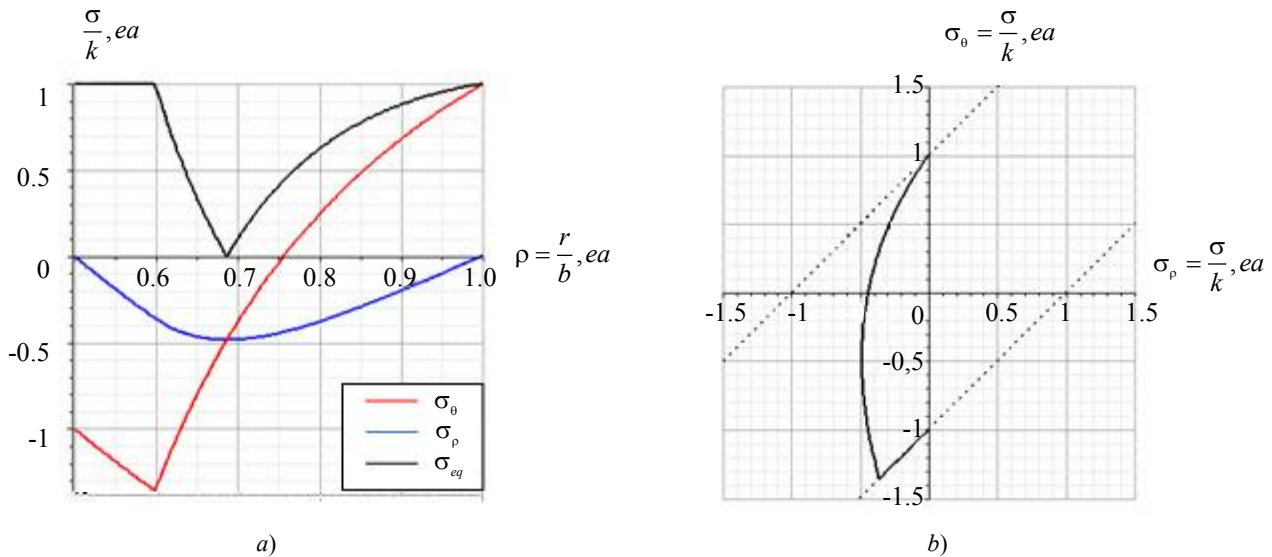


Fig. 2. Stress graphs (a) and stress vector hodographs (b) for parameter values: $k = 1$; $\nu = 0.3$; $a = 0.5$; $b = 1$; $\Delta T = 170$; $c_1 = 0.57$

Fig. 3 shows stress graphs and stress vector hodographs, when the sphere regions corresponding to the conditions $a \leq \rho \leq c_1$ and $c_2 \leq \rho \leq b$, are in a plastic state, and the sphere region corresponding to the condition $c_1 \leq \rho \leq c_2$, is in an elastic state.

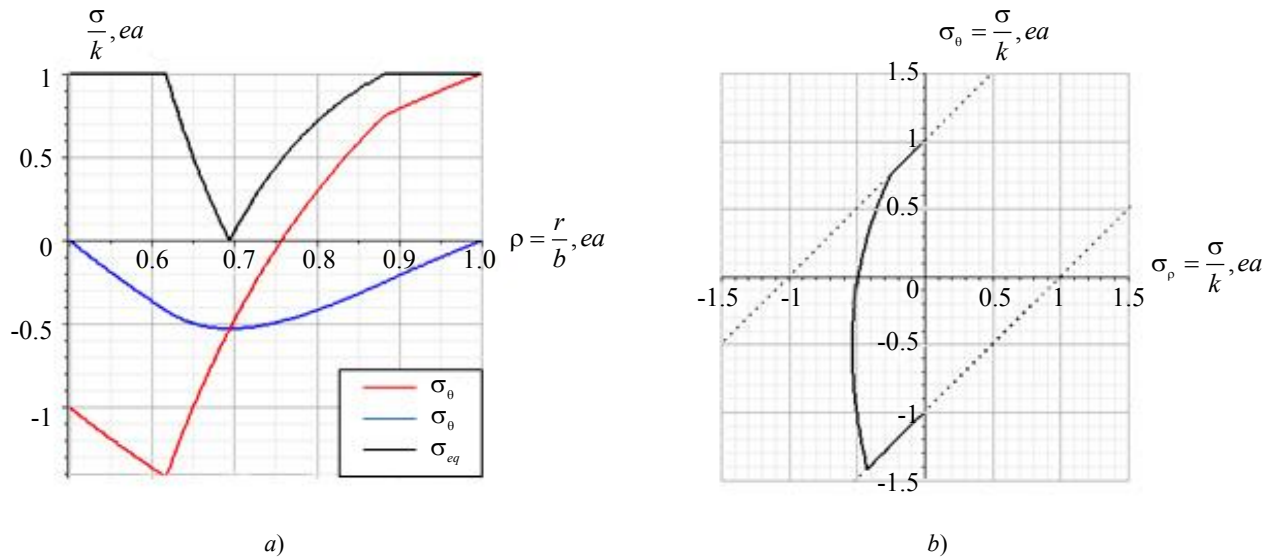


Fig. 3. Stress graphs (a) and stress vector hodographs (b) for parameter values:
 $\nu = 0.3$; $a = 0.5$; $\Delta T = 270$; $c_1 = 0.62$; $c_2 = 0.88$

Fig. 4 shows stress graphs and stress vector hodographs, when the sphere region corresponding to the condition $a \leq \rho \leq c_1$, is in a plastic state, and the sphere region corresponding to the condition $c_1 \leq \rho \leq b$, is in an elastic state.

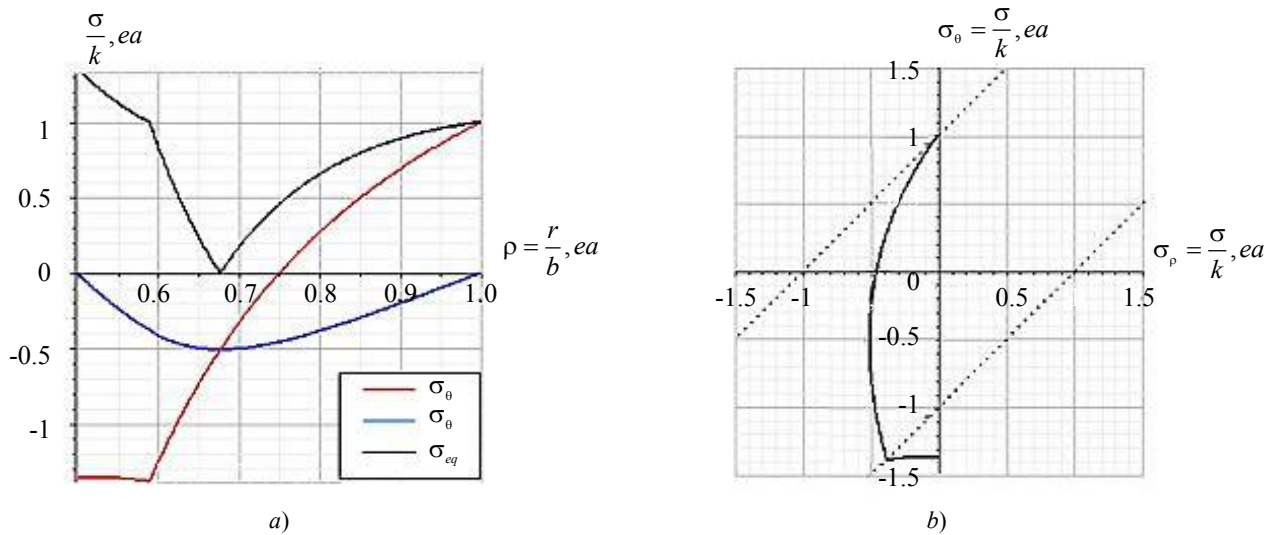


Fig. 4. Stress graphs (a) and stress vector hodographs (b) for parameter values:
 $\nu = 0.3$; $a = 0.5$; $\Delta T = 215$; $c_1 = 0.58$

Fig. 5 shows stress graphs and stress vector hodographs, when the sphere regions corresponding to the conditions $a \leq \rho \leq c_1$ and $c_2 \leq \rho \leq b$, are in a plastic state, and the sphere region corresponding to the condition $c_1 \leq \rho \leq c_2$, is in an elastic state.

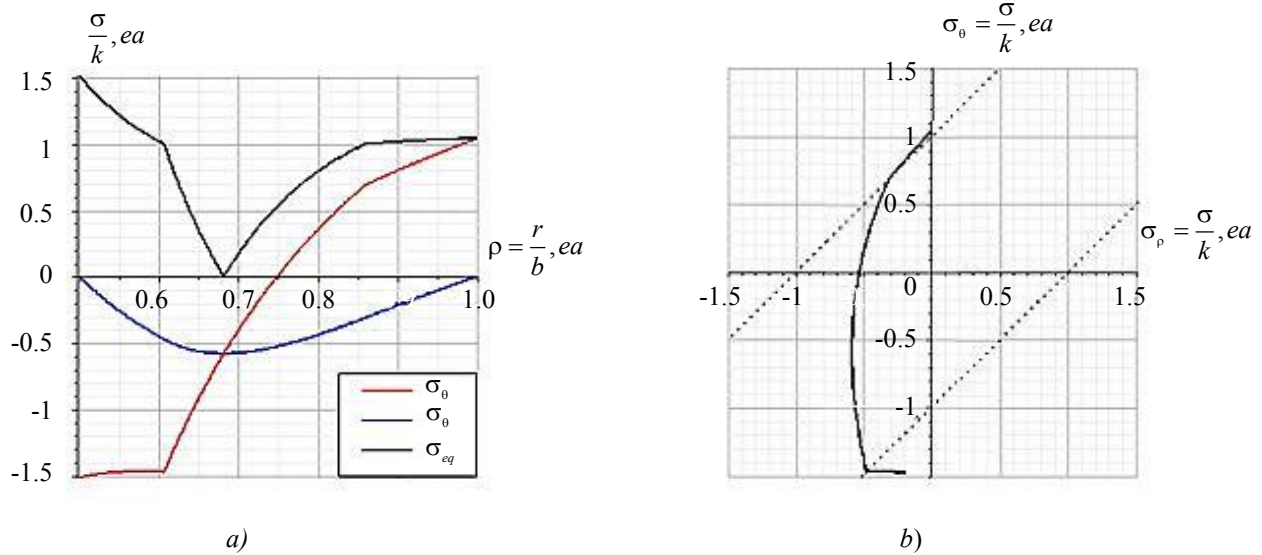


Fig. 5. Stress graphs (a) and stress vector hodographs (b) for parameter values:
 $\nu = 0.3$; $a = 0.5$; $\Delta T = 270$; $c_1 = 0.61$; $c_2 = 0.86$

Fig. 6 shows stress graphs and stress vector hodographs when the sphere regions corresponding to the conditions $a \leq \rho \leq c_1$ and $c_2 \leq \rho \leq b$, are in a plastic state, and the sphere region corresponding to the condition $c_1 \leq \rho \leq c_2$, is in an elastic state.

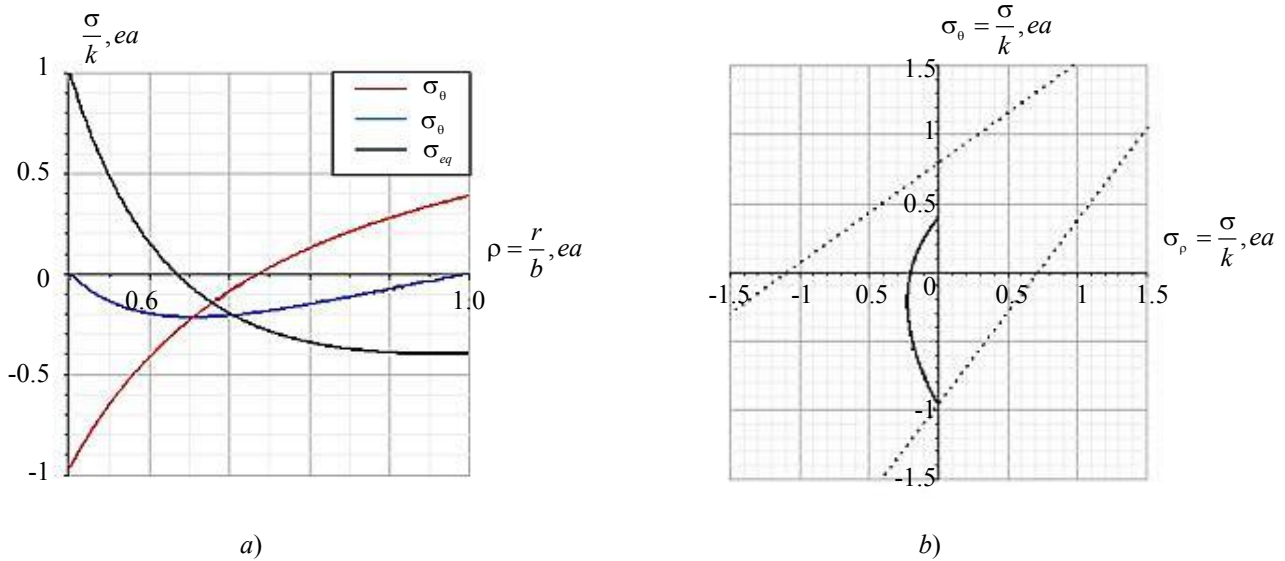


Fig. 6. Stress graphs (a) and stress vector hodographs (b) for parameter values:
 $\nu = 0.3$; $a = 0.5$; $\Delta T = 79$; $\zeta = 0.1$; $\eta = 0.1$; $E\alpha = 0.012$; $\chi = 0.0017$

Discussion and Conclusions. The calculation results show that in this formulation of the problem, when there is only thermal action, the hollow sphere does not completely go into the plastic state (Fig. 2-6). Hardening causes an increase in the equivalent stress in the plastic region and a decrease in the radius of the elastoplastic boundary (Fig. 4, 5). The elastic region cannot completely disappear under loading. Plastic compressibility and the dependence of the plastic limit on temperature have a significant effect on the stress state of the hollow sphere (Fig. 6).

References

1. Chakrabarty J. Theory of Plasticity. Oxford: Elsevier Butterworth-Heinemann; 2006. 882 p.
2. Parkus G. Neustanovivshiesya temperaturnye napryazheniya [Unsteady temperature stresses]. Moscow: Fizmatlit; 1963. 252 p. (In Russ.)
3. Gamer U. On the elastic-plastic deformation of a sphere subjected to a spherically symmetrical temperature field. Journal of Thermal Stresses. 1988;11(3):159–173.
4. Dats EP, Mokrin SN, Murashkin EV. Raschet nakoplennoi ostatochnoi deformatsii v protsesse <nagrevakh-lazhdeniya> uprugoplasticheskogo shara [The calculation of the accumulated residual strain in the heating-cooling

process of elasto-plastic ball]. Bulletin of the Yakovlev Chuvash State Pedagogical University. Series: Mechanics of Limit State. 2012;4:123–132. (In Russ.)

5. Murashkin EV, Dats EP. Termouprugoplasticheskoe deformirovanie mnogosloinogo shara [Thermoelasto-plastic deformation of multilayer ball]. Izvestiya RAN. Mekhanika Tverdogo Tela = Mechanics of Solids. 2017;5:30–36. (In Russ.)

6. Dats EP, Murashkin EV, Velmurugan R. Vychislenie neobratimyykh deformatsii v polom uprugoplasticheskoy share v usloviyakh nestatsionarnogo temperaturnogo vozdeistviya [On computing irreversible strains of the hollow ball under unsteady thermal action]. Bulletin of the Yakovlev Chuvash State Pedagogical University. Series: Mechanics of Limit State. 2015;3:168–175. (In Russ.)

7. Kovalev AV, Khvostov IG. Ob opredelenii napryazhenii i peremeshchenii v uprugom prostranstve, oslablenno sfericheskoy polost'yu, s ucheto temperatury [On the determination of stresses and displacements in an elastic space weakened by a spherical cavity taking into account temperature]. Bulletin of the Yakovlev Chuvash State Pedagogical University. Series: Mechanics of Limit State. 2014;2:29–35. (In Russ.)

8. Burenin AA, Murashkin EV, Dats EP. Residual stresses in AM fabricated ball during a heating process. AIP Conference Proceedings. 2018;1959(1):070008. URL: <https://doi.org/10.1063/1.5034683>

9. Syomka E. Uprugoplasticheskoe sostoyanie pologo shara [Elastoplastic state of a hollow sphere]. The Far Eastern Federal University: School of Engineering Bulletin. 2020;3:3–12. (In Russ.)

10. Burenin AA, Tkacheva AV. Kusочно-lineinye plasticheskie potentsialy kak sredstvo raschetov ploskikh neustanovivshikhsya temperaturnykh napryazhenii [Piecewise linear plastic potentials as a means of calculating plane unsteady temperature stresses]. Izvestiya RAN. Mekhanika Tverdogo Tela = Mechanics of Solids. 2020;6:40–49. (In Russ.)

11. Burenin AA, Tkacheva AV, Scherbatyuk GA. Ispol'zovaniyu kusочно-lineinykh plasticheskikh potentsialov v nestatsionarnoy teorii temperaturnykh napryazhenii [The use of piecewise linear plastic potentials in the nonstationary theory of temperature stresses]. Journal of Samara State Technical University. Ser. Physical and Mathematical Sciences. 2018;22(1):23–39. (In Russ.)

12. Dats EP, Murashkin EV, Tkacheva AV, et al. Temperaturnye napryazheniya v uprugoplasticheskoy trube v zavisimosti ot vybora usloviya plastichnosti [Temperature stresses in an elastic-plastic pipe depending on the selection of the plasticity condition]. Izvestiya RAN. Mekhanika Tverdogo Tela = Mechanics of Solids. 2018;1:32–43. (In Russ.)

13. Dats EP, Murashkin EV. Temperaturnye napryazheniya v usloviyakh toroidal'noi simmetrii [Thermal stresses under toroidal symmetry]. Bulletin of the Yakovlev Chuvash State Pedagogical University. Series: Mechanics of Limit State. 2019;2:57–70. (In Russ.)

14. Aleksandrova NN, Artemov MA, Baranovskii ES, et al. On stress/strain state in a rotating disk. AMCSM_2018 IOP Conf. Series: Journal of Physics: Conf. Series. 2019;1203:012001. URL: <http://doi.org/10.1088/1742-6596/1203/1/012001>

15. Semka EV, Artemov MA, Babkina YN, et al. Mathematical modeling of rotating disk states. In: Proc. Conf. 2019 Applied Mathematics, Computational Science and Mechanics: Current Problems, Voronezh, Russian Federation. 2020;1479:012122.

16. Ishlinskii AYU, Ivlev DD. Matematicheskaya teoriya plastichnosti [Mathematical theory of plasticity]. Moscow: Fizmatlit; 2001. 704 p. (In Russ.)

17. Khan Kh. Teoriya uprugosti. Osnovy lineinoi teorii i ee primenenie [Theory of elasticity. Fundamentals of linear theory and its application]. Moscow: Mir; 1988. 343 p. (In Russ.)

Submitted 28.12.2020

Scheduled in the issue 04.02.2021

About the Authors:

Artemov, Mikhail A., Head of the Software Development and Information Systems Administration Department, Voronezh State University (1, Universitetskaya Sq., Voronezh, 394018, RF), Dr.Sci. (Phys.-Math.), professor, ResearcherID [O-1965-2015](https://orcid.org/0000-0001-8356-5418), ScopusID [6603631575](https://orcid.org/0000-0001-8356-5418), ORCID: <http://orcid.org/0000-0001-8356-5418>, artemov_m_a@mail.ru

Baranovsky, Evgeny S., associate professor of the Software Development and Information Systems Administration Department, Voronezh State University (1, Universitetskaya Sq., Voronezh, 394018, RF), Cand.Sci. (Phys.-Math.), associate professor, ResearcherID [L-6233-2016](#), ScopusID [36503487200](#), ORCID: <http://orcid.org/0000-0002-1514-4475>, esbaranovskii@gmail.com

Verlin, Alexander A., postgraduate student of the Software Development and Information Systems Administration Department, Voronezh State University (1, Universitetskaya Sq., Voronezh, 394018, RF), ORCID: <https://orcid.org/0000-0001-9771-340X>, alexandrverlin@mail.ru

Syomka, Eleonora V., lecturer of the Radioelectronics Department, Military Educational and Scientific Center of the Air Force “N.E. Zhukovsky and Y.A. Gagarin Air Force Academy” (54a, Starykh Bol’shevikov St., Voronezh, 394064, RF), ORCID: <https://orcid.org/0000-0002-0194-6979>, semka_elya@mail.ru

Claimed contributorship

M. A. Artemov: basic concept formulation; research objectives and tasks; formulation of conclusions.
E. S. Baranovsky: academic advising; the text revision; correction of the conclusions. A. A. Verlin: text preparation.
E. V. Syomka: computational analysis; analysis of the research results.

All authors have read and approved the final manuscript.

MECHANICS



UDC 531.36

<https://doi.org/10.23947/2687-1653-2021-21-1-32-42>

Material point physical model rationale while studying kinematic characteristics of a motor vehicle in case of oblique collision with side cable barriers



G. P. Kolesnikova

Peter the Great Military Academy of the Strategic Missile Troops (Balashikha, Russian Federation)

Introduction. A review of the application of theoretical mechanics methods for the development of algorithms of approximate analytical simulation of a motor vehicle (MV) movement in case of oblique collision with side cable barriers is performed. The representation of the MV as a material point in this type of collision is validated. The study objective is to demonstrate the application of a physical model of a material point to describe the motor vehicle dynamics in the event of its oblique collision with side cable barrier.

Materials and Methods. A new physical model that describes the opposition to the motor vehicle movement from the side of a cable barrier in an oblique collision is proposed. New methods of approximate analytical construction of the MV movements during an oblique collision with the side cable barriers are presented. The analytical calculation results are verified by the data of the finite element (FE) simulation of the collision according to the data of field tests. The FE simulation was carried out using a multi-purpose finite element complex LS-Dyna.

Results. New analytical algorithms have been developed for the MV movement in case of an oblique collision with side cable barriers, as well as a new physical model describing the opposition to the MV movement from the side of cable barriers. The application of a physical model of a material point to study the motor vehicle dynamics during an oblique collision with side cable barriers is established scientifically, including the comparative analysis of the kinematic results of the virtual test with kinematic calculations obtained on the basis of algorithms for analytical construction of the MV movements.

Discussion and Conclusions. The analysis of the kinematic results of the virtual test in comparison with the analytical kinematic calculations has shown that the representation of a motor vehicle as a material point in case of an oblique collision with side cable barriers is reasonable since the MV movement is close to translational motion. The results obtained can be used in the development and analysis of the correctness of the FE modeling of a side collision of a motor vehicle with cable barriers.

Keywords: cable barrier, analytical modeling, motion trajectory, displacements, material point, motor vehicle, oblique collision.

For citation: G. P. Kolesnikova. Material point physical model rationale while studying kinematic characteristics of a motor vehicle in case of oblique collision with side cable barriers. Advanced Engineering Research, 2021, vol. 21, no. 1, p. 32–42. <https://doi.org/10.23947/2687-1653-2021-21-1-32-42>

© Kolesnikova G. P., 2021



Introduction. Safety systems designed for the organization of traffic flows on road routes help to minimize the adverse consequences of road traffic accidents (RTA). Currently, cable road barriers are gaining popularity. They are installed on the road dividing strip to prevent intentional and unintentional crossing of the road by vehicles, as well as

on the roadsides, to prevent the departure of vehicles outside the road¹. Different structures of cable barriers consist of common elements: cables, racks, anchor blocks, clamping devices, but differ in the type of their installation² [1-4], in particular, in the method of fastening the cables (Fig. 1), which significantly affects the development of mathematical models. The behavior of the racks under the MV collision is also different. Racks can be crushed or, coming out of the sleeves, assembled with one another, and thus provide additional braking of the MV [5].

The collision of a car with a cable barrier is characterized by complex interaction mechanics, since the cables have a high degree of geometric nonlinearity, and the racks and the ground have a high degree of physical nonlinearity, while almost all processes are transient [5].



Fig. 1. Some types of cable racks [6]

To determine the MV trajectory, string vibration equations can be used in the analytical calculations of arresters^{3,4} and cable-stayed structures^{5,6}. But due to the complexity of the construction of barriers, there are difficulties in the formulation of boundary conditions. Energy methods also give a set of equations that are not solved analytically⁷ [7]. All this causes the need to study barriers with the help of engineering software packages for both modeling the cable barrier itself and the crash test system. In this case, the numerical finite element method in the explicit formulation is often used, which is implemented in the software complexes LS-DYNA, MARC, NASTRAN, etc. [5, 8, 9].

The disadvantages of building FE models are the following: the development complexity; the duration of the calculation period (120 hours or more); the need to check the correctness of the construction. Thus, the period of preparation of the basis for the study is quite long. In this regard, a method of approximate analytical calculation of the MV movement from the data of field tests, based on the methods of theoretical mechanics, is proposed. The analytical calculation provides checking the correctness of the developed FE model, as well as reducing the time of the passive safety study by 2-3 times, since for the analysis of passive safety, it is no longer necessary to build a FE model of the cable barrier itself, but to use the analytically obtained movements.

Materials and Methods. As a result of observing the MV during full-scale crash tests, a hypothesis was put forward: in case of the collision with the side cable barriers, the MV can be represented as a solid body making a translational motion (Fig. 2).

¹ Industry road methodological document ODM 218.6.017-2015. Guidelines for the use of road barriers of various types on federal highways, recommended by the order of the Federal Road Agency, dated December 23, 2015, no. 2489-r. URL: <https://files.stroyinf.ru/Data2/1/4293757/4293757596.pdf> (accessed: 08.01.2021). (In Russ.)

² Horne DA. Report 350 Acceptance of New York Three-Strand Cable Terminal. Office of Highway Safety Infrastructure, FHWA, U.S. Department of Transportation – Washington, D.C.; February 14, 2000. Available from: <https://highways.dot.gov/> (accessed: 21.01.2019).

³ Nuralieva AB. On dynamics of the space elevator cable: Cand.Sci. (Phys.-Math.), diss., author's abstract. Moscow, 2012. 20 p. (In Russ.)

⁴ Mikhailyuk DS. Finite element modeling and research on the dynamics of a deck arrester: Cand.Sci. (Eng.), diss., author's abstract. St. Petersburg, 2009. 19 p. (In Russ.)

⁵ Dyadkin SN. Rationale, technology of balanced erection and monitoring of byte bridge spans with account for climatic factors (case study: the bridge over the Ob River near Surgut): Cand.Sci. (Eng.), diss., author's abstract. Volgograd, 2005. 20 p. (In Russ.)

⁶ Le Thu Huong. Optimization of parameters of spans of suspension bridges, reinforced and not reinforced with inclined cables, when designing them with using PC: Cand.Sci. (Eng.), diss., author's abstract. Moscow, 1999. 25 p. (In Russ.)

⁷ Los MV. Numerical modeling of the behavior of the "body-rope" system with account for flexural rigidity of the cable and mechanism of looping: Cand.Sci. (Phys.-Math.), diss., author's abstract. Moscow, 2000. 19 p. (In Russ.)

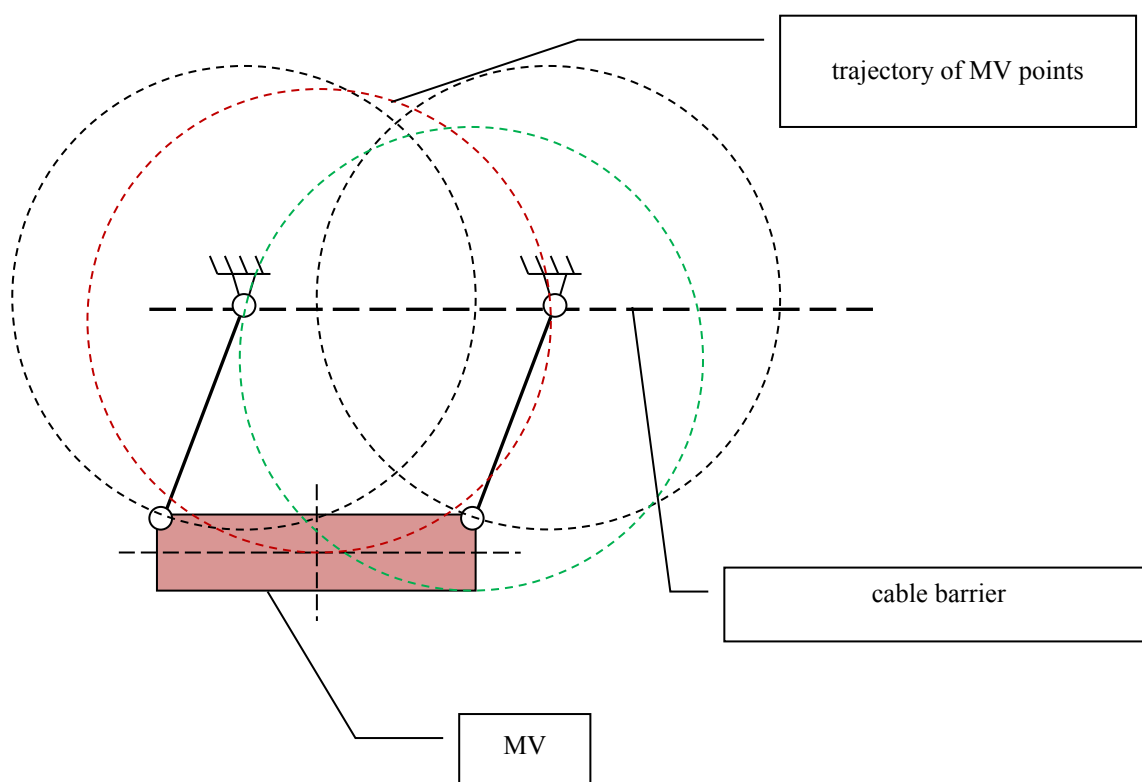


Fig. 2. The model of MV as a solid body performing translational motion

In addition, a number of fundamental assumptions on the dynamics of the MV during an accident are made, justifying the use of the proposed theoretical and mechanical models of the phenomenon:

- the lateral and longitudinal decelerations of the vehicle are constant during the time interval required for the MV to be oriented parallel to the undeformed barrier;
- vertical and rotational accelerations of the vehicle are ignored;
- the lateral component of the speed is zero after the vehicle is redirected parallel to the guardrail;
- as the vehicle is being redirected, it does not engage with the guardrail;
- the deformation of the vehicle occurs in the collision zone, but its center-of-gravity position does not change significantly;
- the MV center of mass moves as if all its mass is concentrated at this point;
- the barrier can be rigid or flexible;
- the friction forces of the car tires on the road surface are ignored;
- the guardrail system does not contain breaks that can cause sudden vertical movements of the vehicle.

With this representation of motion, a MV (Fig. 3) can be considered as a material point of some mass m [10]. The Cartesian coordinate system origin corresponds to the point of origin of contact between the vehicle and the barrier. The motion of the material point begins with at the speed \vec{v}_0 , directed at an angle α to the plane of the fence (x -axis) [6].

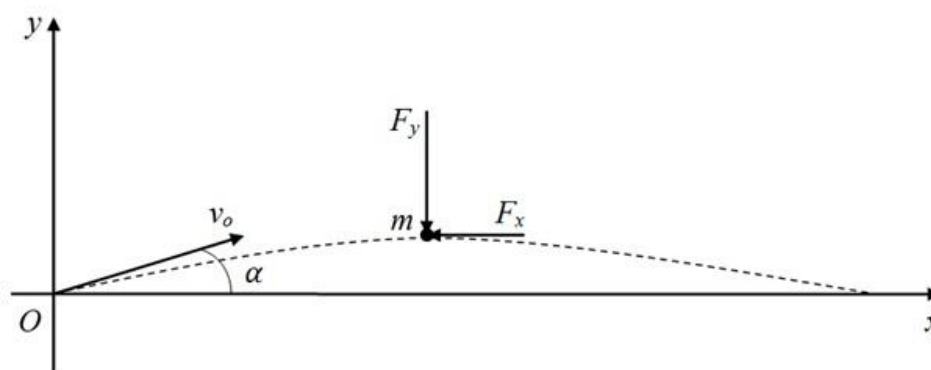


Fig. 3. Calculation scheme of MV [6]

The opposition to the movement of the vehicle from the side of the cable barrier was modeled by the forces [6]:

- with lateral deviation along the y -axis — by the elastic force $P_y = -ky$ and dissipative resistance $P_y^{duc} = -b\dot{y}$, i.e., $F_y = -ky - b\dot{y}$;
- the opposition to movement along the x -axis — by the force of friction $F_x = -fN_l$, where N_l — the force of inertial pressure, i.e., $N_l = m\ddot{y}$ [6].

As a result, the MV motion is described by a system of differential equations [6, 11]:

$$\begin{cases} \ddot{x} = -f\ddot{y}; \\ \ddot{y} + 2\varepsilon\dot{y} + p^2y = 0. \end{cases}$$

The solution to the system is displacement as a function of time t :

$$\begin{cases} x(t) = -f y(t) + v_0 (\cos \alpha + f \sin \alpha) t; \\ y(t) = \frac{v_0 \sin \alpha}{p} e^{-\varepsilon t} \sin pt. \end{cases}$$

In [6], it is proved that the Coulomb friction force from the side of the road barrier does not significantly affect the simulated the MV motion. Physical modeling of the MV as a material point is not new under studying the case of collision with lateral barriers. This approach was used by R. M. Olson, E. R. Post and F. F. McFarland when describing a car hitting a rigid bridge guardrail [12]. Here, the calculation of the side barrier resistance was based only on the classical Amontons-Coulomb model of friction.

In contrast to the problem, the nature of the interaction between the MV and the barrier is described in this paper by a fundamentally new model. With the external similarity of the problem statement, the physical essence of the interaction between the MV and the barrier differs qualitatively from the essence of the interaction with more rigid fences. In our paper, this was taken into account through the Amontons-Coulomb force models considering the force of the inertial normal pressure and the Kelvin-Voigt resistance model.

Also, in the context of the study on the nature of the impact on cable barriers, the paper by M. B. Bateman and others should be mentioned [9]. The data of full-scale tests presented in this work demonstrate clearly that in case of oblique collision with cable barriers, the MV motion is close to translational one, when the yaw angle does not exceed 10° . Here, the head-on crash process is described by two models:

1. A simple dynamic model of a vehicle, where the Runge-Kutta fourth-order method was used for the numerical solution to the differential equation of the MV motion. In this case, the forces of action from the side of the barrier (cable tension) and the road (friction force according to the classical Amontons-Coulomb model) are considered. The wheels are not assumed to require steering under impact.
2. A quasistatic model of the barrier, which is designed to calculate the change in tension of the cables when their geometry changes as a result of the movement of the car.

As a result, the computational model is quite cumbersome and requires a numerical solution, whereas the model proposed in this paper provides calculation algorithms that are easily carried out analytically without the use of numerical methods.

Approximate analytical calculation of the MV kinematic characteristics. As a result of the assumptions made, an algorithm for constructing the MV motion called harmonic has been obtained [6]. Further, we propose quadratic and cubic algorithms based on the construction of polynomial displacement functions [13].

Here, the opposition to the MV motion from the side of cable barriers along the y -axis is determined by some function $P_y(t)$, the result of its integrating is as follows: the MV displacement function along the y -axis has the character of a second or third order polynomial. The simulation of the opposition to the movement along the x -axis remains the same.

We will conduct a comparative analysis of the results of the approximate analytical calculation of the MV kinematic characteristics. Fig. 4-6 show the computation data for bus Mercedes-Benz O345. When constructing the movements of the MV, data of field tests of the State Research Center of the Russian Federation FSUE "NAMI" were used.

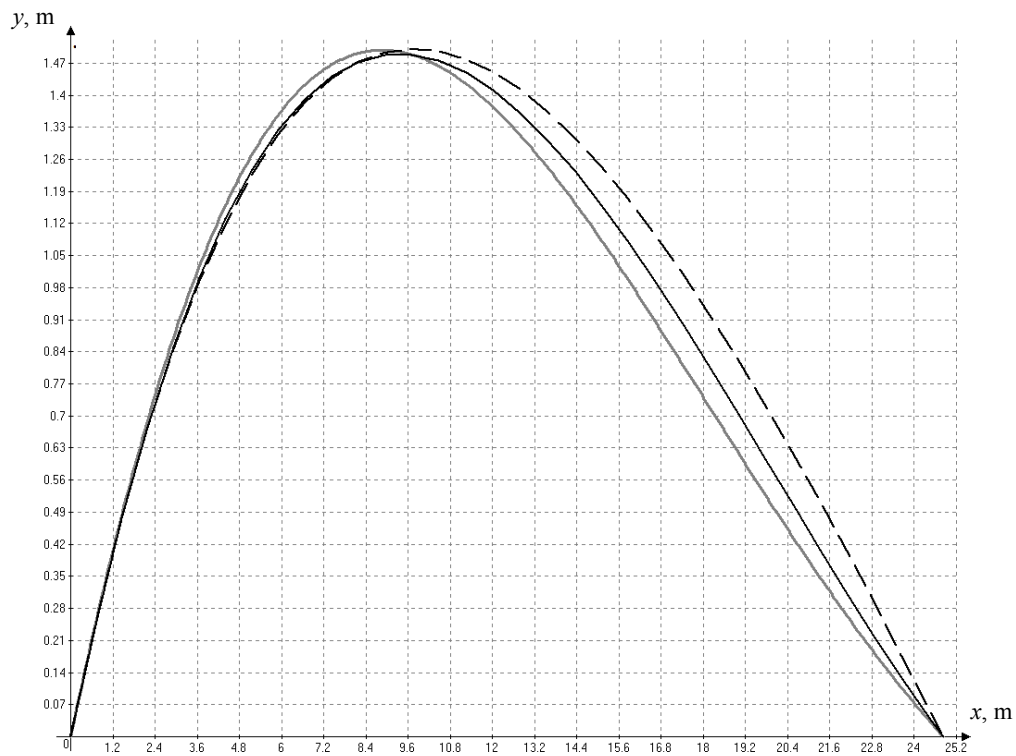


Fig. 4. Interdependence of the deviations x , m, and y , m, calculated by the methods of cubic approximation — black solid line; quadratic approximation — dotted line; harmonic approximation — gray line [13]

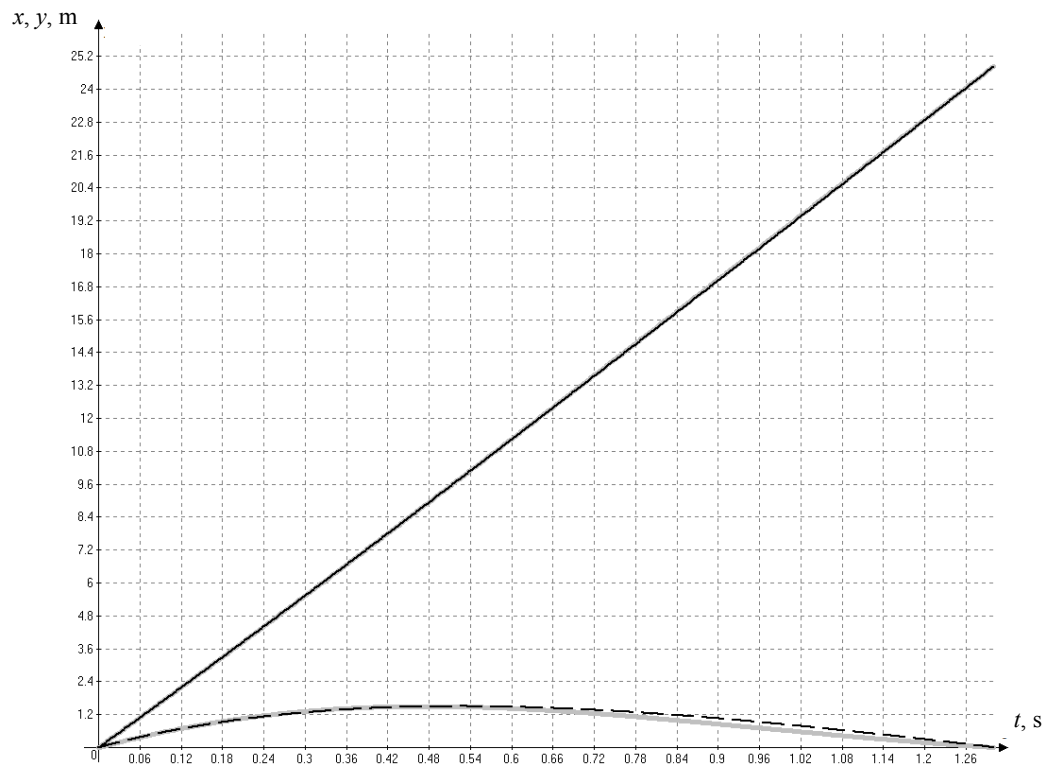


Fig. 5. Dependences of the deviations x , m, and y , m, on time t , s, calculated by the methods of quadratic harmonic approximation along the x -axis — black solid line; along the y -axis: dotted line — by the method of quadratic approximation, gray line — by the harmonic approximation method [13]

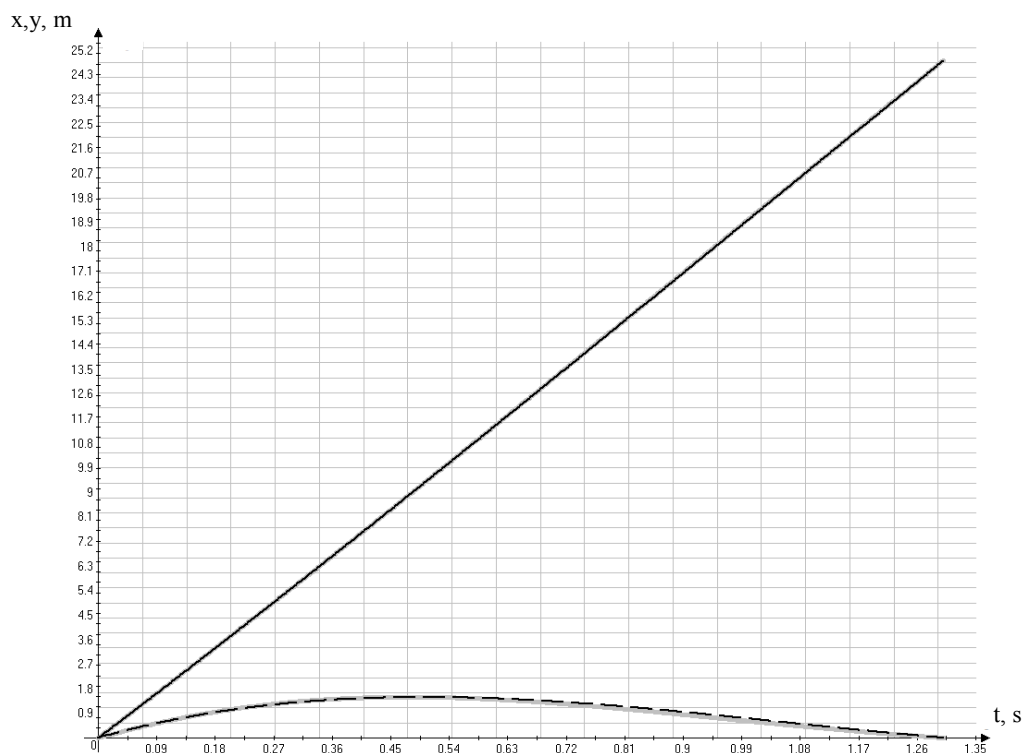


Fig. 6. Dependences of the deviations x , m, and y , m, on time t , s, calculated by the methods of cubic and harmonic approximation along the x -axis — black solid line; along the y -axis: dotted line — by the method of cubic approximation, gray line — by the harmonic approximation method [13]

As can be seen from the above calculated data, the divergence of analytical methods does not exceed 20 %. The same calculations were carried out for car GAZ-3102 [12].

Construction of a finite element model of the contact of the cable barrier and bus Mercedes-Benz-0345.

To analyze the performance of the approximate method of constructing the MV trajectory, a FE-model of the interaction of the cable barrier and bus Mercedes-Benz-0345 was developed in accordance with the industry standard STO 521000-005-10690827-2015¹, agreed with Rosavtodor in 2017. According to this standard, the installation of cable barriers for tests was carried out; the test results were also used in the analytical modeling of the trajectories and deviations of the MV. The object of virtual tests were cable barriers of 14DD/U 4(300)-P-1, 1-3, 0-GB brand [11, 13] with the following parameters:

- octagonal sleeves of GZ 500/U brand;

- STD-2 racks consist of two elements in the form of a square pipe with a length of 1500 m with a cross-section size of 50=50=3 mm;

- spacing of racks with concreted sleeves at the working area — 3 m;

- spacing in the initial and final sections — 2 m;

- the height of the racks above the road surface — 1.1 m.

Cable parameters:

- three-strand, seven-conductor;

- diameter — 19 mm;

- rated breaking force ≈ 173 kN;

- the number of branches — 4.

Bus Mercedes-Benz-0345 parameters [12, 13]:

- gross mass — 14,050 kg;

- overall length — 12,000 mm;

- overall width — 2,500 mm.


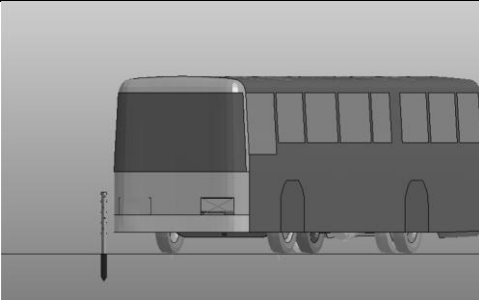

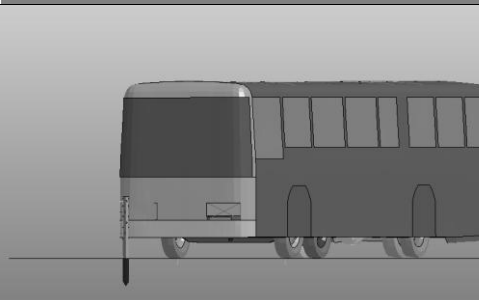

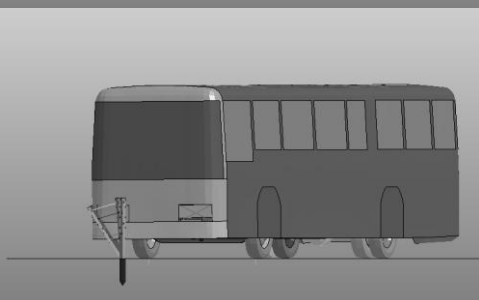

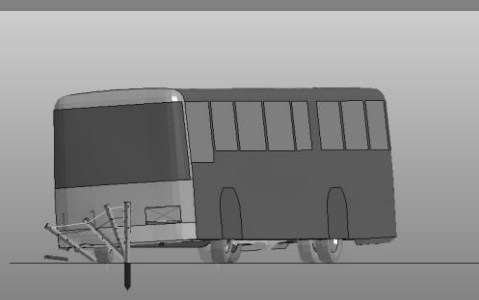

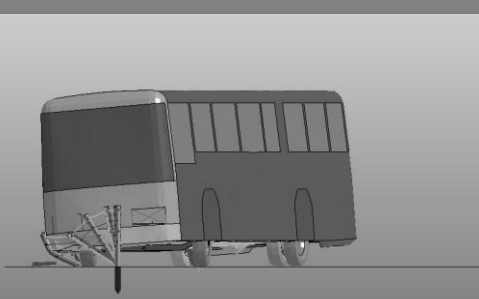
The speed of the MV coming into contact with the barrier is 69 km/h. The angle between the plane of the barrier and the direction of the MV movement — 20° in accordance with the methodology of GOST R 52721-2007

¹STO 521000-005-10690827—2015. Retaining side barriers for vehicles with the use of a C-section of a beam. “PIK” Enterprise. [rosavtodor.gov.ru](https://rosavtodor.gov.ru/storage/app/media/rosavtodor/b/2016/02/09/sto_521000_005_10690827_2015.pdf) URL: https://rosavtodor.gov.ru/storage/app/media/rosavtodor/b/2016/02/09/sto_521000_005_10690827_2015.pdf (accessed: 10.01.2021). (In Russ.)


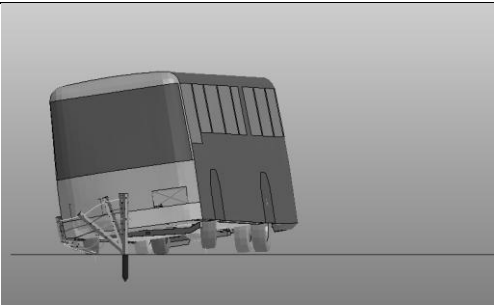

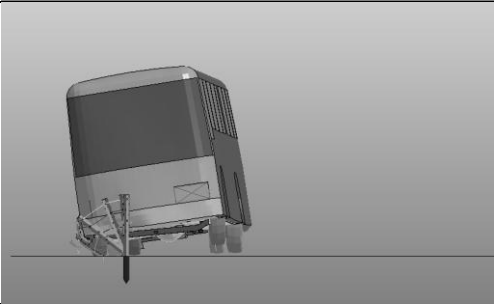

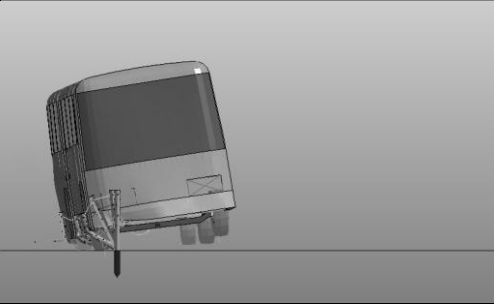
(nos. 6.1–6.6) [11, 13]. Time-lapse images of the MV according to the data of full-scale¹ and virtual tests are presented in the Table 1.

Table 1

Comparative frame-by-frame images of MV

Timepoint t , s	Test mode	
	full-scale	virtual
0.00		
0.16		
0.32		
0.48		
0.64		

¹STO 10690827-001—2015. Lateral deformable road barriers, cable type. Specifications. “PIK” Enterprise. rosavtodor.ru/www/rosavtodor.ru URL: <http://rosavtodor.ru/www/rosavtodor.ru/storage/app/media/uploaded-files/sto-10690827-001-2015.pdf> (accessed: 08.01.2021). (In Russ.)

Timepoint t , s	Test mode	
	full-scale	virtual
0.80		
0.96		
1.12		

The field test results practically coincided with the results of the virtual tests, since in both cases, the dynamic deflection of the barrier was 1.5 m; the path length of the interaction of the MV and the barrier from the calculation was 23.5 m, according to the field tests — 25 m. The relative error of the path length of the interaction did not exceed 6 %.

Research Results. As a result of a virtual test using the developed FE-model of the cable barrier, the trajectories of the characteristic points of bus Mercedes-Benz-0345 were determined. Fig. 7 shows the points of the MV for which the readings were taken, point C corresponds to the center of gravity.

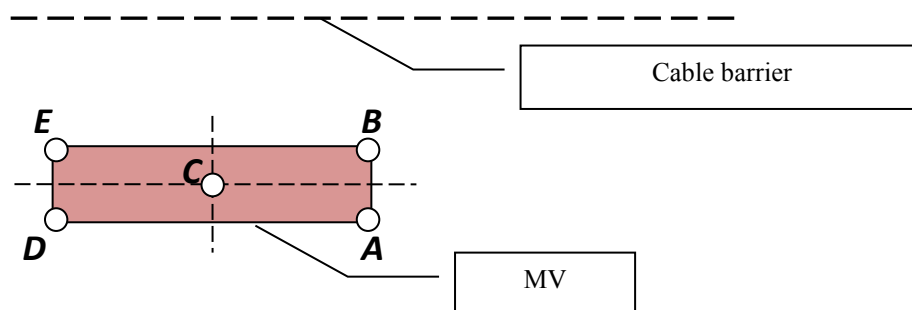


Fig. 7. MV points selected for analysis: A , B — on the frontal surface; D , E — on the rear surface

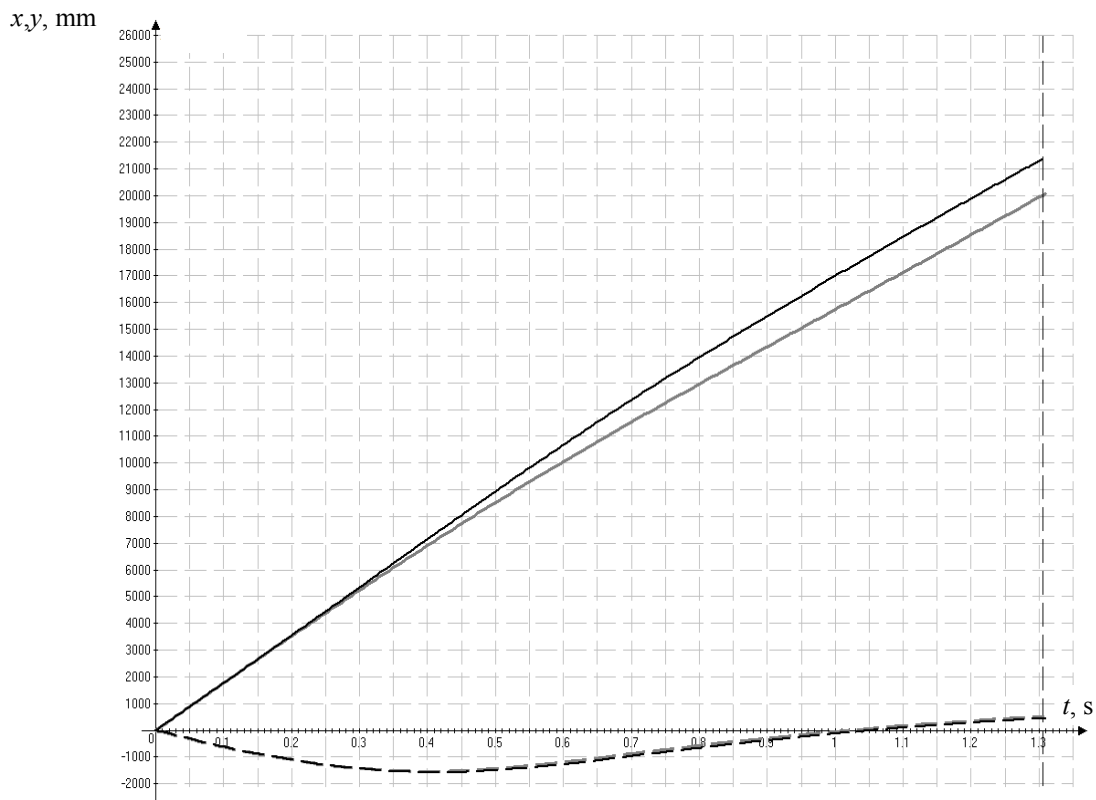


Fig. 8. Dependence of displacements of the MV characteristic points on time.
Dotted line — for points *A* and *B* along the *y*-axis; solid lines — along the *x*-axis:
black — for point *A*, gray — for point *B*

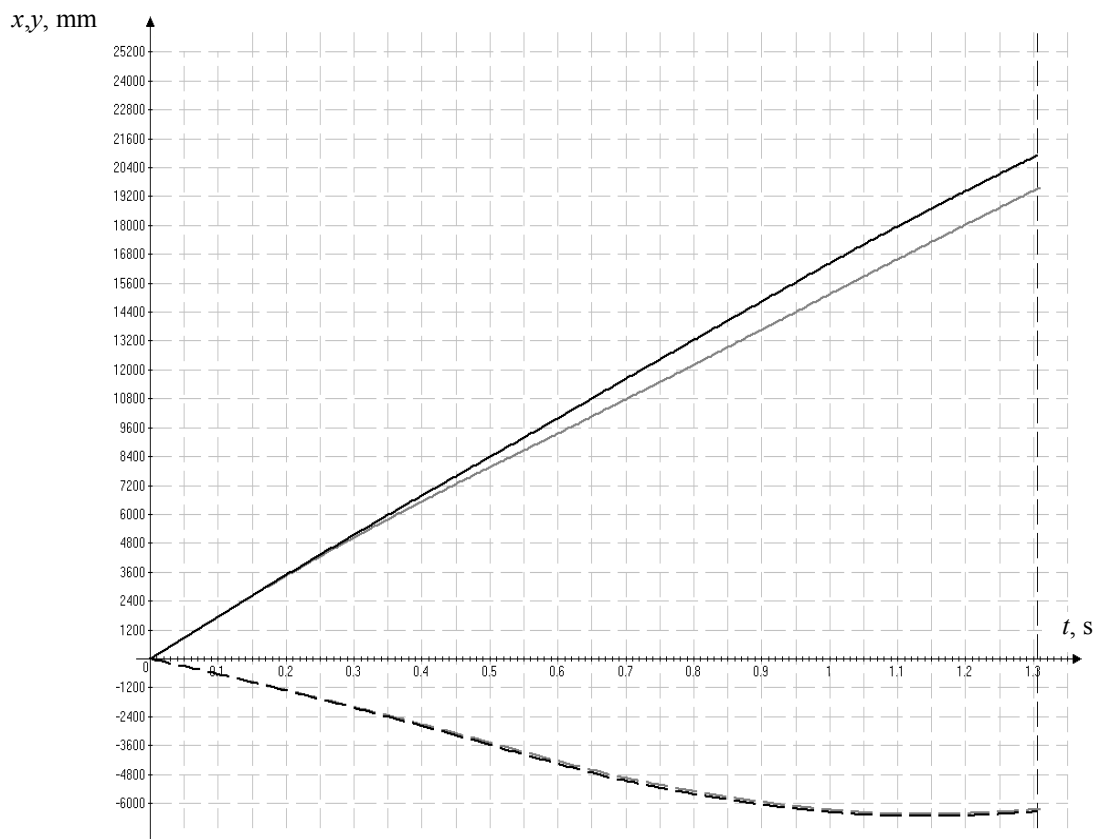


Fig. 9. Dependence of displacements of the MV characteristic points on time.
Dotted line — for points *D* and *E* along the *y*-axis; solid lines — along the *x*-axis:
black — for point *D*, gray — for point *E*

As can be seen from the presented data, the displacements of points *A*, *B*, and *D*, *E* along the *y*-axis match in pairs. The same can be observed for speeds. Thus, in case of oblique collision of the MV with the side cable barriers, the movement of the MV is really close to translational.

Discussion and Conclusions. The analysis of the kinematic results of the virtual test in comparison with the kinematic analytical calculations shows that the representation of the MV as a material point in case of its oblique collision with the side cable barriers is justified, since the movement of the MV is close to the translational one. However, if necessary, for a more accurate analytical calculation of the kinematic characteristics of the motion of points located in areas close to the points *C*, *D*, *E*, an additional analytical calculation is required, for example, using the equations of plane-parallel motion of a solid body.

References

1. McClanahan D, Albin RB, Milton JC. Washington State Cable Median Barrier In-Service Study. In: Presentation at the 83-rd Annual Meeting of the National Transportation Research Board, Washington D.C.; 2004. Available from: <http://www.wsdot.wa.gov/publications/fulltext/Policy/CableBarriersubmittalforTRB.pdf> (accessed: 02.11.2020).
2. Amato G, Ghosh B, O'Brien F, et al. A scaling method for modeling the crashworthiness of novel roadside barrier designs. *International Journal of Crashworthiness*. 2013;18(3):317. Available from: <https://www.tandfonline.com/doi/full/10.1080/13588265.2013.783429>. (accessed: 23.11.2020).
3. Tuan ChY, Sarmah RD, Tuan AY, et al. Progressive failure simulation of security cable barriers. *International Journal of Nonlinear Sciences and Numerical Simulation*. 2010;11(9):755–775.
4. Hunter WW, Stewart JR, Eccles KA, et al. Three-Strand Cable Median Barrier in North Carolina. *Transportation Research Record: Journal of the Transportation Research Board*. 2001;1743(1):97–103.
5. Karpov IA. Razrabotka konechno-ehlementnykh modelei trosovykh dorozhnykh ograzhdenii s ispol'zovaniem programmnoy kompleksa LS-DYNA [Development of finite element models rope guardrails using the software package LS-DYNA]. *Avtomobil'. Doroga. Infrastruktura*. 2014;2(2):38. Available from: URL: https://www.adi-madi.ru/madi/article/view/91/pdf_36 (accessed: 08.01.2021). (In Russ.)
6. Kolesnikova GP, Gasainiev AR. Priblizhennoe matematicheskoe modelirovanie traektorii dvizheniya ATS pri kosom naезде na bokovye trosovye ograzhdeniya [Approximate mathematical modeling of the trajectory of the ATS at an oblique hitting the side of a cable fence]. *Avtomobil'. Doroga. Infrastruktura*. 2018;1(15):2. Available from: URL: <https://www.adi-madi.ru/madi/article/view/515> (accessed: 08.01.2021). (In Russ.)
7. Rainus GE. Raschet mnogoproletnykh trosov i mnogoproletnykh ferm iz trosov [Calculation of multispan cables and multispan cable trusses]. Leningrad: Stroizdat; 1968. 135 p. (In Russ.)
8. Demyanushko IV, Obshchev AG. Raschetno-eksperimental'nyi analiz trosovykh dorozhnykh ograzhdenii bezopasnosti [Computational and experimental analysis of cable road safety fences]. In: Collection of papers on Questions of construction mechanics and reliability of machines and structures. Moscow: MADI Publ. House; 2012. P. 34–44. (In Russ.)
9. Bateman MB, Howard IC, Johnson AR, et al. Validation of a computer simulation of the impact performance of a wire rope safety fence. In: Proceedings of the Institution of Mechanical Engineers, Part C: Journal of Mechanical Engineering Science. 2007;221(12):1557–1570.
10. Drong BI, Dubinin VV, Ilyin MM, et al. Kurs teoreticheskoi mekhaniki [Course of theoretical mechanics], 5th rev. ed. Moscow: Bauman University Publ. House; 2017. 580 p. (In Russ.)
11. Kolesnikova GP. Analiticheskii raschet kinematicheskikh kharakteristik avtomobil'nogo transportnogo sredstva pri kosom naезде na bokovye trosovye ograzhdeniya s uchetom udara [Analytical calculation of the kinematic characteristics of an automobile vehicle with oblique collision with side cable barrier with impact taken into account]. *Avtomobil'. Doroga. Infrastruktura*. 2019;4(22):1. Available from: URL: https://www.adi-madi.ru/madi/article/view/833/pdf_480 (accessed: 08.01.2021). (In Russ.)
12. Olson RM, Post ER, McFarland WF. Tentative service requirements for bridge rail systems. Highway research board. National academy of Sciences – National research council. 1970. Available from:

http://onlinepubs.trb.org/Onlinepubs/nchrp/nchrp_rpt_86.pdf. (accessed: 02.11.2020).

13. Kolesnikova GP. Priblizhennyye metody analiticheskogo modelirovaniya traektorii dvizheniya ATS pri kosom naezde na bokovye trosovye ograzhdeniya [Approximate methods of analytical modeling of the trajectory of motor vehicle movement at an oblique hitting the side of a cable barrier]. Avtomobil'. Doroga. Infrastruktura. 2018;(16):3. Available from: URL: https://www.adi-madi.ru/madi/article/view/568/pdf_354 (accessed: 08.01.2021). (In Russ.)

Submitted 02.11.2020

Scheduled in the issue 25.01.2021

About the Author:

Kolesnikova, Galina P., lecturer of the Mechanics Department, Peter the Great Strategic Missile Troops Academy (8, Karbysheva St., Balashikha, 143900, RF), ResearcherID: [D-9839-2018](https://orcid.org/0000-0003-3392-9281), ORCID: <https://orcid.org/0000-0003-3392-9281>, kolesnikovagp@mail.ru

The author has read and approved the final manuscript.

MACHINE BUILDING AND MACHINE SCIENCE



UDC 519.216.2

<https://doi.org/10.23947/2687-1653-2021-21-1-43-54>

Inverse analysis method for mathematical modeling of hydrodynamic ballast in a drilling rig



I. R. Antypas¹, A. G. Dyachenko¹, B. I. Saed²

¹ Don State Technical University (Rostov-on-Don, Russian Federation)

² University of Aleppo (Aleppo, Syrian Arab Republic)

Introduction. When organizing drilling operations, one of the major problems is the accuracy and smoothness of lowering bundles of pipes into the shaft of the drilling rig. This depends on many factors, including the operation of the hydraulic brake of the lifting device. The objectives of this work are to create and study a mathematical model of hydrodynamic ballast in a drilling rig. Using the inverse analysis method, the effect of some performance indicators on the braking torque of the hydraulic brake is studied.

Materials and Methods. The experiments were performed using a laboratory setup, which is a model of a hydrobrake. Its valve was closed under various conditions to obtain several pressure values with the calculation of the braking torque when a certain weight was suspended. The real (field) operating conditions of the hydromatic brake were simulated, and the results obtained were compared. When creating a mathematical model, the inverse analysis method is used. It is based on the results of experimental measurements and provides expressing the totality of the effects of individual variables on the braking torque.

Results. A mathematical model of the hydraulic brake has been created and tested. The dependence of the braking torque on the pressure, density, and viscosity of the ballast fluid is determined. The influence of each variable is determined experimentally since the dependence under consideration cannot be represented as a direct relationship. The inverse analysis method is used to obtain a set of constant values that give the optimal solution. Taking into account the standard error array and the minimum standard error, the statistical errors made during experimental measurements are considered. The physically acceptable range of values of the proposed mathematical model is visualized. Using a basic (nonlinear) mathematical model, the auxiliary braking torque of a hydrobrake is calculated as a function of pressure, density, and viscosity. The proposed model validity is established. The calculated values of the braking torque were used as a criterion of correctness. The erroneous discrepancy did not exceed 6 %. For additional testing of the model, a computational experiment simulating field conditions was performed.

Discussion and Conclusions. For mathematical modeling of hydrodynamic ballast in a drilling rig, it is advisable to use the inverse analysis method. The model proposed in this paper relates the braking torque of a hydrobrake to the operating parameters of the fluid inside the ballast: pressure, viscosity, and density. The objectivity of the model is validated. An amendment to it is proposed to simulate the operation of the brake in the field. Based on the results obtained, in future studies it is advisable to test the created model in the field with a real payload.

Keywords: hydromechanical ballast, mathematical modeling, inverse analysis method.

For citation: I.R. Antypas, A.G. Dyachenko, B.I. Saed. Inverse analysis method for mathematical modeling of hydrodynamic ballast in a drilling rig. Advanced Engineering Research. 2021, vol. 21, no. 1, p. 43–54. <https://doi.org/10.23947/2687-1653-2021-21-1-43-54>

© Antypas I. R., Dyachenko A. G., Saed B. I., 2021



Introduction. When setting up drilling rigs, the operations of lifting and lowering drill pipes are provided with lifting gears (coils). They are equipped with two types of brakes, the main of which is mechanical. During the drilling process, the weight of the pipes exceeds the payload. To compensate for it, an auxiliary control ballast designed to reduce the speed when installing a group of drill pipes is introduced [1–4].

Ballasts are used to control the load and speed of the hook, as well as to absorb the kinetic energy of a group of borehole drill pipes. In addition, ballasts:

- reduce the effort on the drilling rig, especially under heavy loads;
- reduce the wear of the main mechanical ballast elements;
- help to slowly and smoothly stop the load attached to the hook.

One of the types of auxiliary brakes is hydrodynamic. In this case, the water in the ballast converts part of the absorbed kinetic energy of the lifting axis into heat, and due to this, the pipes are lowered and raised [5–7].

When manipulating the pipes, the brake axis is connected to the axis of the lifting gears. During the operation, the moving part of the installation displaces water in the direction of the inclined blades inside the stator, and rotates at a speed equal to the rotation speed of the axis of the lifting gears. Water falls on the stator ribs, and then on its parts. The process is repeated, and the forces that hinder the movement of the rotor increase. This creates a braking torque that reflects the rotational movement of the lifting gear axes and reduces the rotary speed. As a result, speed of lowering the group of drill pipes decreases [8–10].

The braking safety factor (if its value does not exceed the permissible value) coordinates the auxiliary hydrodynamic work and the effects of the operation of two main brake systems, as well as provides a longer service time for the main brake elements. This is done through reducing the wear of the friction discs and the planes of the brake wheels. Increasing the braking torque of the ballast provides the correct braking movement of the cylindrical hoist. This demonstrates the importance of studying the hydrodynamic brake.

The hydraulic power of the brake N is determined from the ratio:

$$N = \rho \cdot g \cdot Q \cdot H, \quad (1)$$

where ρ — the density of the working fluid (fresh water); g — gravity acceleration; Q — the amount of working fluid consumed, equal to the volume of the working fluid, which passes through the system of ribs in one working cycle; H — the height (level) of the working fluid in the ballast.

The braking torque M_B of the forced engine braking is determined from the ratio:

$$M_B = \rho \cdot g \cdot Q \cdot H / \omega, \quad (2)$$

where ω — angular velocity of rotation of the moving section of the ballast.

Indicators of kinematic braking of ribbed hydraulic machines are determined from the known theoretical ratios of the braking torque:

$$M_B = \lambda_M \cdot \rho \cdot (D^5 - d^5) \cdot \omega^2, \quad (3)$$

$$M_B = \lambda_M \cdot \rho \cdot (D^5 - d^5) \cdot \frac{n^2}{100}. \quad (4)$$

Here, D — the outer diameter of the “ring” of the working fluid formed during the rotation of the rotor wheel and assumed to be equal to the diameter of the wheel of the moving section; d — the inner diameter of the working fluid ring, which depends on the level of the ballast; n — the number of revolutions of the moving section of the ballast (the number of rotating axes), rpm:

$$\left(\omega = \frac{2\pi n}{60} \Rightarrow \omega^2 = \frac{n^2}{100} \right).$$

The hydraulic braking torque coefficient λ_M is a dimensionless value that takes into account the shape of the working cavities in the ballast, the parameters, and the number of brake ribs. In practical calculations, the average value of the hydraulic braking torque coefficient is assumed to be 0.3.

The objective of the study is to investigate the effect of some performance indicators on the braking torque of the hydraulic brake, which is the pressure inside the brake chamber, as well as on the density and viscosity of the working fluid inside the ballast. These indicators are absent in the ratio (4); therefore, we assume that the brake operates at an atmospheric pressure of 1 atmosphere, the fluid is fresh water with a density of 1 g/cm³ and a viscosity of 1 stoke.

Materials and Methods. Laboratory experiments were conducted at the University of Aleppo (Syrian Arab Republic) on a device that is a model of hydrodynamic brake inhibition (Fig.1).

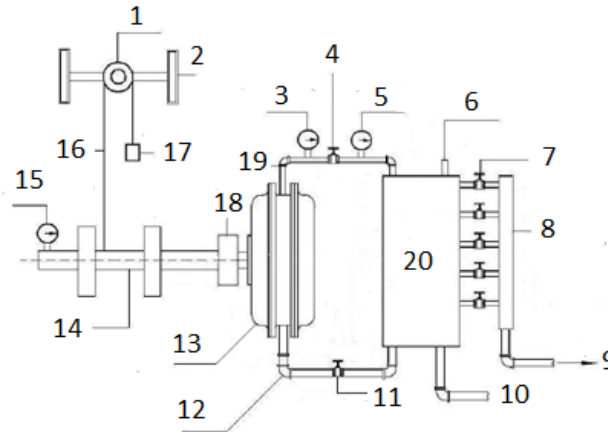


Fig. 1. Laboratory installation — hydrodynamic brake inhibition model:

- 1 — pulley, 2 — pulley armrest, 3 — pressure gauge, 4 — exhaust valve, 5 — thermometer, 6 — opening in the upper part of the tank, 7 — fluid level control valves, 8 — fluid outlet channel, 9 — fluid outlet from the tank, 10 — fluid drain valve, 11 — inlet valve, 12 — inlet line, 13 — hydraulic brake, 14 — coil, 15 — cycle number meter, 16 — cable, 17 — payload, 18 — communication hub, 19 — control line, 20 — fluid tank.

Stages of experiments

1. The tank and ballast are filled with fluid to the required level (0.106 m to the level of the first valve).
2. Using a hand lever connected to the coil, the weight suspended on the hook is raised by 0.317 m. It weighs 8 kg and is connected to the cable.
3. The bundle of pipes is allowed to fall under its own weight.
4. Readings from the indicator of the rotation of the axis of the coil are taken.
5. Then the impact of the indicators obtained during laboratory experiments on the study of hydraulic braking is recorded:

- the pressure created in the brake chamber (P);
- the density of the working fluid (ρ);
- the viscosity of the working fluid (μ).

First, the braking torque of the auxiliary hydrodynamic brake is calculated from the ratio (4). For this purpose, the values n , D , d are determined.

The outer diameter of the “ring” of the working fluid D is formed when the wheel of the moving section (rotor) rotates and is assumed to be equal to its diameter. The diameter D of the propulsor of the laboratory unit in the practical experiments is 0.33 m.

The inner diameter of the working fluid ring d depends on the level of the ballast. To determine this diameter, the following volumes are aligned:

- working fluid inside the ballast;
- the fluid in the “ring”, which is formed when the movable section rotates inside the ballast and is limited by the height of the coolant in the tank (0.106 m).

At $D = 0.33$ m, the working volume of the ballast fluid is 2.85 liters. The calculations have shown that the inner diameter $d = 0.283$ m.

The number of revolutions n is associated with the suspended load. If the brake does not work, this is the number of revolutions of the coiler. If it is separated from the brake, then n is taken from the laboratory experiments: with a load weight of 8 kg, $n = 240$ rpm.

We calculate the hydraulic braking moment for the weight of 8 kg attached to the hook. During the experiment, the tank was filled with fresh water to the level of the first valve (0.106 m) at the following parameters: pressure $P = 1$ atm, fluid density $\rho = 1$ g/cm³, and fluid viscosity $\mu = 1$ St. Therefore, the moment of hydraulic braking:

$$M_B = 0.3 \cdot 1000 \cdot (0.33^5 - 0.283^5) \cdot \frac{240^2}{100} = 355 \text{ H} \cdot \text{m}.$$

Consider the inverse relationship to (2). First of all, we are talking about the inverse relationship between the torque and the angular velocity (ω). A decrease in the number of revolutions n by 20% with an increase in the fluid density means an increase in the torque by 20%. Consider the permissible value of the braking torque 355 N·m. As a result, we get the desired value of the braking torque at the following parameters: pressure $P = 1$ atm, density $\rho = 1$ g/cm³, and fluid viscosity $\mu = 1$ St.

With regard to this work, we note the following. When determining the braking torque of a hydraulic brake, it is required to consider the number of revolutions of the coil connected to the brake axis (i.e., during braking): a decrease in the winding speed by a certain percentage means the same increase in torque.

The effect of the pressure inside the ballast on the braking torque of the hydraulic brake. Fluid pressure was created inside the hydraulic brake by closing the valve in the fluid outlet line. We conducted a laboratory experiment and calculated the braking torque with a suspended load weighing 8 kg. The results are shown in Table 1.

Table 1

Change in the braking torque of the hydraulic brake when the pressure inside the ballast changes

Pressure inside the ballast, atm	1	1.25	1.4	1.55	1.7	1.85
Left torque limit, N·m	105	104	103	100	95	90
Right torque limit, N·m	355	359	363	372	388	405

Fig. 2 shows the change in the braking torque when the pressure inside the ballast changes.

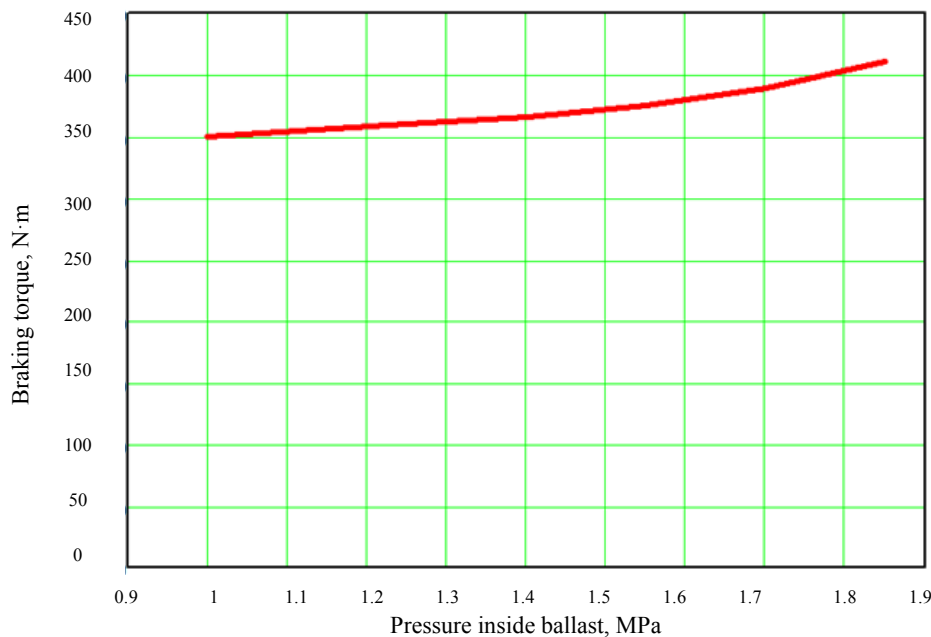


Fig. 2. Change in the braking torque at different pressures inside the ballast

The effect of the working fluid density on the braking torque. The experiments used chemicals that increase the density of water without corroding the elements of laboratory equipment.

Various concentrations of substances dissolved in water for the production of a ballast fluid of different densities are considered. The conditions are the same: the braking torque is investigated with a suspended load of 8 kg (Table 2).

Table 2

Dependence of the braking torque on the fluid density, the number of coil turns, and additives in the ballast fluid

Fluid density	1	1.065	1.09	1.11	1.13	1.15
Number of coil turns	105	104	102	99	95	91
Sodium chloride salts						
Braking torque	355	359	366	375	388	402
Food sugar						
Braking torque	355	359	363	368	378	388

A very weak change in the viscosity with an increase in the concentration of the sodium chloride salt was observed. We can assume that the viscosity of the fluid is approximately equal to 1 St.

Fig. 2 shows the dependence of the braking torque on the density of the working fluid when using sodium chloride salt and food sugar.

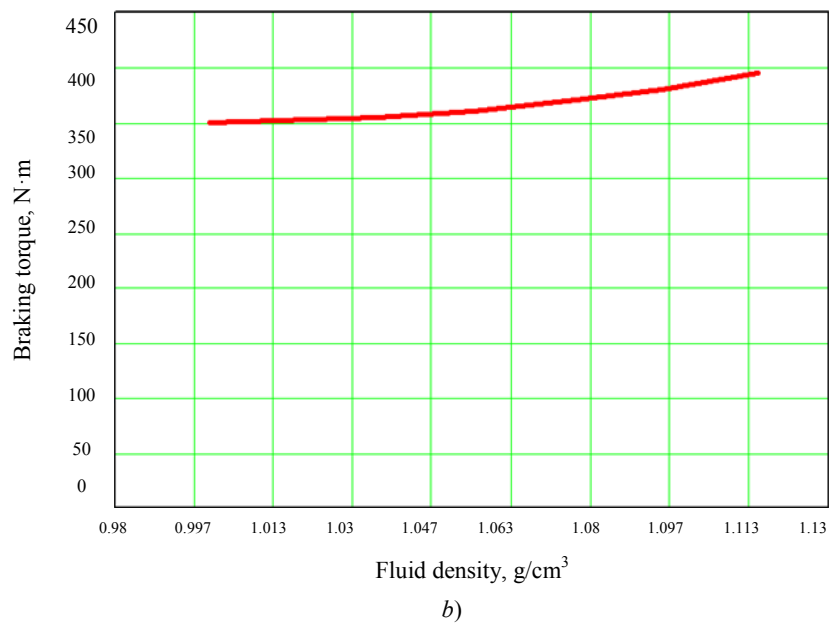
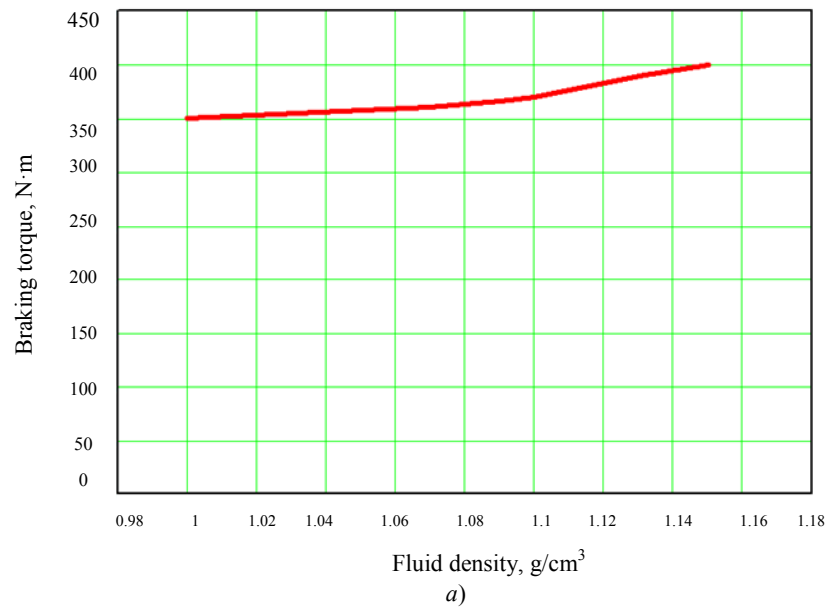


Fig. 3. Dependence of the braking torque on the density of the working fluid with the introduction of sodium chloride salt (a) and food sugar (b)

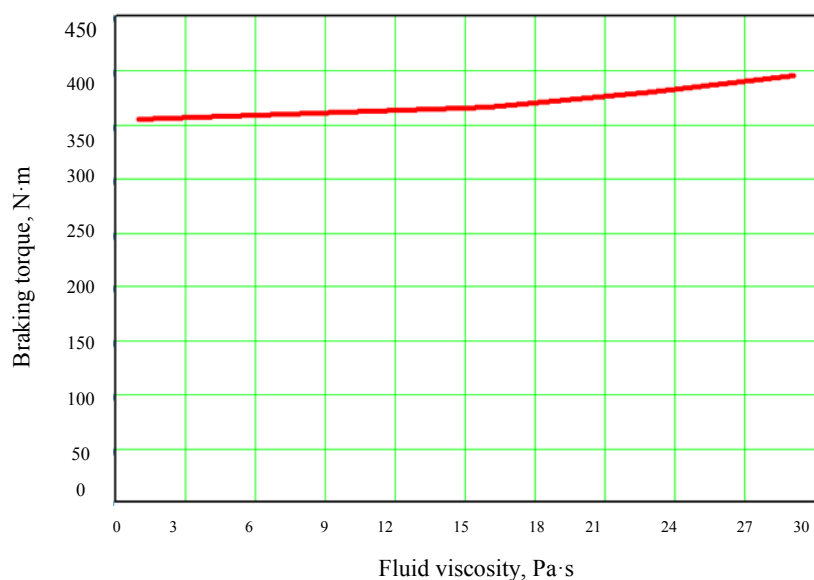
The effect of the working fluid viscosity on the hydraulic system braking. Various combinations of concentrations of glycerin and sodium silicate dissolved in water were used to produce ballast fluids that differ in viscosity. The conditions are the same: the braking torque is investigated with a suspended load of 8 kg (Table 3).

Table 3

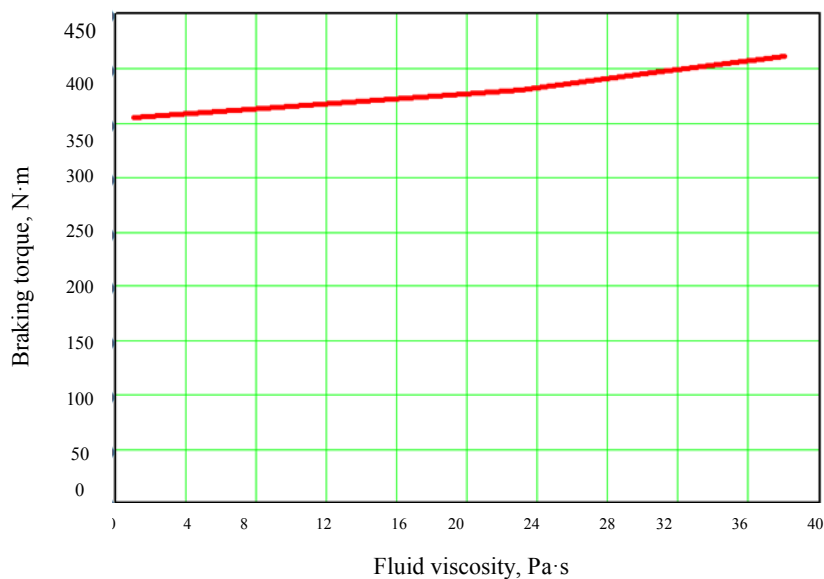
Dependence of the braking torque on the viscosity of the fluid and additives
in the ballast fluid

Fluid density	1	16	22	29
Number of coil turns	105	102	98	94
Glycerin				
Braking torque	355	365	378	392
Sodium silicate				
Braking torque	355	372	388	408

Fig. 4 shows the changes in the braking torque with the change in the viscosity of the working fluid when using glycerin and sodium silicate.



a)



b)

Fig. 4. Dependence of the braking torque on the viscosity of the working fluid inside the ballast with the introduction of glycerin (a) and sodium silicate (b)

The almost linear dependence obtained in this way should be checked using a mathematical model.

During the study of the viscosity index, it was found that the density and viscosity parameters do not depend much on each other, and the density is not equal to 1 g/cm³ (Table 4).

Table 4

Fluid density and viscosity ratio

Fluid viscosity	16	22	29	23	30	38
Density	1.008	1.014	1.021	1.017	1.025	1.034

The density influence coefficient did not exceed 6 %. It was calculated as the difference between the densities of a viscous fluid and fresh water. For example, if the viscosity was 30 St, the density was 1.025 g/cm³. Hence, the density impact factor:

$$\Delta = \frac{1.025 - 1}{1} \cdot 100 = 2.5\%.$$

Research Results

Creating a mathematical model of a hydraulic brake. The dependence of the braking torque on pressure, density, and viscosity cannot be represented as a direct relationship. The effect of each variable on the braking torque is determined experimentally (see Fig. 2–4).

The inverse analysis method. In the scientific and reference literature, there are no recorded indicators of the relationship of the braking torque and pressure, density, and viscosity. Therefore, the inverse analysis method was used [4]. It is efficient for creating mathematical models based on experimental measurements. It can be used to show how the combination of the above variables affects the braking torque. This can be expressed by the relation:

$$D = F(P, C), \quad (5)$$

where F — a function that relates the considered phenomenon D to a set of variable values and a set of values for constants of the mathematical model of the phenomenon.

The inverse analysis provides finding a set of values of the assumed constants of the model C through the inverse dependence:

$$P = F^{-1}(D_m, C), \quad (6)$$

where D_m — a set of experimental values for the phenomenon under study [4, 5].

It is assumed that a direct solution to the relation (6) is impossible. Therefore, an iterative system should be used to get a set of constant values that give an optimal solution. The generalization specifies a set of P values for the relations:

$$D_c = F(P, C), \quad (7)$$

$$|D_m - D_c| \leq \varepsilon, \quad (8)$$

where D_c — a set of calculated values for the phenomenon under study; ε — the required accuracy in accordance with the calculation of the phenomenon under study.

The proposed method takes into account the statistical errors made during the experimental measurements, focusing on the standard error array (S_i) and the minimum standard error. Thus, according to the statistical Gaussian distribution, the dependence of the density of statistical data:

$$f_1(P) = P_1 = \text{const.} \exp\left(-\frac{1}{2}[(D_c - D_m)' C_d^{-1} (D_c - D_m)]\right). \quad (9)$$

Here, C_d — standard error array. The symbol t stands for the matrix:

$$C_d = \begin{bmatrix} S_1^2(1) & \dots & 0 & \dots & 0 \\ 0 & \dots & S_1^2(2) & \dots & 0 \\ 0 & \dots & 0 & \dots & S_1^2(n) \end{bmatrix}, d, \quad (10)$$

where n — the number of control points.

D_c is a function of P , so, the problem is related to determining such a value of P , that D_c gives the maximum value P_t .

$$S_d = (D_c - D_m)^t \cdot C_d^{-1} (D_c - D_m). \quad (11)$$

The minimum value S_d can be obtained for more than one set of P values. Therefore, a correct set of parameters is formed using actual physical modeling of the value of these parameters (Fig. 5) [4, 5].

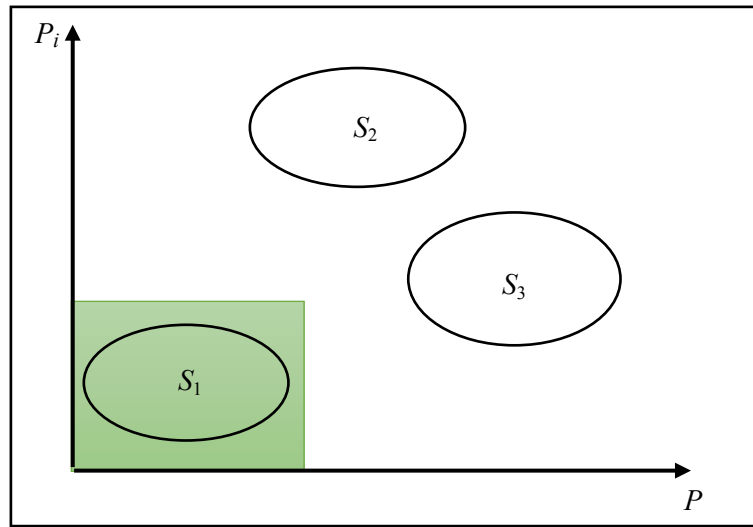


Fig. 5. Determining a physically acceptable range of values (green area):
 S_1 — physically acceptable mathematical solution, S_2, S_3 — mathematical solutions

Thus, we use a set of primary values for the parameters P_0 , which are derived from the average load of the physical field with account for the standard deviation matrix S_2 .

When using new Gaussian distribution, we obtain the following statistical intensity parameter:

$$f_2(P) = P_2 = \text{const} \cdot \exp\left(-\frac{1}{2}[(P - P_0)^t \cdot C_p^{-1} (P - P_0)]\right). \quad (12)$$

Here, C_p — standard deviation matrix:

$$C_p = \begin{bmatrix} S_2^2(1) & \dots & 0 & \dots & 0 \\ 0 & \dots & S_2^2(2) & \dots & 0 \\ 0 & \dots & 0 & \dots & S_2^2(r) \end{bmatrix}. \quad (13)$$

The problem expressed in the relation (6) is solved by inverse analysis. In this case, a set of values of P is within the limits indicated in (7) and (8). Hence, it is possible to determine a general region of the parameters P_1 and P_2 from the Gaussian distribution:

$$f(P) = P_1 \cdot P_2 = \text{const} \cdot \exp(-S), \quad (14)$$

$$S = \frac{1}{2}[(D_c - D_m)^t \cdot C_d^{-1} (D_c - D_m) + (P - P_0)^t \cdot C_p^{-1} (P - P_0)]. \quad (15)$$

So, for the solution, it is required to find the maximum or minimum values of S of the function $f(P)$.

The only way to find the minimum value of S is to use numerical methods, such as Gauss–Newton. This approach is based on the transformation of analytical relations into digital iterative ones with account for the error made due to ignoring some restrictions in the analytical relations (Fig. 6).

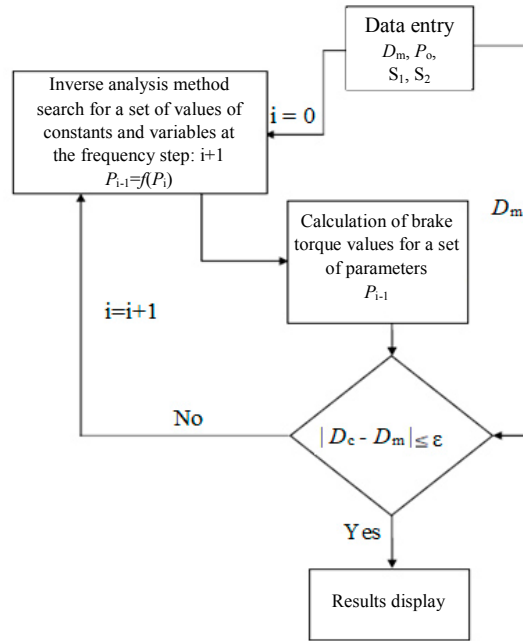


Fig. 6. Inverse analysis method algorithm

At the next stage of the work, the auxiliary braking torque of the hydrodynamic brake was calculated using a basic (nonlinear) mathematical model. It depends on the pressure, density, and viscosity:

$$M_B = f(P, \rho, \mu) + C, \quad (16)$$

$$M_B = a \cdot p^{n_1} + b \cdot p^{n_2} + d \cdot \mu^{n_3} + C. \quad (17)$$

The mathematical model (17) is a general nonlinear model if the values n_1, n_2, n_3 are not equal to one. The set of constants to search are a, b, d , and n_1, n_2, n_3 .

After applying the digital iterative method with an accuracy of 0.001, the parameters presented in Table 5 are found.

Table 5

Parameter values of the proposed model

Parameters	n_1	n_2	n_3	a	b	d	C
Value	1	1	1	58.5	284.6	1.29	10.62

According to Table 5, the physical phenomenon under study can be represented as the linear model (n_1, n_2, n_3) = 1:

$$M_B = 58.5P + 284.6\rho + 1.29\mu + 10.62. \quad (18)$$

The mathematical model is based on the results of laboratory experiments and implies the homogenization of units of measurement in accordance with the value of constants.

Adequacy of the mathematical model. The first stage of determining the adequacy of the model is a braking test at:

- pressure $P = 1$ atm,
- fluid density $\rho = 1$ g/cm³,
- fluid viscosity $\mu = 1$ St.

In this case, the braking was equal to the initial braking torque $M_B = 355 \text{ N}\cdot\text{m}$. This is logical, given the experimental values.

The second stage: three laboratory experiments with an 8-kilogram weight suspended on a hook. They are briefly described below.

The first experiment. We took the maximum values of the variables and the braking torque, and then performed the calculation using a mathematical model based on the ratio (18). We determined the error rate through comparing the experimental and mathematical results.

The second experiment. We took random values of variables that are relatively far from the experimental values and from the calculated values for the braking torque (according to the mathematical model). We calculated the error rate through comparing the experimental and mathematical results.

The third experiment. We took random values for variables that are relatively far from the experimental values and from the calculated values for the braking torque (according to the mathematical model). We calculated the percentage of errors through comparing the experimental and mathematical results.

Table 6 shows the results of validating the adequacy of the mathematical model.

Table 6

Results of checking the model adequacy

No.	Pressure	Fluid viscosity	Fluid density	Braking torque (calculation)	Braking torque (mathematical model)	Errors, %
1	1.85	1.15	38	490	495	1
2	1.60	1.10	13	406	434	6
3	1.45	1.12	26	423	447	5

So, the result validates the model adequacy. First, the level of its fallibility is found to be acceptable. Secondly, the identified errors have a scientific explanation. The fact is that the density parameter does not depend on the viscosity, and this is taken into account in the model. But the experiments conducted earlier to confirm this point of view revealed a correlation between these indicators at the level of 6 % — and this is approximately equivalent to the percentage of errors made when using a mathematical model (in comparison with the calculated data).

To express the cumulative effect of the fluid density and viscosity on the hydraulic brake operation, you can enter the parameter $\mu \cdot \rho$ in the model. However, this is not necessary, given the relatively low error rate. Otherwise, the proposed model will become much more complicated.

Simulation of field conditions. The proposed mathematical model expresses a physical phenomenon identified and studied under the laboratory conditions at the initial braking torque 355 N·m.

In the field, ballasts are characterized by an initial braking torque value M_{B0} . It is proposed to introduce into the mathematical model a parameter that will not change its shape, but, presumably, will reflect the “field”:

$$M_B = 58.5P + 284.6\rho + 1.29\mu + 10.62 + (M_{B0} - M_{Bm}), \quad (19)$$

where M_B — the braking torque of the “field” ballast after applying the conditions (pressure, density, and viscosity); M_{B0} — the initial braking torque for the field ballast; M_{Bm} — the initial braking torque of the laboratory ballast, equal to 355 N·m.

This is the main hypothesis. It is substantiated as follows. The dimensions of the laboratory inhibitor are not chosen randomly, but so as to correspond to the actual smaller dimensions of the brakes produced by *Parmac L.L.C* (model 112–500)¹.

¹ Original HYDROMATIC® Brake 620 251-5000. Parmac L.L.C // www.parmacbrake.com.

Discussion and Conclusions

1. The mathematical model is created using the inverse analysis method, which relates the braking torque of the hydrodynamic brake to the operating parameters (pressure, viscosity, and density) of the fluid inside the ballast.
2. The experiments with various random values of variables validated the adequacy of the model. The values of the braking torque determined experimentally and using the created model were compared. The error rate did not exceed 6 % (Table 6).
3. An amendment to the model for simulating the operation of the hydrodynamic brake in the field is proposed.
4. Based on the results obtained, it is advisable to test the created model in the field with a real payload in future studies.

References

1. Abdoulaev GS, Ren K, Hielscher AH. Optical tomography as a PDE-constrained optimization problem. *Inverse Problems*. 2005;21(5):1507–1530. DOI: 10.1088/0266-5611/21/5/002
2. Agapiou S, Bardsley JM, Papaspiliopoulos O, et al. Analysis of the Gibbs sampler for hierarchical inverse problems. *SIAM/ASA Journal on Uncertainty Quantification*. 2013;2(1):511–544. DOI: 10.1137/130944229
3. Asher MJ, Croke BFW, Jakeman AJ, et al. A review of surrogate models and their application to groundwater modeling. *Water Resources Research*. 2015;51(8):5957–5973. <https://doi.org/10.1002/2015WR016967>
4. Clark MP, Kavetski D, Fenicia F. Pursuing the method of multiple working hypotheses for hydrological modeling. *Water Resources Research*. 2011;47(9):1–16. <https://doi.org/10.1029/2010WR009827>
5. Stefani F. FEM Applied to Hydrodynamic Bearing Design. *New Tribological Ways*. University Campus STeP Ri: InTech; 2011. P. 451–476. DOI: 10.5772/15525
6. Wang Y, Gao D, Fang J. Coupled Dynamic Analysis of Deepwater Drilling Riser under Combined Forcing and Parametric Excitation. *Journal of Natural Gas Science and Engineering*. 2015;27(3):1739–1747.
7. Mao L, Liu Q, Zhou S, et al. Deep Water Drilling Riser Mechanical Behavior Analysis Considering Actual Riser String Configuration. *Journal of Natural Gas Science and Engineering*. 2016;33:240–254.
8. Wang Y, Gao D, Fang J. Optimization Analysis of the Riser Top Tension Force in Deepwater Drilling: Aiming at the Minimum Variance of Lower Flexible Joint Deflection Angle. *Journal of Petroleum Science and Engineering*. 2016;146:149–157.
9. Chang Y, Chen G, Xu L, et al. Influential Factors for the Design of Ultra-Deepwater Drilling Risers. *Petroleum Exploration and Development*. 2009;36(4):523–528.
10. Gong W, Duan Q. An adaptive surrogate modeling-based sampling strategy for parameter optimization and distribution estimation (ASMO-PODE). *Environmental Modelling & Software*. 2017;95:61–75. <https://doi.org/10.1016/j.envsoft.2017.05.005>

Submitted 04.12.2020

Scheduled in the issue 21.01.2021

About the Authors:

Antypas, Imad Rizakalla, associate professor of the Machine Design Principles Department, Don State Technical University (1, Gagarin sq., Rostov-on-Don, 344003, RF), Cand.Sci. (Eng.), associate professor, ResearcherID: [O-4789-2018](https://orcid.org/0000-0002-8141-9529), ORCID: <http://orcid.org/0000-0002-8141-9529>, imad.antypas@mail.ru.

Dyachenko, Alexey G., associate professor of the Machine Design Principles Department, Don State Technical University (1, Gagarin sq., Rostov-on-Don, 344003, RF), Cand.Sci. (Eng.), ORCID: <http://orcid.org/0000-0001-9934-4193>, alexey-a2@mail.ru.

Saed Bakir Imad, associate professor of the Agricultural Engineering Department, University of Aleppo (Mouhafaza, Aleppo, Syrian Arab Republic), Dr.Sci. (Eng.), associate professor, ORCID: <https://orcid.org/0000-0003-3855-7691>, bakir-111@mail.ru.

Claimed contributorship

I. R. Antipas: academic advising; statement of the problem; determination of the research methodology; collection and analysis of the analytical and practical materials on the research topic; critical analysis and finalization of the solution; computer implementation of the problem solution. B. I. Saed: statement of the problem; determination of the research methodology; collection and analysis of the analytical and practical materials on the research topic. A. G. Dyachenko: analysis of the scientific sources on the research topic; critical analysis and revision of the text.

All authors have read and approved the final manuscript.

MACHINE BUILDING AND MACHINE SCIENCE



UDC 62-82

<https://doi.org/10.23947/2687-1653-2021-21-1-55-61>

Simulation of the hydraulic system of a device with self-adaptation for power and kinematic parameters on the working body

T. A. Khinikadze¹, A. T. Rybak¹, P. I. Popikov²¹Don State Technical University (Rostov-on-Don, Russian Federation)²Voronezh State University of Forestry and Technologies named after G. F. Morozov (Voronezh, Russian Federation)

Introduction. Currently, Russia has adopted a course towards the creation of intelligent machines and equipment. The same holds for mobile technological machines for road construction and public utilities. Therefore, the design and creation of this type of actuators with a self-adaptation function is a critical task.

Materials and Methods. A device equipped with a hydraulic drive with self-adaptation to load and coordination of kinematic and power parameters of the principal motion and the feed movement of the working body of the rock-drilling rig, is presented. To study and design the device based on the mathematical modeling methods of a hydraulic drive and adaptive systems, a mathematical model is proposed. It is developed using the foundations of the theory of volumetric stiffness of hydraulic systems. This enables to accurately describe the impact of the dynamic properties of the hydraulic system (compressibility of the working fluid, elastic properties of pipelines, high-pressure hoses, hydraulic apparatuses) on the dynamic properties of the system as a whole.

Results. The mathematical model for a device with self-adaptation includes submodels of adaptive communication, interrelations of power, kinematic and process parameters of rock drilling, as well as mathematical description of the movement of system elements. The solution to the developed mathematical model was performed in the software environment for dynamic modeling of technical systems SimInTech. As a result, general dependences of the adaptive system on the design parameters of the system and the operating conditions are obtained.

Discussion and Conclusion. The mathematical model of the presented device shows the fundamental possibility of implementing the principle of self-adaptation in terms of load under external and internal disturbing actions during operation. The results obtained can be used under designing adaptive systems of other technological equipment, for example, for the implementation of deep drilling in workpieces with variable properties in its depth.

Keywords: hydraulic device with self-adaptation, hydraulic drive function, generalized mathematical model, adaptive communication, coordinated movements, working body, load, stabilization.

For citation: T. A. Khinikadze, A. T. Rybak, P. I. Popikov. Simulation of the hydraulic system of a device with self-adaptation for power and kinematic parameters on the working body. Advanced Engineering Research, 2021, vol. 21, no. 1, p. 55–61. <https://doi.org/10.23947/2687-1653-2021-21-1-55-61>

© Khinikadze T. A., Rybak A. T., Popikov P. I., 2021



Introduction. The course adopted in Russia on building intelligent machines is the basis for the design and creation of actuators with a self-adapting function. The solution to this problem is timely and relevant.

Drives with differential couplings of internal structure elements possess self-adapting properties [1]. This class of technical systems includes a variable rock drilling device (RF Patent No. 2582691). The self-adapting property is implemented by a device with negative feedback and positive feedback [2].

The quality of the self-adapting process is affected by external and internal actions — load variability, medium resistance, dry and viscous friction, volumetric stiffness of the fluid and pipelines, adaptive links.

Materials and Methods. At the current level of development of computer technology, the complexity and high cost of the designed equipment, methods of mathematical modeling are widely used at the development stage [3-

13]. The development of a special model for calculations and computational experiments to determine the parameters at the design stage provides a reasonable choice of the standard size of the device with self-adaptation.

Fig. 1 shows a device for exercising the function of self-adaptation under the conditions of force resistance on the working body which contains fixed displacement pump (H), security valve (KП), filter (Φ), adjustable throttles (Δp_1) and (Δp_2), flow regulator (PP), feed hydraulic cylinder (ГЦ) and main drive hydraulic motor (ГМ), hydraulic valves (P1), (P2) and (P3), pressure gauges (M_{H1}), (M_{H2}) and (M_{H3}),

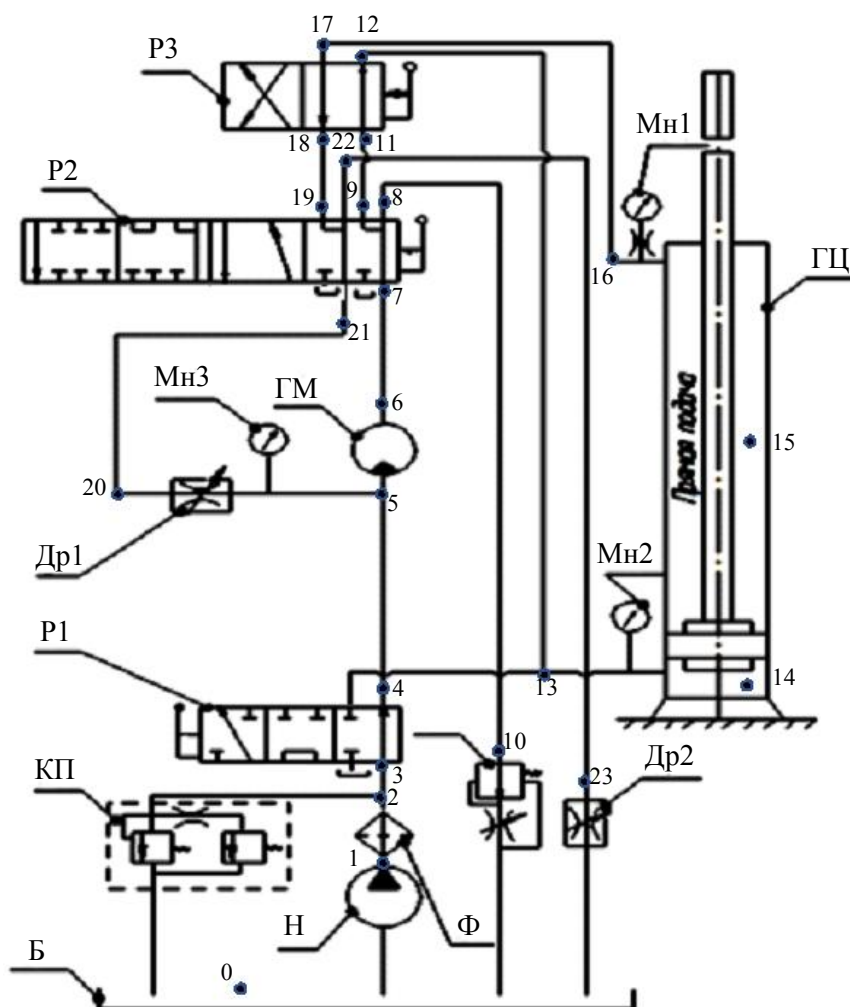


Fig. 1. Schematic diagram of the device for exercising the function of self-adaptation under the conditions of force resistance on the working body

The device is designed to exercise the function of self-adaptive load (to stabilize it) and matching output movements working on production machines and equipment, as well as functions of the actuator itself. Therefore, the device provides multi-position distributors for the formation of flows and directions of the working fluid. Such additional device functions include heating of the hydraulic oil in its start operation; “weighting” of moving parts (idle load) of the feeder when adjusting to technological mode; accelerated lifting (retraction) of the tool with rotation, but without controlling its speeds; tool feed “to the object of action” or “from the object of action” with rotation and control of tool speeds.

The mathematical dependence for the internal negative coupling of the device is established through joint solving the equations arising from the pressure balance equations in the system and the working fluid flow balance equation in the feedback system.

From the pressure balance in the system, it follows

$$\Delta p_{\Delta p5} = \frac{1}{\omega_{\Gamma M}} M_{\Gamma M} + \frac{1}{f_{\Pi}} F_{\Pi} - \left(1 - \frac{f_{\Pi, \text{шТ}}}{f_{\Pi}}\right) \Delta p_{\Delta p10}, \quad (1)$$

where $\Delta p_{\Delta p5}$ and $\Delta p_{\Delta p10}$ — differential pressure across throttles 5 and 10; $\omega_{\Gamma M}$ and $M_{\Gamma M}$ — reduced volume of the hydraulic motor ΓM and the torque generated by it; f_{Π} and $f_{\Pi, \text{шТ}}$ — areas of the hydraulic cylinder piston in the piston and rod cavities; F_{Π} — resistance force from the ground, overcome when moving the rod of the hydraulic cylinder $\Gamma \Pi$.

The balance equation for the costs in the feedback loop has the form

$$Q_{\Delta p10} = Q_{\Delta p5} + v_{\Pi} \cdot f_{\Pi, \text{шТ}}, \quad (2)$$

where $Q_{\Delta p5}$ and $Q_{\Delta p10}$ — the flow rate of the working fluid through the throttles $\Delta p1$ and $\Delta p2$; v_{Π} — the hydraulic cylinder $\Gamma \Pi$ piston travel speed.

Considering that the hydraulic pump H, which feeds the system, has a constant capacity, the flow of the working fluid through the flow regulator PP under the operation of the drive system remains constant. It becomes obvious that the flow rate of the working fluid through the throttle $\Delta p2$ will also be constant. In this case, the dependence of the acceleration of the hydraulic cylinder piston $\Gamma \Pi$ on the total load on the hydraulic motors of the main movement and the feed movement will take the form

$$\frac{dv_{\Pi}}{dt} = -A \left(\frac{1}{\omega_{\Gamma M}} \frac{dM_{\Gamma M}}{dt} + \frac{1}{f_{\Pi}} \frac{dF}{dt} \right), \quad (3)$$

where v_{Π} — hydraulic cylinder $\Gamma \Pi$ piston travel speed; t — time; A — feedback coefficient depending on the parameters of the nominal operating mode of the system, the design parameters of hydraulic machines, throttles and its settings.

It can be seen from the equation (3) that the positive increments of the torque on the hydraulic motor shaft and the movement of the hydraulic cylinder feed piston correspond to the negative increment of the tool feed speed. In other words, as the ground resistance increases to the rotation of the cutting tool or the movement of its feed, the tool feed rate decreases.

The direct relationship between the speeds and accelerations of the hydraulic motor shaft of the main movement and the hydraulic cylinder rod of the feed movement is as follows

$$v_{\Pi} = \frac{1}{f_{\Pi}} (\omega_{\Gamma M} \omega_{\Gamma M} - Q_{\text{pp}}),$$

or

$$\frac{dv_{\Pi}}{dt} = \omega_{\Gamma M} \frac{d\omega_{\Gamma M}}{dt}. \quad (4)$$

where $\omega_{\Gamma M}$ — the angular speed of rotation of the hydraulic motor shaft; Q_{pp} — the flow rate of the working fluid through the flow regulator.

From the equation (4), it can be seen that with an increase in the rotation speed of the hydraulic motor of the main movement (occurs with a decrease in resistance from the side of the treated surface), the speed of movement of the feed cylinder piston increases.

Mathematical modeling of the movements of the working elements of the device. The equations of motion of the rotor of the hydraulic motor of the main movement and the piston of the hydraulic cylinder of the tool feed have the form:

$$J_{\Gamma M} \frac{d\omega_{\Gamma M}}{dt} = \Delta p_{\Gamma M} \omega_{\Gamma M} - M_{\text{comp}}, \quad (5)$$

$$m_n \frac{dv_n}{dt} = f_n p_n - f_{n,шт} p_{n,шт} - F_{comp}, \quad (6)$$

where J_{TM} — the total moment of inertia of all rotating elements of the system reduced to the shaft of the hydraulic motor; m_n — the mass of all moving parts of the system reduced to the hydraulic cylinder piston; M_{comp} — the total moment of resistance to the rotation of the working body reduced to the shaft of the hydraulic motor; F_{comp} — total force of resistance to the tool movement from the side of the treated surface reduced to the piston of the hydraulic cylinder; Δp_{TM} — pressure drop across the hydraulic motor; p_n and $p_{n,шт}$ — pressure in the piston and in the rod cavities of the hydraulic cylinder, respectively.

Modeling the properties of a hydraulic system

The mathematical model of the hydraulic system of the device for performing the function of self-adaptation under the conditions of force resistance on the working body is developed using volumetric rigidity, which provides modeling as close as possible to the real characteristics [16–20]. When modeling, special attention is paid to determining the reduced coefficient of volumetric stiffness of high-pressure hoses [16]. The resulting mathematical model includes the following equations:

— the equation of the pressure increment at various points (in Fig. 1, marked by points 1 to 23) of the hydraulic system has the form:

$$dp = C_{npi} (\sum Q_{bxi} - \sum Q_{ncxi}) dt, \quad (7)$$

where $\sum Q_{bxi}$ and $\sum Q_{ncxi}$ — the sums of all the flow rates of the working fluid entering and outgoing from the considered (i -th) volume of the system during the time dt ; C_{npi} — the reduced coefficient of volumetric rigidity of the selected section of the hydraulic system;

— the equation for determining the flow rate of the working fluid through various elements of the hydraulic system has the form:

$$Q_i = \mu f \sqrt{\frac{2}{\rho} |p_i - p_{i+1}|} \cdot \text{sign}(p_i - p_{i+1}), \quad (8)$$

where p_i and p_{i+1} — pressure at the inlet and outlet of the hydraulic resistances; f — free cross-sectional area of resistance; ρ — working fluid density;

— the formula for calculating the reduced flow rate of linear resistances is as follows

$$\mu = \mu_l = \frac{1}{\sqrt{\lambda_l \frac{l_l}{d_l}}}, \quad (9)$$

where d_l and l_l — diameters and lengths of the linear section of the pipeline; λ_l — the coefficient of hydraulic friction of the pipeline;

— the formula for determining the reduced coefficient of volumetric stiffness of the metal sections of the pipeline has the form:

$$C_l = \frac{4}{\pi d^2 l} \frac{E_f l}{1 + \frac{d E_f l}{\delta E_l}}, \quad (10)$$

where d and l — the internal diameter and length of the pipeline section; δ — its wall thickness; E_f and E_l — moduli of elasticity of fluid and wall material of the hydraulic line.

The reduced coefficients of the volume stiffness $PБД$ are determined experimentally.

The performance of the hydraulic pump is determined with account for the volume losses from the formula:

$$Q_{HD} = \frac{q_{PH} \omega_H}{2\pi} \eta_{0,H}, \quad (11)$$

where q_{PH} — the working volume of the hydraulic pump; ω_H — the hydraulic pump shaft speed; $\eta_{0,H}$ — the current value of the volumetric efficiency of the hydraulic pump.

The flow rate of the working fluid through the hydraulic motor is determined from the formula:

$$Q_{\text{MOT}} = \frac{q_{\text{PM}} \omega_{\text{M}}}{2\pi \eta_{0,\text{M}}}, \quad (12)$$

where q_{PM} — the hydraulic pump working volume; ω_{M} — the hydraulic pump shaft speed; $\eta_{0,\text{M}}$ — current volumetric efficiency of the hydraulic motor.

The current value of the volumetric efficiency coefficients of the hydraulic pump and the hydraulic motor are determined from the formula:

$$\eta_0 = 1 - (1 - \eta_{0,\text{nom}}) \cdot \frac{p_{\text{p}}}{p_{\text{p,nom}}}, \quad (13)$$

where $\eta_{0,\text{nom}}$ — the nominal volumetric efficiency of the hydraulic pump and hydraulic motor; $p_{\text{p,nom}}$ — the value of the nominal pressure of hydraulic machines; p_{p} — the current value of the pressure on the pump or motor.

Research Results

The proposed mathematical model of the device under consideration provides high-precision theoretical studies on the operational capabilities of rock drilling at the design stage. The calculation of the drilling system, performed using the SimInTech software [10, 11], showed the correctness of this statement.

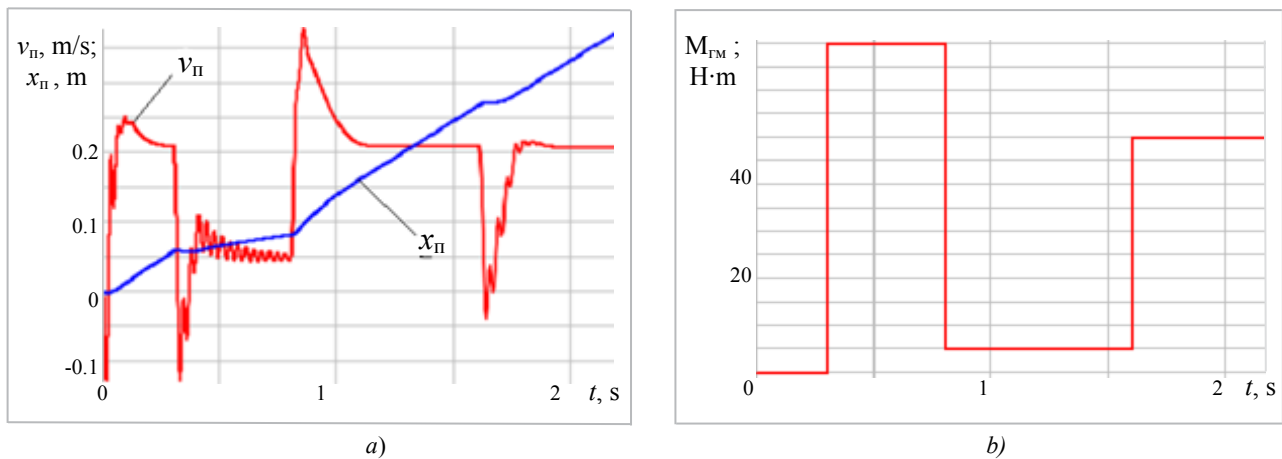


Fig. 2. Changing the parameters of the drilling machine operation with a stepwise change in the resistance to rotation of the main working body of the drilling machine from the ground: *a*) — movement of the hydraulic cylinder piston (x_{II}) and its speed (v_{II}); *b*) — torque of resistance to rotation of the hydraulic motor shaft $M_{ГМ}$

Fig. 2 shows the graphs of change in the parameters of the piston movement of the feed hydraulic cylinder with a stepwise change in the moment of resistance to rotation of the main working body of the drilling machine from the ground.

The analysis of calculation results presented in Fig. 2 shows that with an increase in the moment of resistance to rotation of the working body of the drilling machine (Fig. 2 *b*), the speed of translational movement of the tool decreases and can take negative values (Fig. 2 *a*). This indicates that the system performs the adaptation function. The properties of the system require additional research.

Conclusion. The proposed mathematical model enables to make a preliminary performance assessment at the design stage and select the most rational parameters of the drilling system equipped with an adaptive hydro-mechanical drive under different operating conditions and varying its design properties. The results obtained and their analysis suggest that the proposed method of adapting the main and auxiliary movements of the drive system can be successfully applied in other technological equipment, for example, in deep drilling of multilayer metal workpieces.

References

1. Ivanov KS, Yaroslavtseva EK. Teoriya mekhanizmov s dvumya stepenyami svobody [Theory of mechanisms with two degrees of freedom]. Lambert Academic Publishing; 2014. 180 p. (In Russ.)
2. Khinikadze TA. Issledovanie sootvetstviya kharakteristik adaptivnogo modulya gidroprivoda tekhnologicheskim parametram mashin [Study of characteristics conformity of the hydraulic drive adaptive module to technological parameters of the equipment]. Young Researcher of the Don. 2018;2(11):107–112. (In Russ.)
3. Popikov PI, Goncharov PE, Sharov AV. Matematicheskaya model' rabocheho protsessa lesnogo pozhnogo gruntometa s ehnergosberegayushchim gidroprivodom [Modelling workflow forest fire soil-thrower with energy-saving hydraulic drive]. Forestry Engineering Journal. 2017;4:182–189. (In Russ.)

4. Bartenev IM, Popikov PI, Sharov AV, et al. Osobennosti chislennogo integrirovaniya sistemy differentsial'nykh uravnenii rabocheho protsessa pochvoobrabatyvayushchei mashiny s gidroprivodom dlya profilaktiki i tusheniya lesnykh pozharov [Features of numerical integration of the system of different equations of the working process of soil-cultivating machine with a hydraulic drive for the prevention and suppression of forest fires]. *Forestry Engineering Journal*. 2018;3(31):170–176. (In Russ.)
5. Popikov PI, Scheblykin PN, Sharov AV, et al. Modelirovanie srabatyvaniya predokhranitel'nykh ustroystv lesnogo pozhnogo gruntometa [Modeling actuation safety devices forest fire soil - thrower]. *Aktual'nye napravleniya nauchnykh issledovaniy XXI veka: teoriya i praktika*. 2017;5(1):336–340. (In Russ.)
6. Sova AN, Stepanov MI, Sova VA, et al. Teoreticheskie osnovy modelirovaniya dinamicheskikh kharakteristik privodov perspektivnykh kosmicheskikh apparatov s uchetom funktsionirovaniya ostsillyatorov [Background for modeling the dynamic characteristics of advanced spacecraft drives considering the operation of oscillators]. *Vestnik of DSTU*. 2019;19(4):317–327. URL: <https://www.elibrary.ru/item.asp?id=41591369> (accessed: 27.01.2021). (In Russ.)
7. Syrkin VV, Kvasov IN, Galuza YuF, et al. Issledovanie dinamiki delitelya potoka s reguliruyushchim organom iz ehlastomera [Study of influence of fluid compressibility on dynamics of flow divider]. *Omsk Scientific Bulletin. Series “Aviation-Rocket and Power Engineering”*. 2018;22(4):9–14. (In Russ.)
8. Alekseev GV, Aksenova OI. Vozmozhnosti modelirovaniya oborudovaniya dlya snizheniya ehnergoemkosti realizuemykh tekhnologicheskikh protsessov [Equipment modeling to reduce technological processes power consumption]. *Journal of International Academy of Refrigeration*. 2015;4:49–54. (In Russ.)
9. Berdnik Y, Beskopylny A. The approximation method in the problem on a flow of viscous fluid around a thin plant. *Aircraft Engineering and Aerospace Technology*. 2019;91(6):807–813.
10. Beskopylny A, Kadomtseva E, Strelnikov G, et al. Model of heterogeneous reinforced fiber form concrete in bending. In: *IOP Conference Series on Materials Science and Engineering*. 2018;365(3):032023.
11. Beskopylny AN, Kadomtseva EE, Strelnikov GP. The boundary condition influence on a stress-strain state of a corrugated plate on an elastic foundation. *Materials Science Forum*. 2018;931:60–65.
12. Beskopylnyi AN, Lyapin AA. About the identification of layered constructions properties. *Recent Trends in Science and Technology Management*. 2016;2:36–45.
13. Chukarin AN, Beskopylny AN, Isaev AG. Issledovaniya vibroakusticheskikh kharakteristik v rabochei zone operatora pri abrazivnoi obrabotke svarnykh shvov [Research of vibroacoustic characteristics in the operator working area during welds abrasive treatment]. *Occupational Safety in Industry*. 2019;11:7–12. (In Russ.)
14. Kartashov BA, Kozlov OS, Shabaev EA. Dynamic mode environment of technical systems SimInTech: manual. Moscow: DMK-Press; 2017. 424 p.
15. Abalov AA, Nosachev SV, Zharov VP, et al. Using the SimInTech dynamic modeling environment to build and check the operation of automation systems. *MATEC Web of Conferences*. 2018;226:04003.
16. Rybak AT, Shishkarev MP, Demyanov AA, et al. Modeling and calculation of hydromechanical systems dynamics based on the volume rigidity theory. *MATEC Web of Conferences*. 2018;226:01001.
17. Rybak AT, Temirkanov AR, Lyakhnitskaya OV. Dynamics of Synchronous Hydromechanical Drive in Mobile Machine. *Russian Engineering Research*. 2018;38(9):702–704. DOI 10.3103/S1068798X18090253
18. Temirkanov AR, Rybak AT. Sinkhronnyi gidromekhanicheskii privod rabocheho organa mobil'noi mashiny i ego matematicheskaya model' [Synchronous hydromechanical drive of mobile actuator and its mathematical model]. *Vestnik of DSTU*. 2013;13(3-4):104–110. URL: <https://www.vestnik-donstu.ru/jour/article/view/400> (accessed: 27.01.2021). (In Russ.)
19. Temirkanov AR, Rybak AT. Modelirovanie sistemy gidromekhanicheskogo privoda rabocheho organa mobil'noi tekhnologicheskoi mashiny [Modeling of hydromechanical drive system of working body for mobile technology machine]. *Vestnik of DSTU*. 2014;14(4):176–185. URL: <https://www.vestnik-donstu.ru/jour/article/view/362> (accessed: 27.01.2021). (In Russ.)
20. Mirny VI. Nekotorye voprosy povysheniya proizvoditel'nosti gidravlicheskogo privoda perforatsionnogo pressa tsiklicheskogo deistviya [Several issues of productivity increase and economic effectiveness of hydraulic perforated hammer of cycling capacity]. *Vestnik of DSTU*. 2008;8(1):75–85. URL: <https://www.vestnik-donstu.ru/jour/article/view/1212> (accessed: 27.01.2021). (In Russ.)

Submitted 04.12.2020

Scheduled in the issue 21.01.2021

About the Authors:

Khinikadze, Tengiz A., postgraduate student of the Instrument Making and Biomedical Engineering Department, Don State Technical University (1, Gagarin sq., Rostov-on-Don, 344003, RF), ORCID: <https://orcid.org/0000-0003-1709-9505>, khinikadze@mail.ru

Rybak, Alexandr T., professor of the Instrument Making and Biomedical Engineering Department, Head of the Certification and Professional Accreditation of Educational Programs Department, Don State Technical University (1, Gagarin sq., Rostov-on-Don, 344003, RF), Dr.Sci. (Eng.), professor, ORCID: <https://orcid.org/0000-0001-9950-3377>, 2130373@mail.ru

Popikov, Petr I., professor of the Forestry Mechanization and Machine Design Department, Voronezh State University of Forestry and Technologies named after G.F. Morozov (8, Timiryazeva St., Voronezh, 394087, RF), Dr.Sci. (Eng.), professor, ResearcherID: [AAX-7892-2020](https://orcid.org/0000-0002-6348-8934), ORCID: <https://orcid.org/0000-0002-6348-8934>, popikovpetr@yandex.ru

Claimed contributorship

T. A. Khinikadze: basic concept formulation; research objectives and tasks; computational analysis; text preparation; formulation of conclusions. A. T. Rybak: academic advising; analysis of the research results; the text revision; correction of the conclusions. P. I. Popikov: analysis of literature and patent materials, dynamic characteristics of the hydraulic drive.

All authors have read and approved the final manuscript.

MACHINE BUILDING AND MACHINE SCIENCE



UDC 621.791.75:004.942

<https://doi.org/10.23947/2687-1653-2021-21-1-62-70>

Consumable electrode – additional filler wire arc interaction control under surfacing (DE-GMAW)

S. S. Poloskov¹, V. A. Erofeev², M. A. Sholokhov³¹ Moscow Institute of Physics and Technology (National Research University) (Moscow, Russian Federation)² Tula State University (Tula, Russian Federation)³ Ural Federal University (Ekaterinburg, Russian Federation)

Introduction. Arc surfacing through feeding an additional filler wire heated by an additional arc burning between the filler wire and the electrode wire is considered. Under the conditions of such surfacing, the minimization of the input of the remelted substrate metal into the weld metal is studied. The research objectives are to examine the conditions providing self-regulation of this advanced arc surfacing process, and to evaluate control capabilities of the heat impact power on the metal and on the weld metal flow.

Materials and Methods. In solving a wide range of welding and surfacing tasks, it is advisable to use engineering analysis methods based on physicomathematical modeling of processes and phenomena. These include:

- self-regulation of the arc process under joint melting of the electrode and the filler wires;
- assessment of the possibilities to control the heat impact power on the metal and on the weld metal flow during the formation of the weld pool. The features of the arc surfacing of anticorrosive chromium-nickel steels on low-alloy steel are considered in the paper.

Results. New mathematical dependences are proposed that describe physical phenomena under surfacing with an arc interaction between the electrode and filler wire. A physicomathematical model of the joint melting of the electrode and filler wire is developed. It provides determining the values of the control parameters. In addition, you can find out how much heat affects the substrate from:

- heat release in the main arc,
- droplet flows of the weld electrode and filler metal,
- arc plasma radiation.

Discussion and Conclusions. It is established how the current and the lengths of the main and additional arcs are affected by the supply voltages. The feed rate of the electrode and filler wire with a diameter of 1.6 mm and 1.2 mm made of Inconel 625 alloy is determined. It is shown what thermal effect the substrate undergoes in this case. It is noted that due to the larger value of the main arc current, the diameter of the electrode wire should be larger than that of the filler wire. The heat flow in the substrate is created mainly by the flow of the weld metal droplets.

Keywords: physicomathematical model, arc interaction, surfacing, consumable electrode, filler wire.

Funding information: the research is done within the framework of the independent R&D on the formation of the scientific and technological groundwork for science-intensive products.

For citation: S. S. Poloskov, V. A. Erofeev, M. A. Sholokhov. Consumable electrode – additional filler wire arc interaction control under surfacing (DE-GMAW). Advanced Engineering Research, 2021, vol. 21, no. 1, p. 62–70. <https://doi.org/10.23947/2687-1653-2021-21-1-62-70>

© Poloskov S. S., Erofeev V. A., Sholokhov M. A., 2021



Introduction. Surfacing with materials whose characteristics differ markedly from the base metal, provides the necessary performance properties of the contact surfaces of the products. When surfacing, it is required to reduce the mixing of materials, so you need to adjust the power of the heat impact on the surface of the base metal, and the amount of melting material. In [1], the possibility of such regulation through changing the heat flow during the arc interaction of a melting electrode with an additional filler wire was first validated. Initially, this approach was used mainly in welding [2-4], and in recent years — in surfacing [5]. According to the author of the paper [6], this method of surfacing will help to provide high performance properties of the sealing and contact surfaces of pipeline fittings. However, a number of researchers have noted a factor that complicates the use of this method in welding and surfacing. They consider the major problem to be the filler wire feed control. At an insufficient feed rate, it can melt outside the molten pool, and at a high feed rate, it cannot melt. Therefore, to provide the required flow of the deposited material with a limited heat impact of the arc on the metal surface, it is necessary to accurately set the current of the additional arc burning between the wires. The working conditions, the instability of the wire feed, and the heterogeneity of their thermophysical properties also unpredictably change the melting conditions of the main electrode and the filler wire. Therefore, the surfacing process stability can be provided through using the self-regulation effect of the main and auxiliary arcs. The work objectives are to study conditions for the self-regulation of the arc process through co-melting of the electrode and filler wire, as well as to assess the possibility of heat power control for the metal and the filler metal flow.

Materials and Methods. When solving a number of problems, the use of engineering analysis methods based on physical and mathematical modeling of welding processes is challenging [7, 8]. Such models are a system of differential equations, whose boundary conditions take into account many technological factors. The equations are solved in an iterative cycle. An important advantage of this method of engineering analysis based on fundamental physical laws is the universality of the results and the possibility of using them to study the mechanisms of physical interactions in welding and surfacing processes [9]. Such phenomena include:

- self-regulation of the arc process under the joint melting of the electrode and filler wires,
- assessment of the possibility of controlling the power of thermal impact on the metal.

However, taking into account the effect of arc self-regulation, it is required to further investigate features of the joint melting of the electrode and filler wires. In addition, you need to know with what power the substrate is affected by heat from:

- heat generation in the main arc,
- droplet flows of the deposited electrode and filler metal,
- arc plasma radiation.

In this paper, we consider double-electrode gas metal arc welding, DE-GMAW, and electrode surface welding (a melting electrode and a current-carrying filler wire) in a protective gas.

Main Part. To study the mechanism of interaction between the main and additional arc between the electrode and filler wires, a physicomathematical model is required with account for the following:

- features of the melting of the electrode and filler wires,
- the effect of self-regulation of the thermal power of arcs under surfacing.

The numerical solution to the model equations in an iterative cycle provides a deeper study of the adjustment characteristics of the process and their influence on the thermal power of the surfacing.

Physical model of electrode and filler wire melting. Taking into account many significant factors, it is appropriate to use the approaches described in [10] when studying the features of self-regulation of melting of electrode and filler wires. However, the modeling space needs to be specified. Consider the refined modeling space for the melting conditions of the electrode and filler wire under the action of arcs. The first of them — *a* (Fig. 1) burns between the electrode wire 1 and the substrate 3, and the second *b* — between the electrode and the filler wire 2. In this case, in our opinion, it is suitable to feed the wire from the front of the molten pool. This will eliminate welding (“freezing”) of the unfused filler wire in the solidifying metal of the tail section of the molten pool.

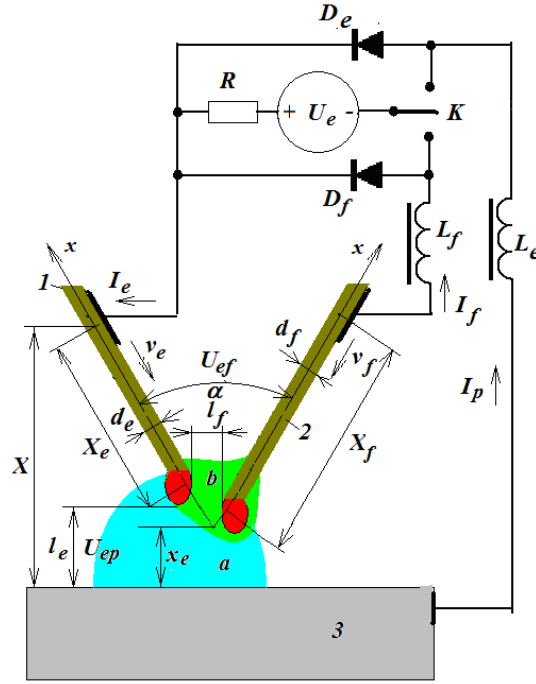


Fig. 1. Process chart of double-arc consumable electrode surfacing with an additional filler wire

To form a common plasma column of arcs a and b , the filler wire is fed at an angle α to the axis of the melting electrode x . This enables the axes of the filler and electrode wires to intersect at a given distance X from their current contact nozzles, and to set the distance x_e from the intersection point of the wire axes to the metal surface. In the simulation space, feed rates and wire diameters of the electrode wire v_e, d_e and the filler wire v_f, d_f are also set.

For the main arc a , voltage U_{ep} is given, and for the additional arc b — U_{ef} . These voltages are regulated by the key K , which redistributes voltage U_e of the power supply between the arcs. The continuity of arc currents I_e, I_f are provided by chokes L_e, L_f and closing diodes D_e, D_f . Arc currents I_e, I_f are self-adapted through a self-regulatory effect of lengths l_e, l_f of the corresponding arcs. The lengths of the electrode stickouts X_e, X_f are determined through the melting of the electrodes. The melting rates are determined by the arc currents I_e, I_f and the voltage drop in the anode regions, as well as by the heating of the stickouts by the arc currents passing through them. R — electrical resistance of the power supply.

Mathematical model of the surfacing process self-regulation. The main control action on the process is provided by the operation of the key K . Its closures (with a period of τ and duration of t_e, t_f) regulate the voltage on the electrodes:

$$U_{ep} = (U_e - (R_e + R)I_e) \frac{t_e}{\tau}; U_{ef} = (U_e - (R_f + R_e + R)I_f) \frac{t_f}{\tau}, \quad (1)$$

where R_e, R_f — electrical resistances of the electrode and filler wire stickouts.

In the steady-state mode, these voltages determine the arc lengths [11]:

$$l_e = \frac{1}{E}(U_{ep} - U_a - U_k); l_f = \frac{1}{E}(U_{ef} - U_a - U_k), \quad (2)$$

where U_a, U_k — voltage drop in the anode and cathode regions of the arc; E — potential gradient in the arc column.

It is advisable to determine the average values of the arc currents through the melting rates of the wires, which, in the steady-state mode, are equal to the rates of their supply:

$$I_f = \frac{v_f \pi d_f^2}{4U_k} (c\rho(T_k - T_{Xf}) + q_{LS}), I_e = \frac{v_e \pi d_e^2}{4U_a} (c\rho(T_k - T_{Xe}) + q_{LS}), \quad (3)$$

where T_k — temperature of electrode metal drops; $c\rho$ — heat capacity of metal of wires; q_{LS} — melting heat; T_{Xe}, T_{Xf} — preheat temperatures of wire stickouts by arc currents.

It should be taken into account that with pulse regulation, the current will change with the period τ and the amplitude:

$$\Delta I = \frac{U_e \tau}{L}. \quad (4)$$

However, with a small period of change, typical for modern power supplies, the periodic change in current can be ignored.

Current flowing through the cathode spot on the metal surface:

$$I_k = I_e - I_f. \quad (5)$$

To find out the temperature distribution along the stickout axes x of the electrode $T_e(x)$ and filler $T_f(x)$ wires, it is required to consider the dependence of the electric resistivity of the wire metal on the temperature $\rho_e(T)$ [12].

Then the temperature distribution is:

$$T_e(x) = \left(\frac{4I_e}{\pi d_e^2}\right)^2 \frac{1}{v_{ecp}} \int_0^x \rho_e(T_e(x)) dx, T_f(x) = \left(\frac{4I_f}{\pi d_f^2}\right)^2 \frac{1}{v_{fcp}} \int_0^x \rho_e(T_e(x)) dx. \quad (6)$$

The preheat temperature T_{Le} is determined from its values at the end of the stickout $x = X_e$

As noted in [13, 14], the temperature of the metal drops T_k entering the weld (molten) pool is determined by a combination of many factors. However, in any case, it will be in the range between the melting point T_L and the boiling point T_V of the metal:

$$T_k \approx \frac{T_V + T_L}{2}. \quad (7)$$

The heat dissipation power is calculated using the following formulas.

— For the cathode arc spot:

$$P_k = U_k(I_e - I_f) \quad (8)$$

— Transferred by electrode droplets:

$$P_e = U_a I_e + c_p T_{Xe} v_e \frac{\pi d_e^2}{4}. \quad (9)$$

— From the flow of filler wire droplets:

$$P_f = U_k I_f + c_p T_{Xf} v_f \frac{\pi d_f^2}{4}. \quad (10)$$

The arc column radiation power:

$$P_{rad} = E(I_f l_f + I_e l_e). \quad (11)$$

Only a part of the arc radiation reaches the surface of the substrate. Note that the radiation intensity is inversely proportional to the square of the distance from the radiation center. Assume that this center is removed from the substrate surface by the length of the main arc. Then, the power on the surface of the substrate:

$$P_r = \frac{P_{rad}}{2} \iint_S \frac{dS}{r^2 + l_e^2}, \quad (12)$$

where S — surface area, r — the distance from the surface to the arc torch axis.

The numerical solution to the model equations is reduced to an iterative selection of arc currents, in which equality is achieved in all relations (Fig. 2).

Source data: metal grade and surfaced material, dimensions X_1, X_2, x_e the surfacing mode parameters $v_e, d_e, v_f, d_f, U_e, R, \tau, t_e, t_f$. Material properties from the databases $T_v, T_L, c_p, q_{LS}, U_a, U_k, E, \rho_e(T)$.	
Initial approximation	
Iterative cycle of current refinement I_e, I_f	
Calculation of temperature distribution in stickouts: $x = 0, T(x) = T_0, R_e = 0, R_f = 0$	
Cycle $x = x + dx$	
	$T_e(x) = T_e(x) + \left(\frac{4I_e}{\pi d_e^2}\right)^2 \frac{\rho_e(T_e(x))}{v_{ecp}} dx, T_f(x) = T_f(x) + \left(\frac{4I_f}{\pi d_f^2}\right)^2 \frac{\rho_e(T_f(x))}{v_{fcp}} dx$
	Electric resistivity of the stickouts: $R_e(x) = R_e(x) + \frac{\rho_e(T_e(x))}{\pi d_e^2} dx, R_f(x) = R_f(x) + \frac{\rho_e(T_f(x))}{\pi d_f^2} dx$
as long as $x < X_e$ or $x < X_f$	
Parameters of stickouts $T_{Le} = T_e(L_e), T_{Lf} = T_f(L_f), R_e = R_t(L_e), R_f = R_f(L_f)$	
Clarification of currents $I_f = \frac{1}{4} \left[3I_f + \frac{v_f \pi d_f^2}{4U_k} (c_p(T_k - T_{Xf}) + q_{LS}) \right], I_e = \frac{1}{4} \left[3I_e + \frac{v_e \pi d_e^2}{4U_a} (c_p(T_k - T_{Xe}) + q_{LS}) \right]$	
until I_e const or I_f const	
Determination of process parameters: $D = k_D (I_e + I_f)^{\frac{2}{3}} + d_e$; $P_e = U_a I_e + c_p T_{Xe} v_e \frac{\pi d_e^2}{4}, P_f = U_k I_f + c_p T_{Xf} v_f \frac{\pi d_f^2}{4},$ $P_r = \frac{E}{2} (I_f l_f + I_e l_e) \iint_S \frac{dS}{r^2 + l_e^2}, l_e = \frac{1}{E} (U_{ep} - U_a - U_k); l_f = \frac{1}{E} (U_{ef} - U_a - U_k).$	

Fig. 2. Algorithm for calculating the parameters of the joint melting process of electrode wires

The algorithm for calculating the parameters of the joint melting process of electrode wires presented in Fig. 2 enables to study in detail the conditions of self-regulation of the main and additional arcs under surfacing.

Research Results

Process control characteristics. Regulatory actions:

- the feed rate of the electrode and filler wires,
- the no-load voltage of the power supply,
- the relative duration of the key closures, which controls the ratio of the voltages of the main and additional arcs.

These actions determine the arc currents, their lengths, and the power distribution of the process. Additional parameters that determine the results of regulation are the wire diameters, their stickouts, and the angles between them.

The ranges of control parameters values are limited. The most important of them is the condition for the existence of an arc between the substrate and the electrode, i.e., the current $I_k = I_e - I_f > 0$ through the cathode spot on the substrate.

Accordingly, the relation should be fulfilled:

$$\frac{v_e d_e^2}{U_a} > \frac{v_f d_f^2}{U_k}. \quad (13)$$

The second critical limitation is the minimum voltage on the arcs, which provides their stable arcing in the absence of short circuits:

$$U_e \frac{t_e}{\tau} > U_a + U_k; U_e \frac{t_f}{\tau} > U_a + U_k. \quad (14)$$

In addition, it is required to provide the correct location of the vanishing point of the electrodes above the substrate surface and the deposited layer, and the absence of short circuits by the electrode metal drops, i.e., the length of the main arc should be:

$$l_e > x_e + l_f \operatorname{ctg} \frac{\alpha}{2}; x_e > d_e. \quad (15)$$

To do this, the main arc voltage should be at least:

$$U_e \frac{t_e}{\tau} > U_a + U_k + E l_e. \quad (16)$$

The length of the additional arc l_f is a process parameter that provides removing the flow of additive drops from the main arc.

Influence of the control parameters on the process power. The power of the heat fluxes acting on the substrate in the sum of the heat release in the cathode spot of the main arc, the radiation power of the main and additional arcs, heat transfer by drops of the electrode and filler metal. Fig. 3 shows the effect of the feed rate of the electrode wire with a diameter of 1.6 mm made of Inconel 625 alloy on:

- current I_e of the main arc,
- power P_k , emitted in the cathode spot,
- power P_e of the heat flux drops of electrode metal,
- temperature T_e of heating the electrode stickout,
- length l_e of the main arc.

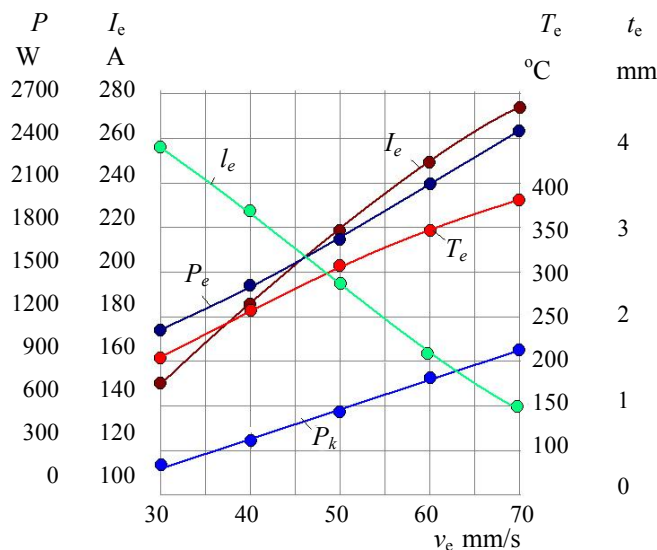


Fig. 3. Dependence of the main arc parameters on the feed rate v_e of the electrode with a diameter of $d_e = 1.6$ mm made of Inconel 625 alloy at stickout of $l_e = 10$ mm, supply voltage $U_e = 32$ W, duty cycle $t_e/\tau = 0.5$, and the additional arc current $I_f = 108$ A

With an increase in the speed v_e of the electrode wire feed at a fixed current I_f of the additional arc, the current I_e , flowing through the electrode, increases almost in proportion to the speed. The deviation from the proportionality is explained by a noticeable increase in the temperature T_e of the electrode stickout. For the same reason, the power P_e that heats the electrode increases faster than the arc current I_e . The power P_k , released in the cathode spot on the substrate surface is almost proportional to the feed rate, but it is much less than the thermal power P_e of the droplet flow. The length l_e of the main arc decreases linearly as the electrode feed rate increases.

Fig. 4 shows the impact of the feed speed v_f of the filler wire with a diameter of 1.2 mm made of Inconel 625 alloy on:

- additional arc current I_f ,
- power P_k generated in the cathode spot,
- power P_f of the heat flux drops of metal filler wire,
- temperature T_f of the heated wire stickout,
- length l_f of the additional arc.

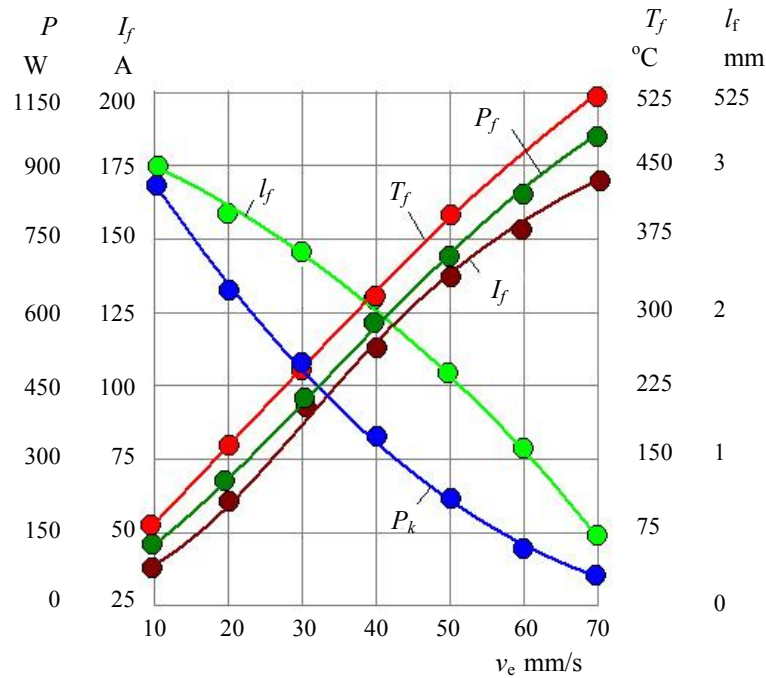


Fig. 4. Dependence of the additional arc parameters on the feed speed v_f of the filler wire with a diameter of $d_e = 1.2$ mm made of Inconel 625 alloy at stickout of $l_e = 10$ mm, supply voltage $U_e = 32$ W, duty cycle $t_f / \tau = 0.5$, and the main

With an increase in the feed rate v_f of the filler wire at a fixed current I_e of the main arc, the current I_f is somewhat disproportionate to the feed rate due to a noticeable increase in the temperature T_f of the wire stickout. The power P_e , spent on heating the wire increases faster than the current I_f of the additional arc. The power P_k , generated in the cathode spot on the substrate surface, is greatly reduced through increasing the feed rate of the filler wire due to the redistribution of the main arc current to the filler wire. The thermal power P_f of the flow of the droplets from the filler wire is less than the power P_e of droplets from the electrode. The length l_f of the additional arc decreases non-linearly as the feed rate increases. This is due to the impact of the electrical resistance, which is greater in the filler wire than in the electrode stickout due to the smaller wire diameter and higher temperature T_f . The voltage of the arcs determines their length, i.e., their location above the substrate.

Fig. 5 shows how the distance between the electrode and filler wire and their distance from the substrate depend on the surfacing mode.

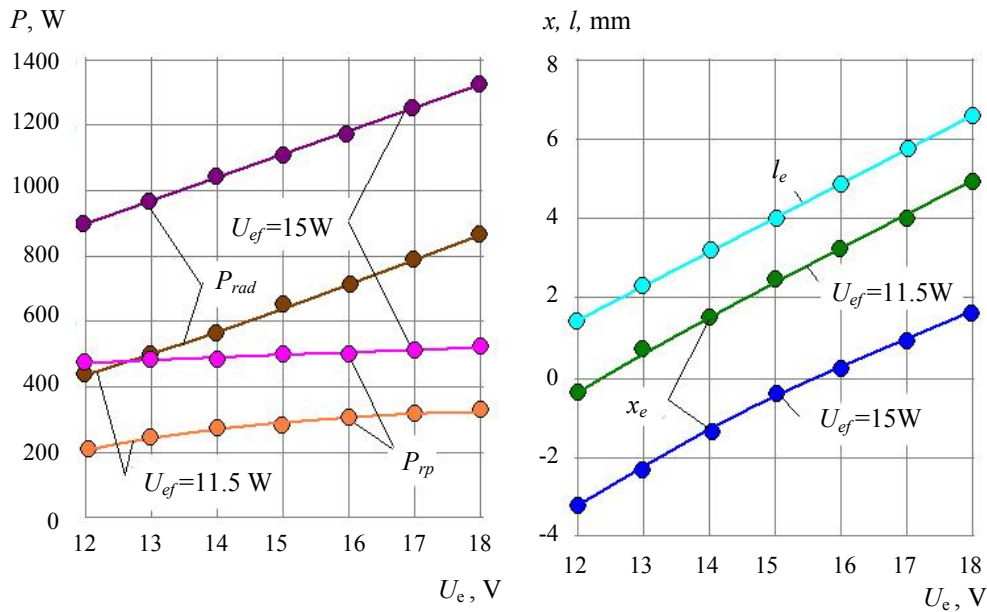


Fig. 5. Impact of the main arc voltage U_{ep} at different additional arc voltage U_{ef} on: arc radiation power P_{rad} , arc radiation power on the substrate P_{rp} , main arc length l_e , main arc length x_e from the vanishing point of the electrodes to the substrate

The minimum arc voltage (12 V) is determined from the sum of the anode and cathode voltages, as well as their minimum length. The voltage U_{ef} is set between the electrode wire and the filler wire. At the same time, an increase in the voltage U_{ep} between the electrode and the substrate increases the length l_e of the main arc, which is accompanied by an increase in the power P_{rad} of heat release in the plasma arc torch. Raising the voltage U_{ef} between the electrode and the additive increases the length l_f of the additional arc, which also increases the power P_{rad} . Some part P_{rp} of this power P_{rad} is radiated to the substrate surface. The dependence of the total power P_{rad} of the arc torch on the voltage of the main arc U_{ep} is noticeable. At the same time, a change in the power P_{rp} that heats the substrate is less significant. This is due to the removal of the arc plasma from the substrate as the length l_e of the main arc increases. The voltage of the additional arc U_{ef} affects the heating power P_{rp} of the radiation much more strongly, since the distance between the arc torch and the substrate does not depend on this voltage. Voltages U_{ep} and U_{ef} affect significantly the location of the wire vanishing point x_e , which imposes restrictions on the power supply of the arcs.

Discussion and Conclusions. Surfacing with the electrode and filler wire arc interaction enables to adjust the power consumed for melting the deposited metal and for heating the substrate. The stability of consumable-electrode arc welding is usually provided by the self-regulating effect, which equalizes the melting and feeding rates of the electrode wires when they change over a wide range. The physicomathematical model of joint melting of electrode and filler wires is developed with account for self-regulation, in which the control actions are the wire feed rates and the voltage on the welding torches, while the currents and arc lengths are the results of self-regulation. The model provides determining the values of the control parameters, as well as the power of the thermal effect on the substrate under the consumable-electrode surfacing with additional filler wire.

Based on the results of the work performed, the following conclusions can be drawn.

1. Under the consumable-electrode arc surfacing with additional filler wire, to effectively regulate the ratio between the volumes of the surfaced material and the remelted substrate, the following self-regulation should be provided:

- of the main arc between the electrode and the substrate,
- of the additional arc between the electrodes.

2. Self-regulation of the arc melting process of the electrode and filler wires is described by a system of equations. In it, the control actions are the wire feed rates and the voltages of the main and additional arcs, and the control results are the arc currents, their lengths, the distribution of heat generation power, the heat fluxes of the electrode metal droplets and the arc radiation on the substrate surface.

3. Limits are set on:

— the ratio of the parameters of the feed of the electrode and filler wire, which provide the presence of an arc between the electrode and the substrate;

— minimum voltage across arcs maintaining their stable burning in the absence of short circuits.

4. Calculations of the modes of consumable-electrode surfacing with an additional filler wire of the Inconel 625 alloy are performed. The calculations show that the process can be controlled over a wide range of wire feed rates and burner voltages.

References

1. Zhang YM, Jiang M, Lu W. Double electrodes improve GMAW heat input control. *Welding Journal*. 2004;83(11):39–41.
2. Li KH, Zhang YM. Consumable double-electrode GMAW. Part 1: The process. *Welding Journal*. 2008;87(1):11–17.
3. Li KH, Zhang YM. Consumable double-electrode GMAW. Part II: Monitoring, modeling and control. *Welding Journal*. 2008;87(2):44–50.
4. Yi Lu, Shu Jun Chen, Yu Shi, et al. Double-Electrode Arc welding process: Principle, variants, control and developments. *Journal of Manufacturing Processes*. 2014;16(1):93–108.
5. Günther K, Bergmann JP, Suchodoll D. Hot wire-assisted gas metal arc welding of hypereutectic FeCrC hardfacing alloys: Microstructure and wear properties. *Surface and Coatings Technology*. 2018;334:420–428.
6. Poloskov SS. Problemy naplavki uplotnitel'nykh poverkhnostei truboprovodnoi armatury i puti ikh resheniya [Problems of weld overlay of sealing surfaces of pipe fitting and solutions]. *Vestnik of DSTU*. 2019;19(4):349–356. DOI: <https://doi.org/10.23947/1992-5980-2019-19-4-349-356>. (In Russ.)
7. Shipilov AV, Erofeev VA, Vyshemirsky EM, et al. Fiziko-matematicheskaya model' orbital'noi svarki neplavyashchimsya ehlektrodom v inertnykh gazakh: kontseptsiya i vozmozhnosti [Physical and mathematical model of orbital non-consumable electrode welding in inert gases: concept and possibilities]. *Welding and Diagnostics*. 2011;2:3–9. (In Russ.)
8. Winczek J, Rygal G. Modelling of a temporary temperature field during arc weld surfacing of steel elements taking into account heat of the weld. *Journal of Applied Mathematics and Computational Mechanics*. 2015;14(1):111–120.
9. Murphy AB. A perspective on arc welding research: The importance of the arc, unresolved questions and future directions. *Plasma Chemistry & Plasma Processing*. 2015;35(3):471–489.
10. Poloskov SS, Yerofeyev VA, Sholokhov MA. Fiziko-matematicheskaya model' dugovogo vzaimodeistviya pri naplavke plavyashchimsya ehlektrodom s dopolnitel'noi prisadochnoi provolokoi [Physics-mathematical model of arc interaction when smelting a melting electrode with additional additive wire]. *Welding and Diagnostics*. 2019;6:27–31. (In Russ.)
11. Getskin OB, Erofeev VA, Poloskov SS, et al. Fiziko-matematicheskaya model' sistemy «istochnik pitaniya — duga» dlya svarki plavyashchimsya ehlektrodom v zashchitnykh gazakh [Physical and mathematical model of the system “power source – arc” for MIG/MAG welding]. *Tyazheloe Mashinostroyeniye*. 2008;6:18–20. (In Russ.)
12. Waszink H, Van den Heuvel CJPM. Heat generation and heat flow in the filler metal in GMA welding. *Welding Journal*. 1982;61(8):269–280.
13. Lenivkin VA, Dyurgerov NG, Sagirov KhN. Tekhnologicheskie svoystva svarochnoi dugi v zashchitnykh gazakh [Technological properties of the welding arc in protective gases]. Moscow: Mashinostroyeniye; 1989. 264 p. (In Russ.)
14. Chuan Song Wu. Computer simulation of three-dimensional convection in traveling MIG weld pools. *Engineering Computations*. 1992;9(5):529–537.

About the Authors:

Poloskov, Stanislav S., Director of Analytical Center, Moscow Institute of Physics and Technology (National Research University) (9, Institutsky per., Dolgoprudny, Moscow Region, 141701, RF), Scopus ID [57190177358](https://orcid.org/0000-0002-8205-3565), ORCID: <http://orcid.org/0000-0002-8205-3565>, stanislavpoloskov@gmail.ru

Erofeev, Vladimir A., professor of the Welding, Casting and Technology of Structural Materials Department, Tula State University, (92, Lenin Ave., Tula, 300600, RF), Cand.Sci. (Eng.), ORCID: <https://orcid.org/0000-0003-3756-2640>, Va_erofeev@mail.ru

Sholokhov, Mikhail A., Head of the Welding Production Automation and Robotization Department, Yeltsin Ural Federal University (UrFU) (19, Mira St., Ekaterinburg, 620002, Russia), Dr.Sci. (Eng.), ORCID: <https://orcid.org/0000-0002-7666-5645>, M.a.sholokhov@urfu.ru

Claimed contributorship

S. S. Poloskov: definition of the modeling area and boundary conditions; analysis of the research results, text preparation; formulation of conclusions. V. A. Erofeev: physicomathematical model development; analysis of the research results. M. A. Sholokhov: academic advising; the text revision; correction of the conclusions.

All authors have read and approved the final manuscript.

MACHINE BUILDING AND MACHINE SCIENCE



UDC 621.65; 004.92

<https://doi.org/10.23947/2687-1653-2021-21-1-71-81>

Strength analysis of the TWS 600 plunger pump body in Solid Works Simulation

E. V. Koleda¹, S. O. Kireev¹, M. V. Korchagina¹, A. V. Efimov¹, J. Sperling²¹Don State Technical University (Rostov-on-Don, Russian Federation)²ACT Well Services GmbH (Diesdorf, Federal Republic of Germany)

Introduction. The relevance of the presented paper is due to the widespread use of plunger pumps in industrial practice, in particular, in gas and oil production. The quality of working operations and the efficiency of further well operation depend largely on their reliability. The improvement of plunger pumps involves increasing their reliability, increasing their service life, efficiency, downsizing, reduction in weight, labor intensity of installation and repair work. The modernization of the mechanism includes its power study since the found forces are used for subsequent strength calculations. Before the appearance of programs for the numerical analysis of solid objects, the analytical solution to the problem of strength calculation of the high-pressure pump drive frame was a very time-consuming and expensive procedure. The situation has changed with the development of computer technologies and the inclusion of the finite element method in the computer-aided design systems. The objective of this work is to perform a strength calculation on the TWS 600 plunger pump body made of 09G2S steel.

Materials and Methods. A method for determining the reactions of the crank shaft supports of a high-pressure plunger pump and strength calculation of the drive part housing is developed. The direction and magnitude of the resulting forces and reactions of the supports are determined graphically according to the superposition principle of the force action on the supports. Strength calculations were performed using the finite element method in the computer-aided design system Solid Works Simulation. In this case, solid and finite-element models of the body with imposed boundary conditions were used, which were identified during the analysis of the design and the calculation of the forces arising under the pump operation.

Results. The reactions in the crankshaft supports are described with account for the forces generated by the plunger depending on its operating mode and the crank position. The forces acting on each of the plungers and the resulting reactions in each of the supports are determined. The diagrams of stresses and the safety factor are presented, which provide assessing the strength of the body and developing recommendations for creating a more rational design.

Discussion and Conclusions. As a result of the calculations, we have identified areas of the structure with minimum safety factors, and areas that are several times higher than the recommended values. This provides optimizing the design under study through strengthening the first and reducing the thickness of the metal on the second. From the point of view of weight and size characteristics and maintainability, the results of the strength calculation performed can be used to optimize the design of the pump body under typical operating conditions.

Keywords: plunger pump, support reactions, strength calculation, design optimization, superposition principle, calculation of body parts.

For citation: E. V. Koleda, S. O. Kireev, M. V. Korchagina, et al. Strength analysis of the TWS 600 plunger pump body in Solid Works Simulation. Advanced Engineering Research, 2021, vol. 21, no. 1, p. 71–81. <https://doi.org/10.23947/2687-1653-2021-21-1-71-81>

Funding information: the research is done within the frame of the independent R&D no. AAAA-A20-120012190068-8 of 21.01.2020.

© Koleda E. V., Kireev S. O., Korchagina M. V., Efimov A. V., Sperling J., 2021



Introduction. Oil production is not complete without the use of plunger pumps. They are required for such working operations as well cementing and acidizing, sand blast perforation, hydrofracturing, etc. [1]. Downsizing and reduction in weight of the pumps make them extremely attractive for use in mobile oilfield installations. The reliability of the pumps largely determines the quality of processing and the efficiency of further operation of oil and gas wells [2].

Despite the overall rather high level of plunger pump designs, they continue to be improved. The improvement of plunger pumps involves increasing their reliability, increasing their service life, efficiency, downsizing, reduction in weight, labor intensity of installation and repair work. For this purpose, the designs of the components and parts of the drive and hydraulic systems are changed [3–5]. The modernization of the mechanism includes its power study since the found forces are used for subsequent strength calculations. Recently, in connection with the development of computer technologies, numerical methods of strength analysis with the use of applied programs are increasingly used [6, 7].

Before the appearance of programs for the numerical analysis of solid objects, the analytical solution to the problem of strength calculation of the high-pressure pump drive frame was a very time-consuming and expensive procedure [8–10]. The development of the finite element method (FEM) in the deformable solid mechanics and its inclusion in computer-aided design systems (CAD, e.g., Solid Works Simulation) opens up new opportunities in solving problems of this kind. Strength calculations performed in CAD provide optimizing the design of the body parts. For the design under consideration, the body is one of the critical parts that takes up the load and provides the correct mutual arrangement of the drive part elements.

To obtain reliable results in the strength analysis of the pump body using numerical methods in CAD, it is required to determine all external loads acting on the body.

The widely used TWS 600 triplex plunger pump was selected as the object of modernization. In Russia, structural low-alloy 09G2S steel is used for manufacturing body parts of high-pressure plunger pumps [11]. Replacing the material of the body parts of TWS 600 plunger pump with 09G2S steel will reduce the cost. In this regard, this work objective is to analyze the possibility of replacing the material of the body of TWS 600 plunger pump with 09G2S steel to optimize the price and provide the possibility of repair work.

Materials and Methods. The replacement of the material should be validated by the strength calculation. The calculation of the body was carried out by the FEM in the CAD Solid Works Simulation.

The external forces acting on the pump body are reactions in the crankshaft supports. They arise from the action of the inertia forces of the reciprocating moving parts of the crosshead connecting rod group and the forces of fluid pressure on the plunger. To determine the reactions in the crankshaft supports, it is required to perform a dynamic calculation of the slide-crank mechanism of the plunger pump¹.

As mentioned in [12, 13], tasks of the dynamic analysis include studying the influence of external and internal forces on the links and kinematic pairs of the mechanism, as well as identifying ways to reduce dynamic loads.

The crankshaft in question consists of two main journals on the major shaft axis and three crank journals eccentrically arranged at 120° offset. The bearing supports are located on the main journals and on the crank webs between the crank journals (Fig. 1).

¹ Timofeev GA. Theory of machines and mechanisms: a course of lectures. Moscow, 2010. 351 p. (In Russ.)

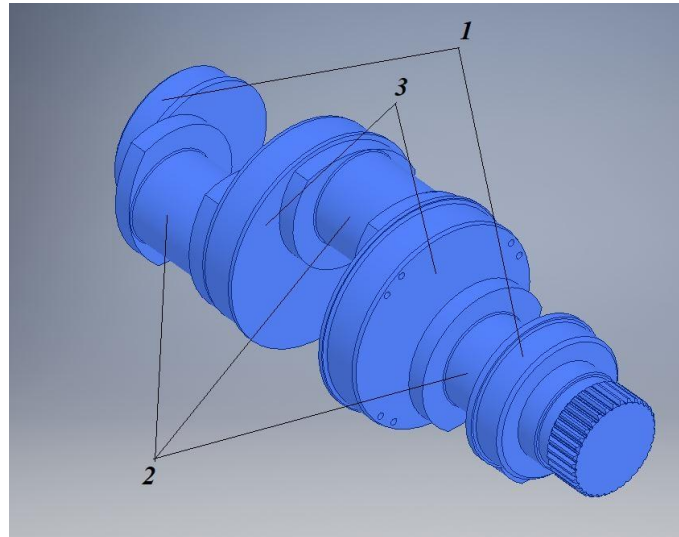


Fig. 1. Crankshaft of TWS 600 plunger pump: 1 — main journals; 2 — crank journals; 3 — webs

During the operation of the pump, three plungers reciprocate successively to provide discharge or suction (Fig. 2).

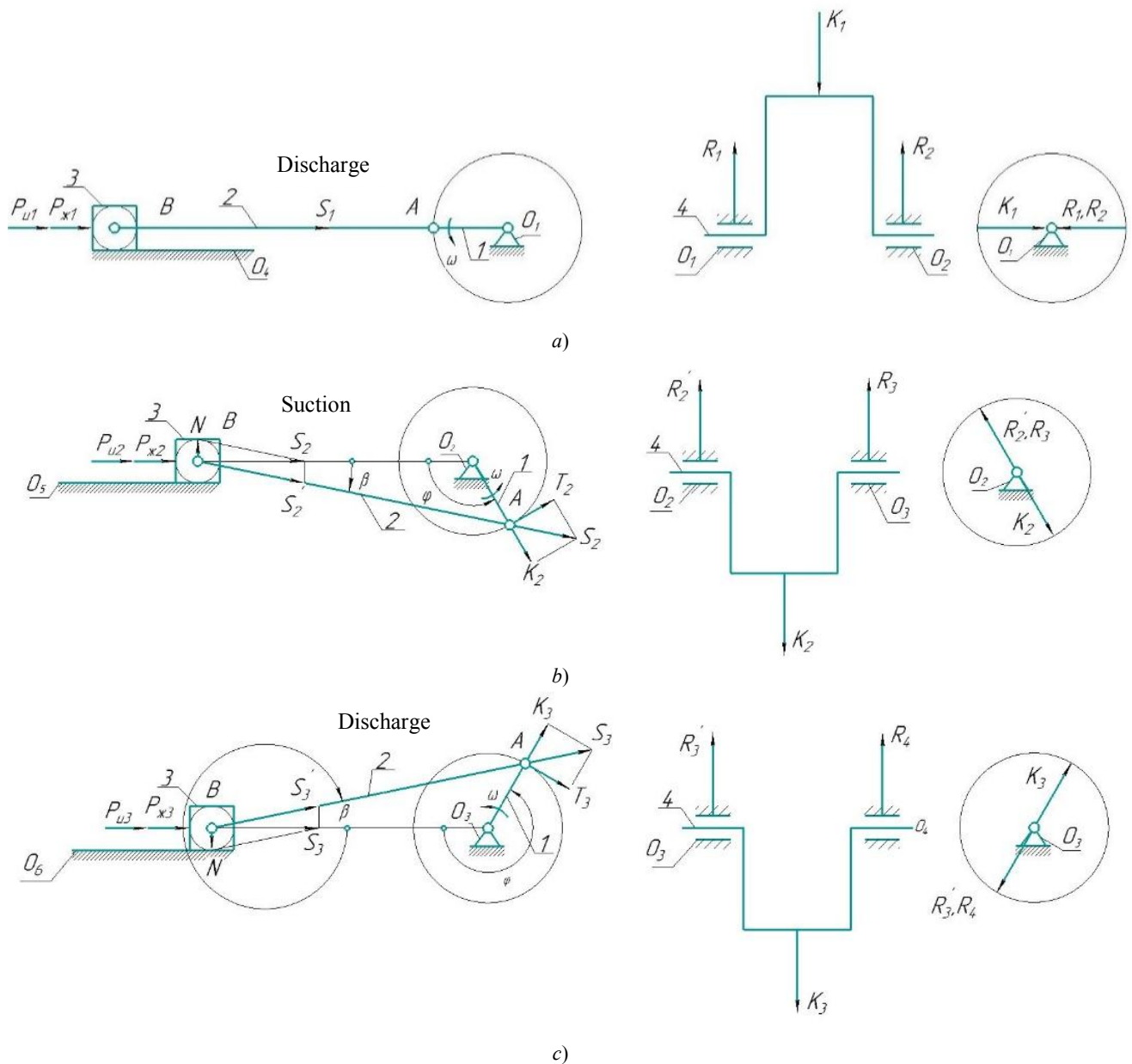


Fig. 2. Design diagram of the mechanism of the drive part of the plunger pump: a) position of the 1st plunger; b) position of the 2nd plunger; c) position of the 3rd plunger

Consider the position of the mechanism in which the first plunger is located at the extreme discharge point (ex. p.) and is under maximum load. The angle of rotation of the crank journal for this plunger is zero (Fig. 2 a). Then, the second plunger performs suction (Fig. 2 b), its journal is displaced by 120° . The third plunger operates for the discharge (Fig. 2 c), the journal is displaced by 240° . Thus, in one situation, the crankshaft is loaded with forces of different magnitude, and the reactions of the supports will be different. This occurs when the crank is in the position when the first plunger is at the extreme point of discharge, the second performs suction, and the third operates for discharge. We will perform the calculation for the specified position of the crank (mechanism) [8-10], and then, for other positions: when the second and third plungers will reach the extreme discharge point.

Link masses were calculated in the Autodesk Inventor Professional 2018 program based on the previously created 3D model of the drive of the TWS 600 plunger pump. A design diagram of the mechanism of the drive part of the plunger pump was constructed with an indication of the forces acting on its links (Fig. 2).

Let us denote the external forces for finding the crank shaft reactions: $P_{\text{ж}}$ — fluid pressure force, P_u — inertia force.

The fluid pressure force acting on the plunger is found from the expression:

$$P_{\text{ж}} = p_{\text{ж}} \cdot \pi \cdot r^2,$$

where $p_{\text{ж}}$ — pressure of the pumped liquid applied to the plunger; r — radius of the section of the plunger¹.

The inertia force of the reciprocating moving parts is:

$$P_u = -m \cdot i = -m \cdot r \cdot \omega^2 \cdot (\cos \varphi + (2 \cdot \cos^2 \varphi - 1)),$$

$$m = m_k + 0,275 \cdot m_{\text{ш}},$$

where m_k — crosshead mass, $m_{\text{ш}}$ — mass of the upper connecting rod head, r — crank radius, ω — crankshaft speed at 230 rpm, φ — crankshaft angle.

The force acting on the plunger is determined from the formula:

$$P_{\Sigma} = P_{\text{жи}} + P_{ui},$$

where $P_{\text{жи}}$ — pressure force of the pumped liquid in each position of the plunger, P_{ui} — inertia force of the reciprocating moving parts in each position of the plunger.

Total force P_{Σ} , applied to the crosshead pin axis and directed along the axis of the cylinder, can be decomposed into:

- force N acting perpendicular to the axis of the cylinder;
- force S acting on the axis of the connecting rod.

N presses the crosshead against the cylinder wall, which causes wear on their surfaces. This force changes in value and direction, alternately pressing the crosshead to one or the other side of the guides.

The force S , transferred to the of the crankpin axis, can be decomposed into:

- tangential force T , acting perpendicular to the crank of the crankshaft;
- radial force K , directed along the crank axis.

The force K is determined from the formula:

$$K_i = P_{\Sigma i} \cdot \frac{\cos(\varphi_i + \beta_i)}{\cos \beta},$$

where φ_i — crank angle (Fig. 2); β_i — angle of deviation of the connecting rod from the axis (Fig. 2); $P_{\Sigma i}$ — total force acting on the plunger.

The results of calculating radial forces for all crank journals in each considered position of the mechanism are summarized in Table 1.

¹Catalog of high-pressure plunger pumps manufactured by Weir SPM, Nord-SPM LLC. URL: http://виерспм.рф/catalogues/JI2IK_KATAJIOГ HACOCOB.pdf (accessed: 14.02.2021). (In Russ.)

Table 1

The results of calculating radial forces for all crank journals
in each considered position of the mechanism

Mechanism position								
I			II			III		
Plunger position								
1	2	3	1	2	3	1	2	3
ex.p.	suction	discharge	discharge	ex.p.	suction	suction	discharge	ex.p.
φ, degree								
0	120	240	240	0	120	120	240	0
K, H								
450000	−2503	−306687	−306687	450000	−2503	−2503	−306687	450000

The reactions of the supports are directed opposite to the radial forces (Fig. 3), and their values are determined from the formulas:

$$R_1, R_2 = \frac{K_1}{2},$$

$$R'_2, R_3 = \frac{K_2}{2},$$

$$R'_3, R_4 = \frac{K_3}{2},$$

where K_1, K_2, K_3 — radial forces directed along the crank axis.

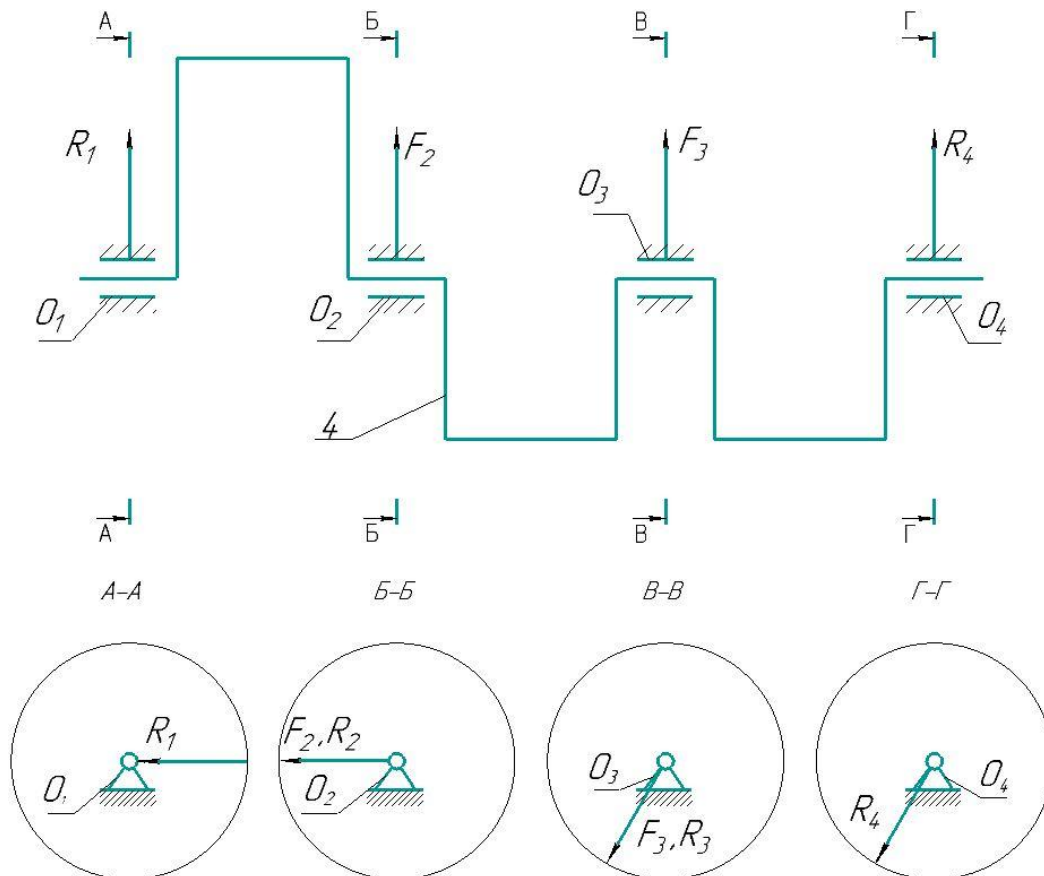


Fig. 3. Scheme of reactions of supports

The direction and magnitude of the resulting forces F_2 and F_3 of the reactions of the supports O_2, O_3 are determined graphically (see Fig. 3) according to the principle of superposition of the force action on the supports.

The resulting forces F_2 and F_3 coincide in magnitude and direction with the forces R_2 and R'_3 , respectively.

Numerical values and directions of reference reactions are found for the position of the mechanism at which the first plunger was at the discharge extreme point (see Fig. 2 a), the second performed suction (see Fig. 2 b), and the

third — discharge (Fig. 2 *b*). For other positions of the mechanism, the reactions of the supports are determined similarly and will be numerically equal, alternately changing places.

Table 2 shows the results of calculating the reactions of the crankshaft supports for the positions of the mechanism in which each of the plungers is alternately located at the extreme discharge point.

Table 2

Numerical values of the reactions of the supports for all positions of the mechanism

Mechanism position	Plunger position			Reaction forces of the supports			
				R_1, H	F_2, H	F_3, H	R_4, H
I	1	2	3	225000	225000	153343	153343
	ex.p.	suction	discharge				
II	1	2	3	153343	329602	225000	1251
	discharge	ex.p.	suction				
III	1	2	3	1251	153343	329602	225000
	suction	discharge	ex.p.				

The body of the high-pressure plunger pump was modeled in Autodesk Inventor Professional 2018 CAD system. The model includes bearing cages since the presence of a cage significantly affected the nature of the load application.

The strength analysis is performed by the FEM in the computer-aided design system Solid Works Simulation.

Fig. 4 *a* shows a solid model of the calculated structure, and Fig. 4 *b* shows a finite-element model.

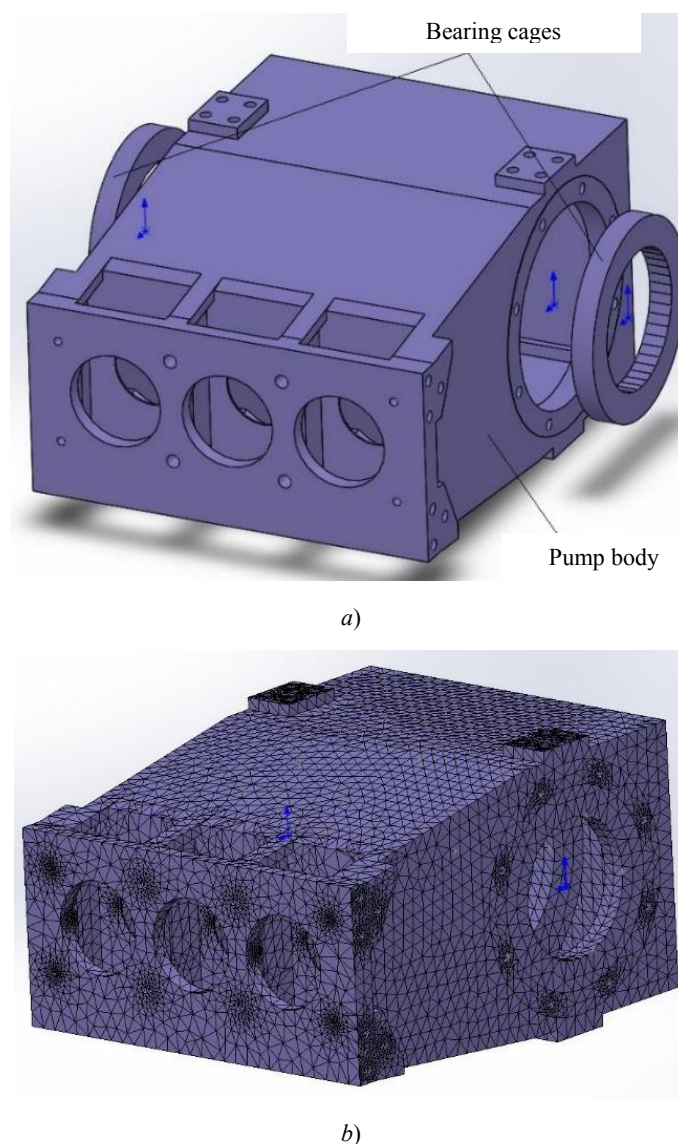


Fig. 4. Body models of the TWS 600 three-plunger high-pressure pump: *a*) solid-state, *b*) finite-element

The finite element model contains 100,747 elements (175,172 nodes). The body material is 09G2S steel. The model describes the loads and records the movements in all directions of the surfaces of the bolt holes. Fig. 5 shows the boundary conditions for the contacting surfaces. By the type of contacts, the surfaces are connected to common nodes.

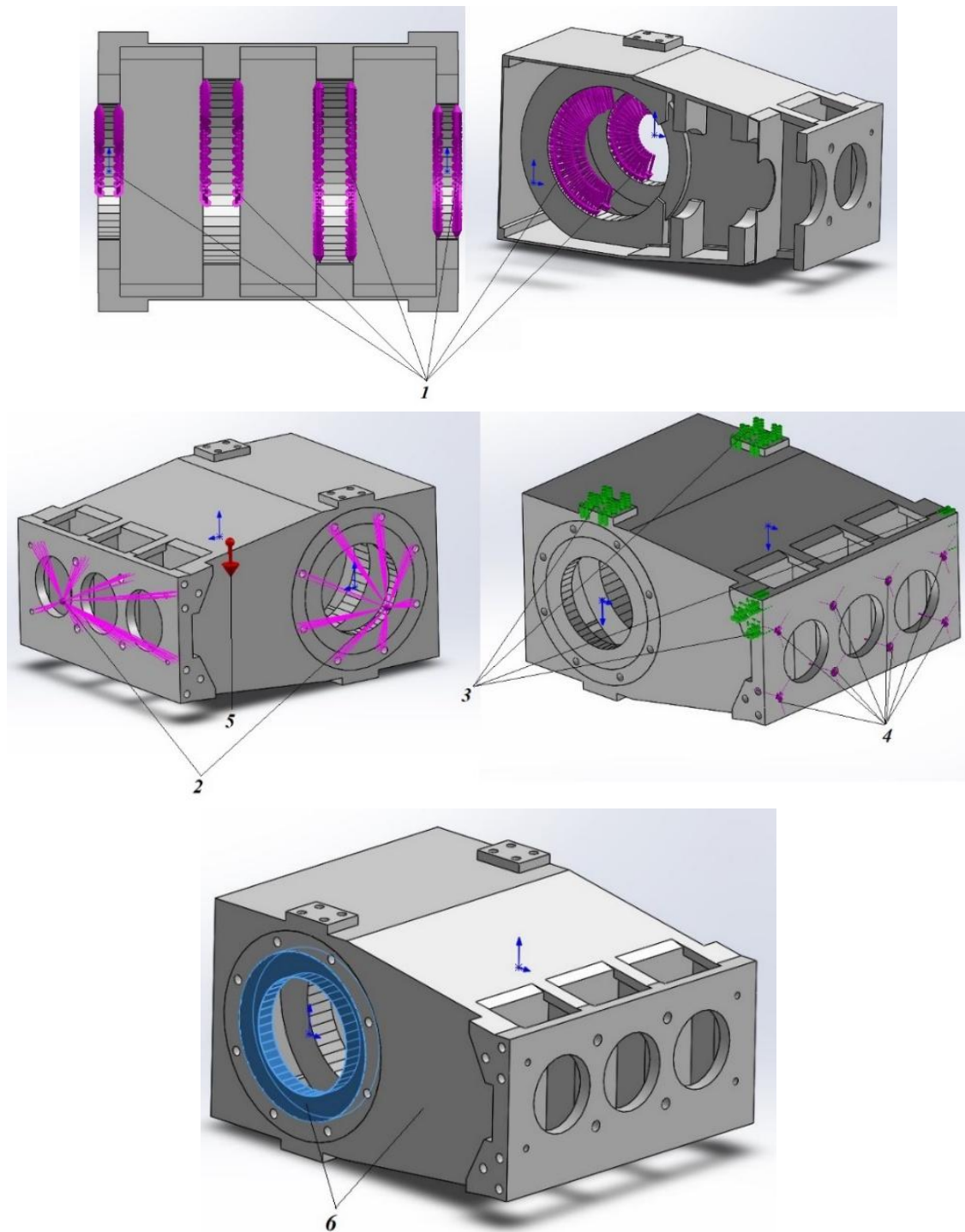


Fig. 5. Boundary conditions: 1 — operating load (radial force distributed over cylindrical surfaces); 2 — remote loading (mass of the gearbox and hydraulic unit); 3 — restriction — “fixed”, zero movements in all axes — X , Y , Z ; 4 — operating load (pressure force of the liquid under discharge and suction); 5 — gravity; 6 — type of contact — connected (no gap) surfaces with shared nodes

Research Results. Diagrams of equivalent von Mises stresses are shown in Fig. 6.

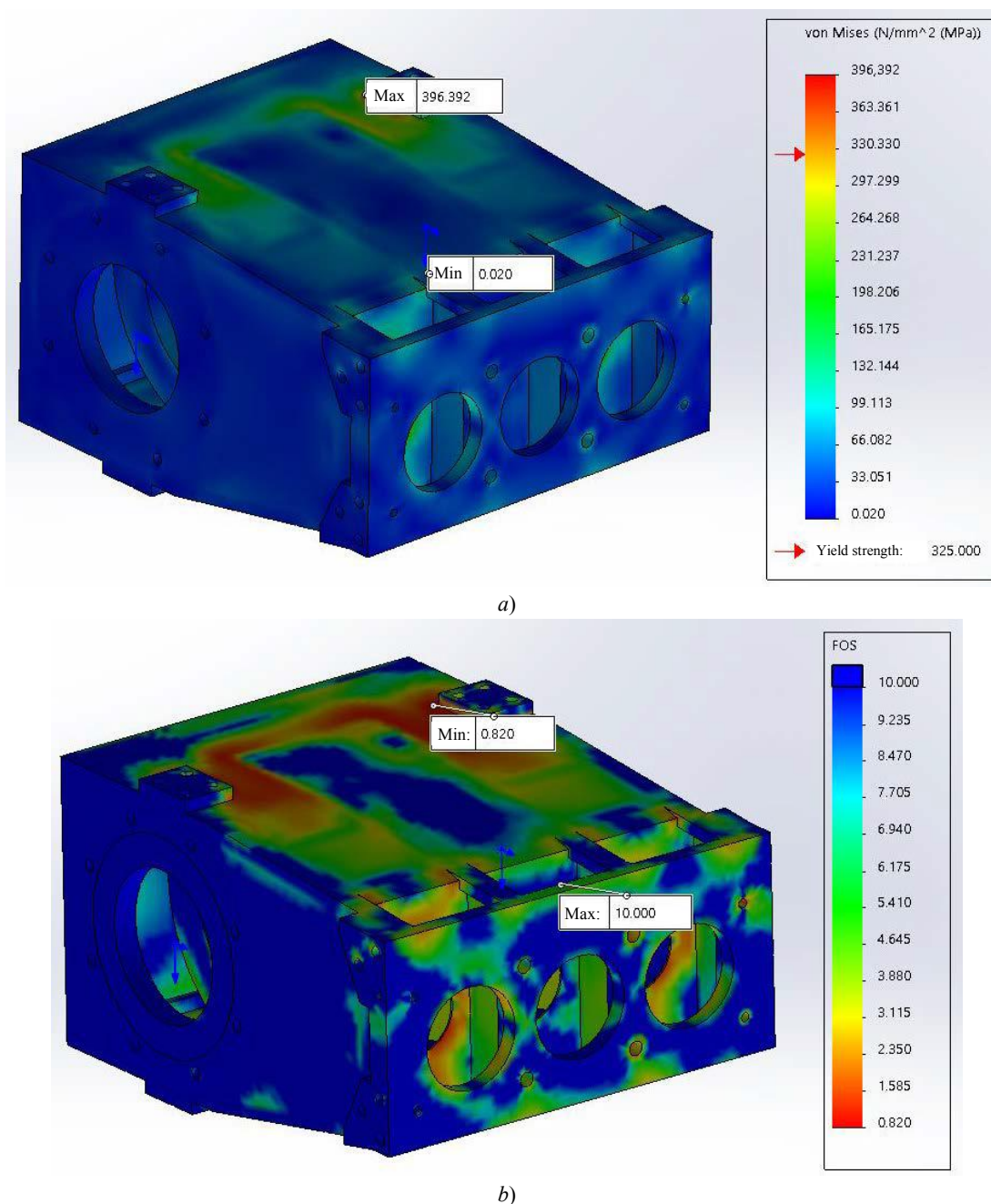


Fig. 6. Diagrams obtained as a result of the strength analysis of the TWS 600 plunger pump body: *a)* diagram of equivalent stresses, *b)* diagram of the yield factor

Yield factor is determined from the formula:

$$K_n = \frac{\sigma_B}{\sigma_{\text{эKB}}},$$

where σ_B — ultimate strength of 09G2S steel, $\sigma_B = 470 \text{ Mpa}^1$; $\sigma_{\text{эKB}}$ — maximum equivalent stress, $\sigma_{\text{эKB}} = 396.392 \text{ MPa}$.

$$K_n = \frac{470}{396.392} = 1.18.$$

As can be seen, the equivalent stresses² have the greatest intensity in the lower region of the pump body design.

The minimum yield factor of the material is 0.82 (see Fig. 6 *b*).

¹ Zubchenko AS, Koloskov MM, Kashirsky YV, et al. Steel and Alloy Grade Guide. Moscow, 2003. 784 p. (In Russ.)

² Feshchenko VN. Constructor reference. Book 2. Design of machines and their parts. Moscow, 2017. 400 p. (In Russ.)

The strength calculation of the plunger pump body was carried out for the third position of the mechanism (Fig. 2 b). For other positions of the mechanism (see Fig. 2 a, b) the strength calculation is performed similarly.

The results of the strength calculation of the body for the three positions of the mechanism are shown in Table 3.

Table 3

Results of the strength calculation of the plunger pump body

Mechanism position	Plunger position			Equivalent stresses, MPa	Safety factor for	
					yield strength	ultimate strength
I	1	2	3	231.772	1.402	2.02
	ex.p.	suction	discharge			
II	1	2	3	284.783	1.141	1.65
	discharge	ex.p.	suction			
III	1	2	3	396.392	0.820	1.18
	suction	discharge	ex.p.			

Discussion and Conclusions. The reactions in the crankshaft supports with account for the forces generated by the plunger depending on its operating mode and the position of the crank are described. The forces acting on each of the plungers and the resulting reactions in each of the supports are determined.

For the strength calculation of the plunger pump body made of 09G2S steel, the FEM in CAD SolidWorks Simulation is used. When assessing the body strength, it has been observed that in the third position of the mechanism, the lower region of the structure has minimum coefficients of yield factor and strength factor (see Table 3). This area requires strengthening since the coefficient values are insufficient for the specified operating conditions. Also, there are unloaded areas in the body, where the values of safety and yield factors are several times higher than the recommended ones. In the future, it is required to optimize the plunger pump body: to strengthen the areas of the structure with unsatisfactory coefficients of safety and yield factors, and in places where the coefficients exceed the recommended values, to use a metal of a smaller thickness.

Thus, the strength calculation results can be used to optimize the design of the pump body under standard operating conditions.

References

1. Vlasov VS. High pressure pump stations and their application fields. Russian Journal of Heavy Machinery. 1998;7:53–55.
2. Popov VP, Kireev SO. Trekhplunzhernye nasosy vysokogo davleniya «Trast-Inzhiniring» [Three-plunger high-pressure pumps “Trust-Engineering”]. Toplivnyi rynek. Oil. Gas. 2010;21:6–9. (In Russ.)
3. Stepanov V, Kireev S, Korchagina M, et al. Fatigue performance of hydraulic unit of high-pressure plunger pump. IOP Conference Series: Earth and Environmental Science. 2019;403:012087. URL: <https://iopscience.iop.org/article/10.1088/1755-1315/403/1/012087> (accessed: 09.02.21) DOI: 10.1088/1755-1315/403/1/012087
4. Veselovskaya EV, Papin VV, Bezuglov RV. Perfection of Drinking and Technical Water Supply Systems in the Implementation of the Concept a Heat and Power Complex for Highly Efficient Use of Secondary and Renewable Energy Sources. IOP Conference Series: Materials Science and Engineering. 2018;463(2):022011. URL: <https://iopscience.iop.org/article/10.1088/1757-899X/463/2/022011> (accessed: 09.02.21) DOI: 10.1088/1757-899X/463/2/022011
5. Parshukov VI, Efimov NN, Papin VV, et al. Energy-Technological Complex, Functioning on The Basis of Waste Processing Technologies. IOP Conference Series: Materials Science and Engineering. 2018;463:042029. URL:

<https://iopscience.iop.org/article/10.1088/1757-899X/463/4/042029> (accessed: 09.02.21) DOI: 10.1088/1757-899X/463/4/042029

6. Babichev S. Inzhenernyi analiz sredstvami T-FLEX [Engineering analysis by means of T-FLEX]. SAPR i Grafika = CAD and Graphics. 2016;12(242):36–41. (In Russ.)
7. Kireev SO, Korchagina MV, Nikishenko SL, et al. Raschet rabochikh kharakteristik uzla treniya «polzun — napravlyayushchie» plunzhernogo nasosa vysokogo davleniya [Calculation of working characteristics of the “slider-guides” friction unit of a high-pressure plunger pump]. University News. North-Caucasian region. Technical Sciences Series. 2018;3(199):101–106. DOI: 10.17213/0321-2653-2018-3-101-106 (In Russ.)
8. Chakherlou TN, Mirzajanzadeh M, Abazadeh B, et al. An investigation about interference fit effect on improving fatigue life of a holed single plate in joints. European Journal of Mechanics. 2010;29(4):675–682. DOI: 10.1016/j.euromechsol.2009.12.009
9. Makhutov NA. Deformatsionnye kriterii razrusheniya i raschet ehlementov konstruksii na prochnost' [Deformation criteria for fracture and strength analysis of structural elements]. Moscow: Mashinostroenie; 1981. 272 p. (In Russ.)
10. Kireev SO. Analiz uslovii raboty uzlov treniya skol'zheniya privodnoi chasti plunzhernykh nasosov vysokogo davleniya servisa neftegazovykh skvazhin [Analysis of the operating conditions of the sliding friction units of the drive part of high-pressure plunger pumps for oil and gas wells]. Khimicheskoe i Neftegazovoe Mashinostroenie = Chemical and Petroleum Engineering. 2016;5:25–30. (In Russ.)
11. Kireev SO, Kaderov HK, Zaikin VP. Avtomatizirovannoe postroenie diagramm kinematicheskikh parametrov shatunno-kreitskopfnogo mekhanizma [Automated construction of diagrams of the kinematic parameters of the connecting rod-crosshead mechanism]. Progressive Technologies and Systems of Mechanical Engineering. 2018;3(62):41–46. (In Russ.)
12. Timofeev GA, Mor EG, Barbashov NN. Sovmestnyi metod kinematicheskogo i silovogo analiza slozhnykh mekhanicheskikh sistem [A combined method for the kinematic and force analysis of complex mechanical systems]. Proceedings of Higher Educational Institutions. Machine Building. 2015;3(660):11–17. (In Russ.)
13. Sidorenko AS, Potapov AI. Matematicheskaya model' kinetostaticheskogo rascheta ploskikh rykhaznykh mekhanizmov [Mathematical model of kinetostatic calculation of flat lever mechanisms]. Proceedings of the Voronezh State University of Engineering Technologies. 2016;1(67):70–78. (In Russ.)

Submitted 24.12.2020

Scheduled in the issue 08.02.2021

About the Authors:

Koleda, Eduard V., graduate student of the Oil and Gas Complex Machinery and Equipment Department, Don State Technical University (1, Gagarin sq., Rostov-on-Don, 344003, RF), ORCID: <http://orcid.org/0000-0001-6955-6873>, koleda.eduard@mail.ru.

Kireev, Sergey O., Head of the Oil and Gas Complex Machinery and Equipment Department, Don State Technical University (1, Gagarin sq., Rostov-on-Don, 344003, RF), Dr.Sci. (Eng.), professor, ORCID: <http://orcid.org/0000-0001-9352-3852>, kireevso@yandex.ru.

Korchagina, Marina V., associate professor of the Oil and Gas Complex Machinery and Equipment Department, Don State Technical University (1, Gagarin sq., Rostov-on-Don, 344003, RF), Cand.Sci. (Eng.), ORCID: <http://orcid.org/0000-0001-7092-7176>, ms.korchaginamv@mail.ru.

Efimov, Andrey V., associate professor of the Oil and Gas Complex Machinery and Equipment Department, Don State Technical University (1, Gagarin sq., Rostov-on-Don, 344003, RF), Cand.Sci. (Eng.), ORCID: <https://orcid.org/0000-0001-9940-9030>, spu-58.2@donstu.ru.

Joerg Sperling, Managing Director, ACT Well Services GmbH, (Am Klingbusch 6, Diesdorf, 29413, Germany), spu-58.2@donstu.ru.

Claimed contributorship

E. V. Koleda: computational analysis; text preparation; formulation of conclusions. S. O. Kireev: academic advising; basic concept formulation; research objectives and tasks. M. V. Korchagina: analysis of the research results; the text revision; correction of the conclusions. A. V. Efimov: supervising the model construction; monitoring the implementation of numerical studies. Joerg Sperling: statement of the research problem; scientific advice.

All authors have read and approved the final manuscript.

MACHINE BUILDING AND MACHINE SCIENCE



DOI 621.855

<https://doi.org/10.23947/2687-1653-2021-21-1-82-88>

Power analysis of chain transmission with gear chain and involute sprockets



S. B. Berezhnoy, G. V. Kurapov

Kuban State Technological University (Krasnodar, Russian Federation)

Introduction. The power analysis of a chain transmission with a toothed chain and involute sprockets considers the centrifugal forces and the friction coefficients between the plate and the sprocket tooth. The work objectives are to determine all meshing forces, and to calculate the coupling coefficient of the gear chain with the involute sprocket in the drive gears.

Materials and Methods. When evaluating the traction capacity of a chain transmission, such parameters as the power analysis and the coupling coefficient of the gear chain with the sprocket are important (it shows what fold the pressure on a given tooth is greater than the pressure perceived by the tooth in front). In the presented paper, the following diagrams are visualized: the arrangement of the plates in gearing with the involute sprocket teeth and the meshing forces. The factors that affect the involute profile of the sprocket tooth are considered. This includes the weight of the chain plate package and the force: centrifugal, friction, normal pressure and tension. At the same time, changes in the coupling coefficient for the subsequent teeth involved in traction are taken into account. The balance of the links i and $i + 1$ of the gear chain is studied in the coordinate system XOY with the center on the axis of rotation of the involute sprocket. The method enables to determine all the desired forces through the geometric calculation of the values of the angular transmission parameters. Using the equations obtained, the following parameters are specified: the coupling coefficient B_i , the tension of the driving branch S_1 and the slack branch S_2 .

Results. A patented transmission stand with a gear chain and involute sprockets is presented. The tests carried out on it validated the study results of a chain transmission with a toothed gear and involute sprockets with the specified parameters. The correctness of the power analysis of the transmission with account for the centrifugal forces and the friction coefficients of the plates and the sprocket teeth was proved.

Discussion and Conclusions. It is noted that the centrifugal forces and the friction coefficients during engagement affect significantly the traction capacity of a transmission with a toothed chain and involute sprockets. The data obtained can be used to accurately estimate the traction capacity of such gears.

Keywords: chain transmission, toothed chain, involute sprocket, chain plate, traction capacity, coupling coefficients, centrifugal forces, friction forces, friction coefficients, joint angular velocity, driving side, slack side.

For citation: S. B. Berezhnoy, G. V. Kurapov. Power analysis of chain transmission with gear chain and involute sprockets. Advanced Engineering Research, 2021, vol. 21, no. 1, p. 82–88. <https://doi.org/10.23947/2687-1653-2021-21-1-82-88>

© Berezhnoy S. B., Kurapov G. V., 2021



Introduction. Chain transmissions with toothed chain are not sufficiently studied. Their release is limited, but they are increasingly used in production. Specifically, such gears are used to complete drive mechanisms in machines, precision machine tools, and other equipment. This paper considers the power analysis and calculation of the traction capacity of gears with a toothed chain and involute sprockets.

The traction capacity determines the operability of the involute gear chain transmission, which depends on a number of factors¹. Among them there are:

¹ Kurapov GV. Performance study of a chain transmission with a gear chain and involute sprockets: Cand.Sci. (Eng.) diss. Krasnodar, 2019. 173 p. (In Russ.)

- transmission geometry,
- limiting contact stress of the weakest element of the pair “chain plate – sprocket tooth”,
- coupling coefficient of the toothed chain with the sprocket teeth,
- slipping of the toothed chain along the sprocket teeth,
- permissible specific pressure inside the joint,
- impact resistance of gear chain elements¹ [1-3].

Materials and Methods. The coupling coefficient is one of the main factors of the traction capacity of a chain transmission equipped with a toothed chain. During the operation of such a transmission, engagement occurs and forces act that move the chain plates along the working and occipital profiles of the sprocket teeth [4-7]. On the arc of the involute sprocket with a toothed chain, any of its links (link i , $i + 1$, $i + 2$, etc.) experience:

- friction force $N_i f$ of the chain on the sprocket tooth,
- tensile strength Q_i of adjacent links,
- normal pressure force N_i of the tooth sprocket profile (Fig. 1).

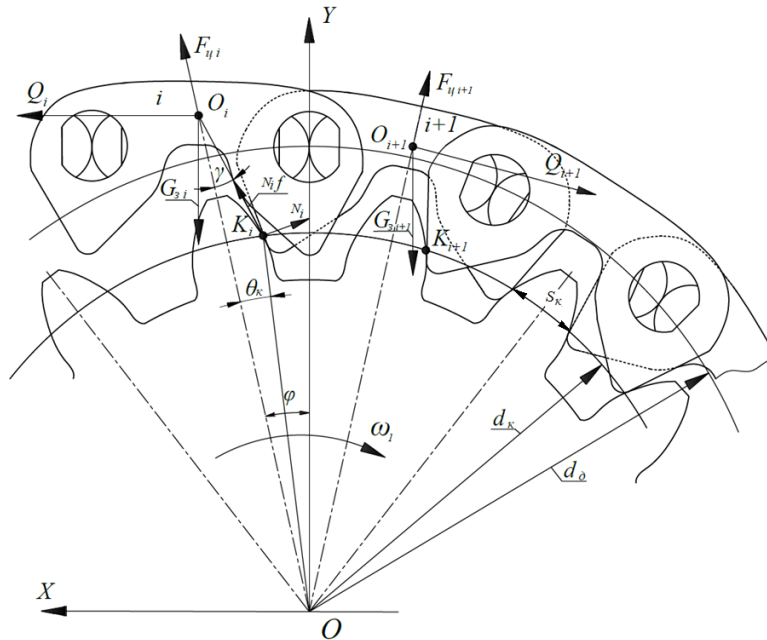


Fig. 1. Arrangement of plates in engagement with the involute sprocket teeth

In the literature, the coupling coefficient is calculated from the ratio of the tensile forces Q_i and Q_{i+1} in the adjacent chain links:

$$B_i = \frac{Q_i}{Q_{i+1}}. \quad (1)$$

This coefficient is not constant, so the plates of the gear chain move along the profiles of the sprocket teeth throughout the entire arc of contact. Fig. 2 shows the engagement of the first package of plates (link) of the chain with the sprocket tooth.

¹ Semenov VS. Availability assurance of roller chain drives during their operation. In: Proc. All-Russian Sci.-Pract. Conf. of postgraduates, doctoral students, and young scientists. Maykop, 2017. P. 121–125. (In Russ.)

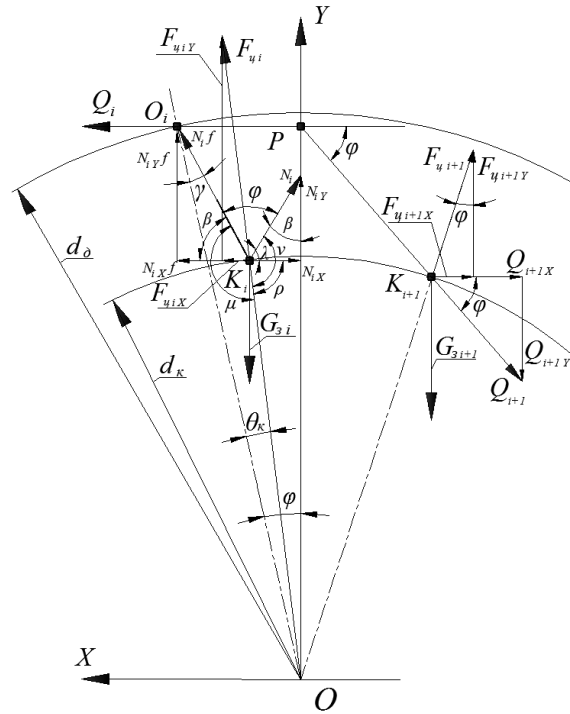


Fig. 2. Diagram of the forces acting in the engagement of the gear chain plate with the sprocket

The involute profile of the sprocket tooth is affected by the following factors [8-14].

1. Friction force $N_i f$, which prevents the movement of the plate pack to the top of the sprocket tooth. Here, f — the friction coefficient.
2. Weight of the chain plate package $G_z = m_i g$. Here, g — the acceleration of gravity, m_i — chain link weight depending on the pitch¹.
3. Normal pressure force N_i of the sprocket tooth profile concentrated at the point of engagement K_i .
4. Tensile forces Q_i and Q_{i+1} of the adjacent links of the gear chain.
5. Centrifugal force with account for the mass of the chain link $F_y = \frac{m_i \omega^2}{R}$. Here, ω — angular speed of rotation of the sprocket. R — radius of the central part of the link (represented as a circle that changes position when the sprocket rotates) on the involute profile of the sprocket tooth.

However, when the chain moves from the driving branch to the driven branch, the tensile forces Q_i and Q_{i+1} change by the value of each value of the coupling coefficient B_i ; so, it needs to be determined more precisely.

Let us build the XOY coordinate system. It passes through the center of the axis of rotation of the involute sprocket. The vector of the X -axis coincides with the vector of the linear velocity of the gear chain in the transmission.

Let us analyze the equilibrium of the first link i and the second $i + 1$.

Balance of forces on the axis X ($\sum X = 0$) will be:

$$-Q_i + N_{iX} - N_{iX} f - F_{yiX} + F_{y(i+1)X} + Q_{i+1X} = 0. \quad (2)$$

Balance of forces on the axis Y ($\sum Y = 0$) will be:

$$G_{zi} + G_{z(i+1)} - F_{yiY} - N_{iY} - N_{iY} f + Q_{i+1Y} - F_{y(i+1)Y} = 0. \quad (3)$$

At $\sum X = 0$ and $\sum Y = 0$, the gear chain plates will be stationary. If $\sum X = 0$ and $\sum Y \neq 0$, then the plates will move along the tooth profile.

¹ GOST 13552–81. USSR State Standard. Driving toothed chains. Specifications. USSR State Standards Committee. Moscow: Standartinform; 1987. 12 p. (In Russ.)

Let us determine the forces acting on the chain links. Fig. 2 shows: P — the center of mass of the gear chain link; d_k — the diameter of the circle of the contact point K of the package of plates with the profile of the sprocket tooth, $d_k = \frac{d_b}{\cos \theta}$; d_o — the diameter of the dividing circle of the sprocket, $d_o = \frac{t}{\sin \frac{180}{z}}$.

Along X -axis:

$$N_{iX} = N_i \cdot \sin \beta,$$

$$N_{iX} f = N_i f \cdot \cos \beta,$$

$$F_{yiX} = F_{yi} \cdot \sin \varphi,$$

$$F_{yi+1X} = F_{yi+1} \cdot \sin \varphi,$$

$$Q_{i+1X} = Q_{i+1} \cdot \cos \varphi,$$

Along Y -axis:

$$N_{iY} = N_i \cdot \cos \beta,$$

$$N_{iY} f = N_i f \cdot \sin \beta,$$

$$F_{yiY} = F_{yi} \cdot \cos \varphi,$$

$$F_{yi+1Y} = F_{yi+1} \cdot \cos \varphi,$$

$$Q_{i+1Y} = Q_{i+1} \cdot \sin \varphi.$$

Here, β — the angle of the tooth profile of the involute sprocket; $\varphi = \frac{\pi}{z}$ — half of the tooth pitch angle of the involute sprocket.

Values of angular parameters:

$$\lambda = \varphi + \gamma, \quad (4)$$

$$\mu = \pi - \gamma - \theta_k, \quad (5)$$

$$\nu = \frac{\pi}{2} + \gamma + \theta_k, \quad (6)$$

$$\rho = \frac{\pi}{2} - \varphi + \theta_k, \quad (7)$$

$$\beta = \frac{\pi}{2} - \varphi - \gamma. \quad (8)$$

Here, γ — half of the tooth wedge angle of the involute sprocket.

$$\gamma = \alpha_k - \theta_k. \quad (9)$$

$$\alpha_k = \arccos \frac{d_b}{d_k}. \quad (10)$$

θ_k — the angle between the axis OO_{i+1} of the tooth and the line connecting point K_1 to the center O of the sprocket (see Fig. 2).

$$\theta_k = \frac{S_k}{d_k}. \quad (11)$$

S_k — the thickness of the involute sprocket tooth at the point of contact K and the gear chain (see Fig. 1). $d_b = m z \cos \alpha$ — the diameter of the main circle of the involute sprocket, where m — the sprocket module for the toothed chain transmission, z — the number of sprocket teeth.

Substituting all the values included in the equations (2) and (3), we obtain:

$$2G_z - F_{yi} \cdot \cos \varphi - N_i f \cdot \sin \beta - N_i \cdot \cos \beta + Q_{i+1} \cdot \sin \varphi - F_{yi+1} \cdot \cos \varphi = 0, \quad (12)$$

$$Q_{i+1} = \frac{(F_{yi} \cdot \cos \varphi + N_i \cdot \cos \beta + N_i f \cdot \sin \beta + F_{yi+1} \cdot \cos \varphi - 2G_z)}{\sin \varphi}, \quad (13)$$

$$Q_i = N_i \cdot \cos \beta - N_i f \cdot \cos \beta - F_{yi} \cdot \sin \varphi + F_{yi+1} \cdot \sin \varphi + Q_{i+1} \cdot \cos \varphi = 0. \quad (14)$$

Transforming the equations (13) and (14), we obtain the coupling coefficient B_i of the toothed chain with a given involute sprocket tooth:

$$B_i = \frac{Q_i}{Q_{i+1}} = \sin \varphi \left(\frac{N_i \cdot \cos \beta - N_i f \cdot \cos \beta - F_{yi} \cdot \sin \varphi + F_{yi+1} \cdot \sin \varphi + Q_{i+1} \cdot \cos \varphi}{F_{yi} \cdot \cos \varphi + N_i \cdot \cos \beta + N_i f \cdot \sin \beta + F_{yi+1} \cdot \cos \varphi - 2G_s} \right). \quad (15)$$

If the tension value of the driving branch of the chain transmission S_1 is known, then the tension of the driven branch S_2 is determined with account for the overall coefficient of the chain – sprocket tooth coupling:

$$B_z = \frac{S_1}{S_2}, \quad (16)$$

$$S_2 = \frac{S_1}{B_z}, \quad (17)$$

$$B_z = B_0 \cdot B_1 \cdot B_2 \dots B_n. \quad (18)$$

Here, B_z — the overall coupling coefficient of the chain and the sprocket; n — the number of teeth of the driving involute sprocket.

Research Results. To verify the calculations, a stand¹ protected by a patent of the Russian Federation was designed and manufactured (Fig. 3). Bench tests of the chain transmission under study were carried out. The parameters:

- 1) electric motor power $N_{эл} = 12$ kW,
- 2) toothed chain pitch $t_y = 19.05$ mm,
- 3) the number of teeth of the driving and driven sprocket $z_1 = z_2 = 23$,
- 4) speed of the driving and driven sprocket $n_1 = n_2 = 1000$ rpm.

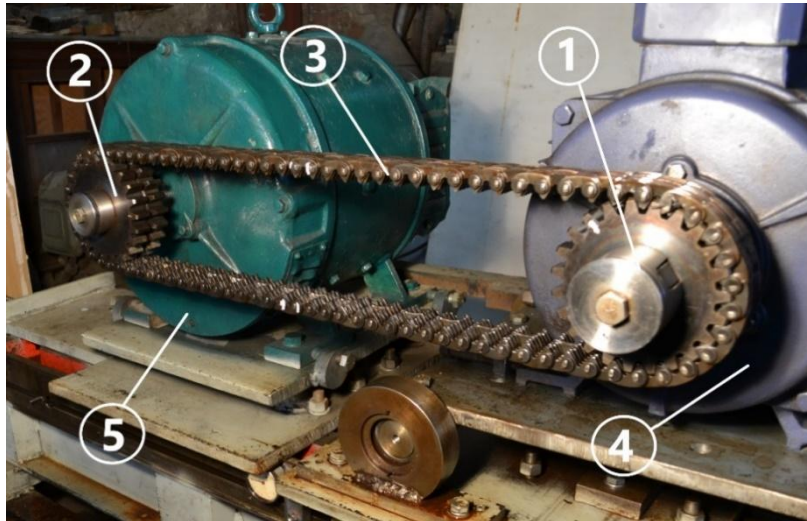


Fig. 3. Transmission test bench with toothed chain and involute sprockets:

1 — driving sprocket, 2 — driven sprocket, 3 — toothed chain, 4 — electric motor, 5 — generator

For the bench tests, calculations were performed with account for the reference data^{2, 3, 4, 5}. The results are presented in Table 1.

¹ Berezhnoy SS, et al. Test bench for chain gears. RF Patent no. 147242, 2014. (In Russ.)

² Chernavsky SA, et al. Design of mechanical gears: study guide for technical colleges. Moscow: Al'yans; 2008. 590 p. (In Russ.).

³ Uchaev PN, et al. Course design of machine parts based on graphic systems: study guide. Krasnodar: Izd-vo TNT; 2013. 428 p. (In Russ.)

⁴ Gotovtsev AA, Kotenok IP. Design of chain gears. Reference guide. Moscow: Mashinostroenie; 1982. 336 p. (In Russ.)

⁵ Feshchenko VN. Handbook for designers. Book 1. Machines and mechanisms. Moscow: Infra-Inzheneriya; 2016. 400 p. (In Russ.)

Table 1

The obtained data for determining the traction capacity of a toothed chain transmission

Parameter	Notation and dimension	Numerical value
Tension of the working transmission branch	S_1 , H	4662
Tension of the idle transmission branch	S_2 , H	270
Total coupling coefficient of the chain and the leading involute sprocket	B_1	17.2
Centrifugal force of the chain	F_u , H	29.82

The proposed approach to determining the coupling coefficient has confirmed the correctness of the force calculation with account for the centrifugal forces and the friction coefficients of the plate package and the sprocket tooth.

Discussion and Conclusions. In this paper, all the forces acting in the engagement of the chain plate package and the sprocket tooth are determined. The procedure of power calculation of a toothed chain transmission is presented. The dependences for determining the impact of centrifugal forces and friction coefficients on the final calculation of the coupling coefficient are obtained. To confirm the theory, the chain transmission was studied on a test bench.

So, the centrifugal forces and the meshing friction coefficients significantly affect the traction capacity of the transmission with a toothed chain and involute sprockets.

References

1. Semenov VS, Saenko NN. Formy raspolozheniya sharnirov tsepi i tyagovaya sposobnost' tsepoi peredachi [Forms of arrangement of chain hinges and traction ability of chain transmission]. University news. North-Caucasian region. Technical Sciences Series. 2003;5:106–108. (In Russ.)
2. Semenov VS, Saenko NN. Sootnoshenie usilii v tsepnom zatseplenii [Ratio of forces in the chain engagement]. University news. North-Caucasian region. Technical Sciences Series. 2003;5:108–11. (In Russ.)
3. Metil'kov SA, Bachalov IS. Метильков, С. А. Otsenka rabotosposobnogo sostoyaniya tsepnykh peredach [Assessment of the working condition of chain gears]. Novye materialy i tekhnologii v mashinostroenii. 2009;10:59–62. (In Russ.)
4. Berezhnoy SB, Voyna AA, Kurapov GV. Opredelenie radiusov raspolozheniya tsentrov sharnirov zubchatoi tsepi na dugakh obkhvata ehvol'ventnykh zvezdochek [Determining location radii of gear chain pivot locus on involute sprocket wraps]. Vestnik of DSTU. 2014;1(76):86–92. DOI: <https://doi.org/10.12737/3507> (In Russ.)
5. Ostapenko OI, Voina AA, Lichman LR. Kinematicheskaya dolgovechnost' tsepoi peredachi s zubchatoi tsep'yu i ehvol'ventnoi zvezdochkoj [Kinematic durability of chain transfer with the tooth chain and the involute sprockets]. Vestnik of DSTU. 2009;4(43):653–658. (In Russ.)
6. Berezhnoy SB, Voyna AA, Kurapov GV. Analiz udarnoi stoikosti tsepi v zavisimosti ot profilya zuba zvezdochki [Analysis of impact resistance of chain according to sprocket lug profile]. Scientific Journal of KubSAU. 2015;03(107):1522–1532. URL: <http://ej.kubagro.ru/2015/03/pdf/98.pdf> (accessed: 27.01.2021). (In Russ.)
7. Semenov VS, Muzalev SA. Nityazhenie vetvei kontura tsepoi peredachi i koefitsient stsepleniya zvezdochki [Tension of the branches of the chain transmission circuit and the coupling coefficient of the sprocket]. New Technologies. 2006;2:79–82. (In Russ.)
8. Metil'kov SA. Метильков, С. А. Prognozirovaniye nagruzochnoi sposobnosti tsepnykh peredach pri periodicheskom smazyvanii [Predicting the load capacity of chain gears under periodic lubrication]. Vestnik Mashinostroeniya. 2002;10:9–12. (In Russ.)
9. Kryvyi PD, Liashuk OL. Metody opredeleniya nesushchei sposobnosti privodnykh rolikovykh i tyagovykh plastinchatykh tsepei [Methods for determining the carrying capacity of the drive roller and traction plate chains]. Technological Complexes. 2013;2(8):39–51. (In Russ.)

10. Ryabov GK. Raspredelenie nagruzki po zub'yam zvezdochek tsepnykh peredach [Load distribution on the teeth of sprockets of chain gears]. Proceedings of Higher Educational Institutions. Machine Building. 1983;3:22–27. (In Russ.)
11. Berezhnoy SB, Voyna AA, Kurapov GV. Osobennosti rascheta i proektirovaniya zubchatykh tsepnykh peredach [Features of calculation and design of tooth chain gearings]. Science. Engineering. Technology. 2014;3:68–75. (In Russ.)
12. Szezepinski W. Limit analysis and plastic design of complex shape. Progress in Aerospace Sciences. 1972;12:1–47. DOI:10.1016/0376-0421(72)90003-6
13. Rachner HG. Stahlgelenketten und Kettentriebe. Berlin: Springer;1962. 220 p.
14. Kuntzmann P. Les transmission par chaîne à rouleaux. Paris: Dunod; 1961. 220 p.

Submitted 12.01.2021

Scheduled in the issue 25.01.2021

About the Authors:

Berezhnoy, Sergey B., professor of the Land Transport and Mechanics Department, Kuban State Technological University, (2, Moskovskaya St., Krasnodar, 350072, RF), Academician of the Engineering Academy of the Russian Federation, Dr.Sci. (Eng.), professor, Scopus ID: [25227504200](https://scopus.org/scopus/authors/details/scopusid/25227504200), ORCID: <https://orcid.org/0000-0001-5013-7345>, berezhnoy@kubstu.ru

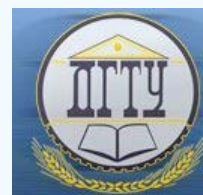
Kurapov, Georgy V., associate professor of the of the Land Transport and Mechanics Department, Kuban State Technological University, (2, Moskovskaya St., Krasnodar, 350072, RF), Cand.Sci. (Eng.), ResearcherID: [AAO-8482-2020](https://orcid.org/0000-0001-8101-265X), Scopus ID: [57219551108](https://scopus.org/scopus/authors/details/scopusid/57219551108), ORCID: <https://orcid.org/0000-0001-8101-265X>, kurapov_georgii@mail.ru

Claimed contributorship

S. B. Berezhnoy: academic advising; the research results analysis of the power transmission calculation with account for new variables; formulation of conclusions. G. V. Kurapov: performing calculations according to the proposed method; conducting experiments on the test bench; processing of the results; creating the final version of the text.

All authors have read and approved the final manuscript.

MACHINE BUILDING AND MACHINE SCIENCE



UDC 621.791.793:669.15–194.2:539.4

<https://doi.org/10.23947/2687-1653-2021-21-1-89-95>

On detection of crack-like welding defects by existing quality control methods

V. A. Peredelsky¹, V. Y. Harchenko¹, A. L. Chernogorov¹, S. V. Tihinov²¹Don State Technical University (Rostov-on-Don, Russian Federation)²“GAC MR NAKS” LLC (Moscow, Russian Federation)

Introduction. The research materials devoted to the operability assurance of welded structures of hazardous technical devices — components of oil and gas production equipment are summarized. The factors determining the operational strength of welded joints and structures are systematized and diagrammed. The causes for the decrease in their service properties are described. We have defined the role of volumetric and crack-like welding defects, which were not detected during quality control at the manufacturing stage and in determining the residual life while in operation, in ensuring the life cycle of the structure. Measures to improve the practice of detecting crack-like defects under visual- and-dimensional and ultrasonic methods of quality control of welded joints are proposed.

Materials and Methods. In accordance with SNiP 2.05.06–85, the structures of main oil and gas pipelines, vertical cylindrical tanks, and other oil and gas production equipment (OGPE) are made of dead-killed and semikilled low-carbon and low-alloy steels with tensile strength of up to 686.5 MPa. Regardless of the class and strength level of steel, it should be well welded by all methods prescribed by standard process documentation (SPD). At the same time, regardless of the state of supply, the carbon equivalent $C_{\text{ЭКВ}}$ should not exceed 0.46 %. The research methods are calculation-experimental ones. To calculate the stress-strain state of welded joints, the following methods were used:

- finite elements (FEM),
- fracture mechanics using the stress intensity coefficient K_I .

Methods of mathematical statistics were used to estimate the geometric dimensions of crack-like welding defects. Welding defects were detected by standard quality control methods prescribed by the SPD and GOST standards.

Results. Welded structures operating in the fatigue mode are considered. Some factors characteristic of welded joints are analyzed. It is shown how they affect the formation of strength performance properties. The role of dangerous crack-like defects, which with high probability can be formed in welded joints in the manufacture of structures and during operation, is established. Often, the reason is a decrease in mechanical properties due to aging and loss of plasticity caused by accidental mechanical actions. Note that it is impossible to identify these defects by existing quality control methods, both during the control process under production and during diagnostics while in operation. This reduces the accuracy of predicting the operational life of the welded structure.

Discussion and Conclusion. It is proposed to include the following requirements in the SPD:

- to the quality of welded joints of hazardous technical devices of OGPE,
- to detection of sharp crack-like defects with a radius of curvature in the range of 0.1–0.25 mm.

However, the reliability of detection of such defects by the control methods used remains low due to the human factor. To increase the reliability of detection of sharp crack-like defects, the directions of improvement of ultrasonic quality control of welded joints are determined.

Keywords: welding, welds, structural strength, welding defects, non-destructive testing, visual and dimensional control, ultrasonic testing, validity.

For citation: V. A. Peredelsky, V. Y. Harchenko, A. L. Chernogorov, et al. On detection of crack-like welding defects by existing quality control methods. Advanced Engineering Research, 2021, vol. 21, no. 1, p. 89–95. <https://doi.org/10.23947/2687-1653-2021-21-1-89-95>

© Peredelsky V. A., Harchenko V. Y., Chernogorov A. L., Tihonov S. V., 2021



Introduction. Scientific studies [1-7], as well as standards¹, regulatory² and specification documents³ of relevant organizations are devoted to the problems of determining the strength of the operated welded metal structures. Factors that determine the strength characteristics of weld joints are numerous and diverse. The destruction of welded metal structures under operation depends on:

- operating conditions (level of calculated loads, loading scheme, joint effect of various forces, action of unaccounted loads, etc.);
- structural and technological causes.

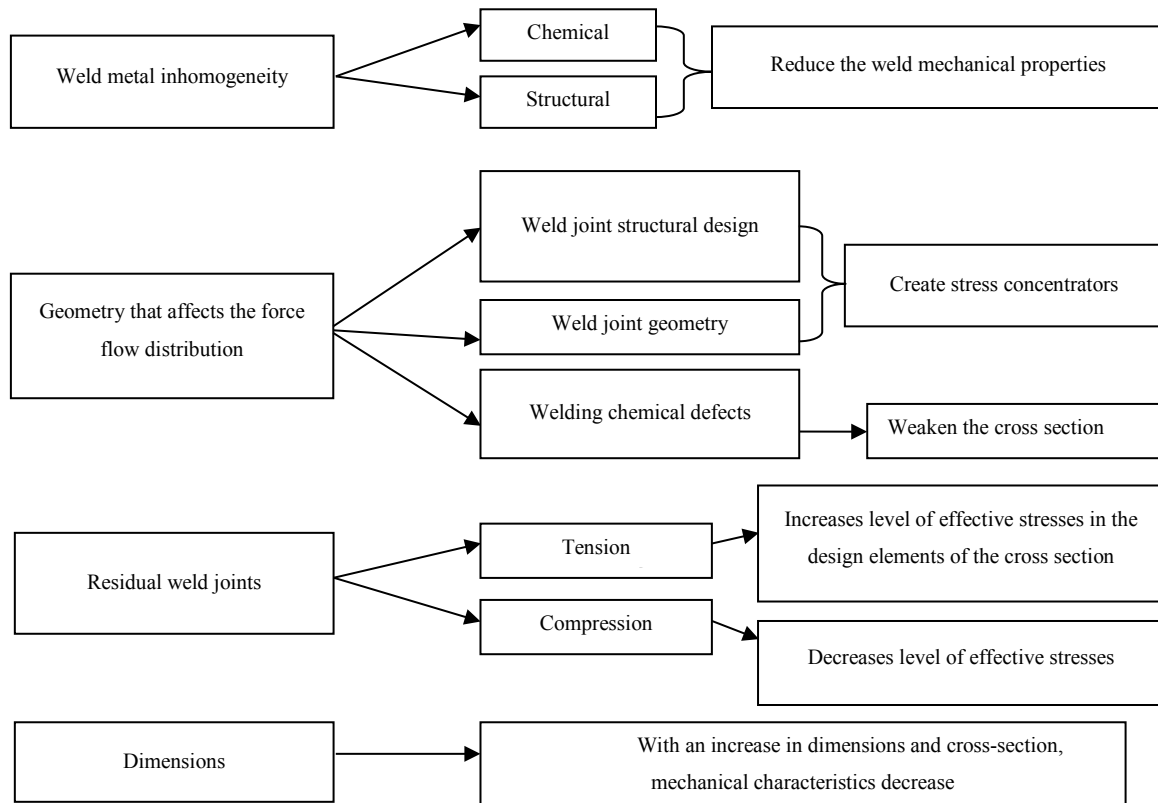


Fig. 1. Factors determining the operational strength of weld joints and structures

The generalization of numerous studies suggests that the load-bearing capacity of welded structures is affected by the following conditions.

- I. Heterogeneity of the metal structure and mechanical properties of the weld and the near-weld zone.
- II. Welding defects, mainly, crack-like ones. These are undercuts, cracks, rolls, sharp inclusions, faulty penetration, incomplete fusion, etc. (Fig. 2).

¹ Gas-shielded arc welding. Welded joints. Main types, design elements and dimensions. Federal Agency for Technical Regulation and Metrology. Moscow: Standartinform; 2001. 37 p. (In Russ.)

² RD-25.160.10-KTH-001-12. Welding technology instruction for the construction and repair of steel vertical tanks of "Transneft" JSC. 112 p. URL: https://www.studmed.ru/rd-25-160-10-ktn-001-12-instrukciya-po-tehnologii-svarki-pri-stroitelstve-i-remonte-stalnyh-vertikalnyh-rezervuarov-chast-1_5cb8180807a.html (accessed: 10.10.2020). (In Russ.)

³ Gazprom Industry Standard 2-2.4-083-2006. Regulatory documents for the design, construction and operation of Gazprom facilities. Instructions on non-destructive methods of quality control of weld joints during the construction and repair of field and main gas pipelines. URL: <https://files.stroyinf.ru/Index2/1/4293831/4293831880.htm> (accessed: 10.10.2020). (In Russ.)

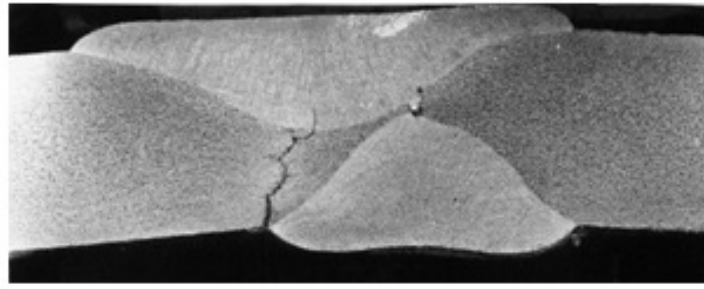


Fig. 2. Defects in the butt weld joint

III. Imperfection of the geometry of the weld cross-sections. The decrease in strength is mostly due to the sharpness of the interface between the base and the deposited metal (Fig. 2, 3): the smaller the transition radius r and the greater the angle of approach θ from the base to the deposited metal, the lower the fatigue strength of the weld joint. This pattern is valid even in the absence of welding defects.

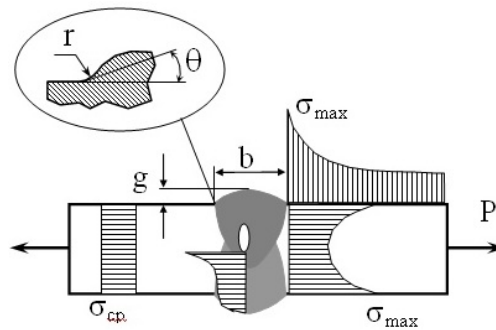


Fig. 3. Stress distribution in the interface zone of the base and deposited metal, at the apex of sharp defects

The weld joint design is determined by:

- the shape and dimensions of the butt edges of the parts;
- relative position, configuration, length of welds;
- type of weld joint according to GOST.

Fig. 4 shows the stress distribution in lap joints with flank and composite welds.

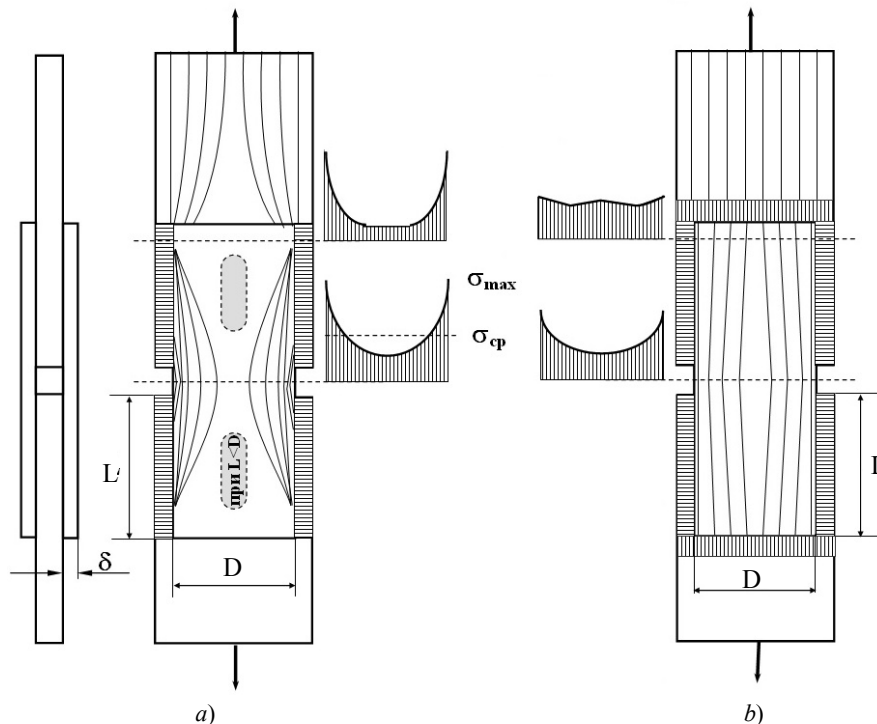


Fig. 4. Stress distribution in lap joints: a) with flank welds; b) with composite weld

Table 1 shows the values of the theoretical stress concentration coefficient K_H depending on the length and width of the tie plate:

$$K_H = \frac{6_{max}}{6_{cp}} = 6,6 \cdot \frac{D}{L} \cdot \text{cth} \left(4,6 \frac{D}{L} \right). \quad (1)$$

Table 1

K_H values depending on the length and width of the tie plate

D/L	0.2	1.0	2.0	4.0
K_H	1.45	2.01	3.37	6.61

IV. Residual welding stresses (RWS).

V. Absolute dimensions of the parts to be welded (scale factor).

Welded joints in metal structures, even without welding defects, usually contributes to a decrease in operational properties. Butt weld joints are the least dangerous in this sense. Lap joints and T-joints create a stress concentration caused by sharp changes in the working cross-sections [8, 9]. However, for the manufacture of many structures, butt joints are not enough.

Residual welding stresses can change the overall power flow distribution pattern. RWS, interacting and summing up with stresses from external loads, affect the performance of weld joints. This effect can also be positive, for example, if the vectors of RWS and stresses from external loads are multidirectional (tension + compression, etc.).

Welded joints have the greatest impact on the fatigue of structures. Disturbing factors (Fig. 1) cause destruction at stresses that can be transmitted by elements of metal structures without weld joints¹.

In numerous papers devoted to the impact of welding defects on the performance of joints, recommendations are given to reduce harmful effects. At the same time, it is noted that some defects should be classified as harmless. For example, single small pores practically do not affect the fatigue strength of weld joints. In this case, the regulations on the presence of pores are designed to provide not the strength, but the acceptable presentation of the product.

Traditionally, welding defects are understood as any imperfections in the geometry and discontinuities of the material of the welds and the heat-affected zone (HAZ). Thus, the geometry of the local interface zone of the base and deposited metals can also be considered a defect.

Materials and Methods. The study of the documents regulating the presence and size of welding defects has shown that they practically do not require the geometry of the sections of weld joints at the junction of the weld and the base metal. However, it is here that destruction occurs due to the formation and growth of crack-like defects [2, 4, 10]. When developing standards (for example, for main pipelines operating under static and re-static loads), it is important to consider not only the size of the defect that weakens the working section of the weld, but also its sharpness, which determines the local stress concentration at the defect mouth.

In [8], methods for predicting the stability of weld joints during fatigue work with account for the actual geometry of the welds and the probability of defects are presented. This approach is appropriate for the development of industry standards for the admissibility of welding defects considering the loading and responsibility of metal structures. These methods provide the determination of statistically valid characteristics of the weld joint quality.

In metal structures under static loads, defects in welds appear if their dimensions are so significant that they actually weaken the working cross-sections of the joints. To determine the strength of the joints and the acceptable dimensions of the defects, a static strength calculation for permissible stresses is performed.

It is advisable to approach the calculations of weld joints operating in the re-static load mode with crack-like defects, with regard to fracture mechanics. In this case, the stress intensity factor K_I [3, 10–12] is used:

$$K_I = \sigma \sqrt{\pi l}, \quad (2)$$

¹Harchenko VYa, Assaulenko SS, Peredelsky VA. On the requirements for the quality of weld joints and their classification in machine-building structures. In: Proc. VII Sci.-Pract. Conf. on Innovative technologies in mechanical engineering and metallurgy. Rostov-on-Don: DSTU Publ. Center; 2015. P. 341–346. (In Russ.)

where σ — nominal voltages; l — half-length of the equivalent crack describing a typical size of crack-like defects defect (e.g., the undercut depth, the depth of faulty penetration, etc.).

In this case, defects with a radius at the vertex R of less than 0.25 mm can be conventionally classified as crack-like defects. These are the defects for which $R > 0.25$ mm can be conventionally considered blunt.

Research Results. One of the factors that determine the operational properties of welded structures are crack-like defects, such as: faulty penetrations, undercuts, inter-roll incomplete fusions, microcracks.

During visual and measuring control, it is very difficult to detect sharp defects with small measured values (0.1-0.25 mm). This is due to the low sensitivity of the measuring instrument and the human factor since the measurements are performed using the controller in manual mode [13].

Radiography and ultrasound are the two main non-destructive physical testing methods for detecting internal defects. Under studying the particularly critical structures, these methods often duplicate each other since they have different sensitivity and reliability. To bring out sharp, undetectable defects (e.g., cracks), an ultrasound control¹ is preferred [14, 15]. However, it is often done manually. Accordingly, the results may be affected by the human factor, so this method is not sufficiently reliable.

Major challenge in assessing the product quality may arise for specialists already at the preparation stage, when choosing the method of ultrasonic testing (e.g., when using the mirror-shadow method, the echo technique, or the shadow method). To choose, you need to know the methods of operation, as well as to consider the characteristics of the converters in accordance with GOST R 55725-2013². Such knowledge is not always demonstrated even by third-level specialists, which is revealed during certification.

Equipment and quality control specialists should be able to correctly configure the flaw detector according to standard samples (SS-1, SS-2, SS-3) and according to the enterprise standard samples (ESS). Such templates are made of a material similar to the material of the object under control. The samples should correspond to the object in thickness and (if required) in radius (when checking small diameter pipes). However, the practice of conducting certification activities indicates that in some cases, specialists are not able to perform this work efficiently.

During the control process, the speed and step of scanning the object are also important. If the scanning speed is too high, the operator risks missing the defect or inaccurately determining its coordinates, the depth of occurrence and the boundaries of the discontinuity. The scanning speed standards are specified in the regulatory documentation. However, in the field, the control procedure is complicated by temperature difference, which depend on the time of year, venue, etc. For example, depending on the environment temperature, the temperature of the object under control changes, and this can affect the viscosity of the contact liquid. On the other hand, at low temperature, heating of the controlled area is required. This changes some of the physical properties of the object under control and, accordingly, the passage of ultrasound in the product, etc.

The main problem in summing up the results of the control and issuing conclusions is a free and subjective interpretation of the data obtained on the number of defects, depth and area of their occurrence. Much depends on the experience of the operator, his ability to distinguish the signals of defects from false or superficial ones.

Discussion and Conclusions. It is required to restrict the influence of the human factor to increase the reliability of the results of visual-measuring and ultrasonic quality control of weld joints. To achieve this goal, we consider it appropriate to organize additional training in the process of periodic mandatory assessment of the qualifications and certification of control specialists. Teachers should be experts of welding production. In short-term training programs, it is required to summarize information on the impact of sharp crack-like welding defects on the strength characteristics of welded structures and their operational life.

¹ GOST 55724–2013. Non-destructive testing. Welded joints. Ultrasonic methods. Federal Agency for Technical Regulation and Metrology. Moscow: Standartinform; 2019. 28 p. (In Russ.)

² GOST P 55725–2013. Non-destructive testing. Piezoelectric ultrasonic transducers. General technical requirements. Federal Agency for Technical Regulation and Metrology. Moscow: Standartinform; 2019. 16 p. (In Russ.)

During certification, it is required to use special simulators for ultrasonic testing and samples of weld joints of structural elements with artificially created defects that simulate their real size, shape and location in test samples. This will provide obtaining an objective assessment of the reliability and informativeness of ultrasound control.

References

1. Luk'yanov VF, Zhabin AN, Prilutskii AI. Normativnaya baza tekhnicheskogo regulirovaniya v svarochnom proizvodstve [Regulatory framework for technical regulation in welding production]. Rostov-on-Don: DSTU Publ. Centre; 2008. 302 p. (In Russ.)
2. Hesse A-C, Nitschke-Pagel T, Dilger K. On the effect of weld defects on the fatigue strength of beam welded butt joints. *Procedia Structural Integrity*. 2018;13:2053–2058.
3. Gorev VV, Uvarov BYu, Filippov VV, et al. Metallicheskie konstruksii. V 3 t. [Metal structures. In 3 vol.], 3rd ed., VV Gorev (ed.). Moscow: Vysshaya shkola; 2004. Vol.1. 551 p. (In Russ.)
4. Gumerov AG, Yamaleev KM, Zhuravlev GV, et al. Treshchinostoikost' metalla trub nefteprovodov [Fracture toughness of metal of pipes of oil pipelines]. Moscow: Nedra-Biznestsentr; 2001. 231 p. (In Russ.)
5. Gosavi PD, Sarkar KK, Khunte SK, et al. Microstructure and mechanical properties correlation of weld joints of a high strength naval grade steel. *Procedia Structural Integrity*. 2019;14:304–313.
6. Shen W, Qiu Y, Xu L, et al. Stress concentration effect of thin plate joints considering welding defects. *Ocean Engineering*. 2019;184:273–288.
7. Papatheocharis T, Sarvanis GC, Perdikaris PC, et al. Fatigue resistance of welded steel tubular X-joints. *Marine Structures*. 2020;74:102809.
8. Luk'yanov VF, Parkhomenko AA, Rogozin DV. Otsenka ustalostnoi prochnosti svarnykh soedinenii s uglovymi shvami na osnove analiza lokal'nogo napryazhennogo sostoyaniya [Evaluation of fatigue strength of weld joints with angular seams based on the analysis of the local stress state]. *Welding and Diagnostics*. 2010;6:16–19. (In Russ.)
9. Kurkin AS, Makarov EL. Metodika rascheta resursa svarnykh konstruksii s nalichiem defektov [Methods of calculating the service life of welded structures with defects]. *Welding and Diagnostics*. 2012;5:41–44. (In Russ.)
10. Hu Y, Yan R, Shen W, et al. A novel semi-analytical method for notch stress and fatigue strength analysis of tube-flange welded joints. *International Journal of Fatigue*. 2020;141:105860.
11. Poletaev YuV, Poletaev VYu, Rogozin DV. Vliyanie nadreza na sklonnost' svarnykh soedinenii k mezherennomu razrusheniyu [Notch effect on the liability of welded joints to intergranular fracture]. *Vestnik of DSTU*. 2015;3(82):28–34. (In Russ.)
12. Primož Štefane, Sameera Naib, Stijn Hertelé, et al. Effect of crack length on fracture toughness of welded joints with pronounced strength heterogeneity. *Procedia Structural Integrity*. 2018;13:1895–1900.
13. Shubochkin AE, Prilutsky MA, Susman GV, et al. O pogreshnosti izmereniya geometricheskikh parametrov svarnogo soedineniya s ispol'zovaniem shablonov [On the error of measuring the geometric parameters of the welded compound using templates]. *Welding and Diagnostics*. 2019;6:41–45. (In Russ.)
14. Aleshin NP, Chernyshev GG, eds. Svarka. Reza. Kontrol'. Spravochnik v 2 t. [Welding. Cutting. Control. Reference book in 2 vols.] Moscow: Mashinostroenie; 2004. 480 p. (In Russ.)
15. Albuquerque V, Silva C, Moura E, et al. Thermal aging effects on the microstructure of Nb-bearing nickel-based superalloy weld overlays using ultrasound techniques. *Materials & Design*. 2012;36:337–347.

Submitted 23.11.2020

Scheduled in the issue 09.01.2021

About the Authors:

Peredelsky, Viktor A., postgraduate student of the Machines and Welding Fabrication Automation Department, Don State Technical University (1, Gagarin sq., Rostov-on-Don, 344003, RF), ORCID: <https://orcid.org/0000-0002-3802-8776>, viktorperedelsky@rambler.ru.

Harchenko, Viktor Y., lecturer of the Machines and Welding Fabrication Automation Department, Don State Technical University (1, Gagarin sq., Rostov-on-Don, 344003, RF), Cand.Sci. (Eng.), associate professor, ORCID: <https://orcid.org/0000-0002-7349-9688>, rostov.naks@mail.ru.

Chernogorov, Anatoly L., lecturer of the Machines and Welding Fabrication Automation Department, Don State Technical University (1, Gagarin sq., Rostov-on-Don, 344003, RF), Cand.Sci. (Eng.), associate professor, ORCID: <https://orcid.org/0000-0001-6251-9906>, motors2007@bk.ru.

Tihonov, Sergey V., welding engineer, “Head Certification Center, Moscow Region, National Agency of Welding Control” LLC (bldg. 14, 5, 2-ya Baumanskaya ul., Moscow, 105005, RF), ORCID: <https://orcid.org/0000-0003-0681-6169>, Stihonov86@mail.ru

Claimed contributorship

V. A. Peredelsky: basic concept formulation; text preparation; formulation of conclusions. V. Ya. Harchenko: basic concept formulation; academic advising; analysis of source material; the text revision; correction of the conclusions. A. L. Chernogorov: performing calculations of the stress-strain state of welded joints; the text revision. S. V. Tihonov: formation of references; analysis of the research results.

All authors have read and approved the final manuscript.

INFORMATION TECHNOLOGY, COMPUTER SCIENCE, AND MANAGEMENT



UDC 519.72; 519.876.5

<https://doi.org/10.23947/2687-1653-2021-21-1-96-104>

On the modification of bit-flipping decoder of LDPC-codes

S. S. Gurskiy, N. S. Mogilevskaya

Southern Federal University (Rostov-on-Don, Russian Federation)



Introduction. In all types of digital communication, error control coding techniques are used. Many digital communication standards, such as Wi-Fi and 5G, use low density parity check (LDPC) codes. These codes are popular because they provide building encoders and decoders with low computational complexity. This work objective is to increase the error correcting capability of the well-known bit-flipping decoder (BF) of LDPC-codes. For this purpose, a modification of the decoder is built, which enables to dynamically control one of its main parameters whose choice affects significantly the quality of decoding.

Materials and Methods. The well-known bit-flipping decoder of binary LDPC-codes is considered. This decoder has several parameters that are not rigidly bound with the code parameters. The dependence of the decoding quality on the selection of the output parameters of the bit-flipping decoder was investigated through simulation modeling. It is shown that the decoding results in this case are significantly affected by the input parameter of the decoder — threshold T . A modification of the BF-decoder of binary LDPC-codes has been developed, in which it is proposed to set the threshold dynamically during the execution of the algorithm depending on the error rate. A comparative analysis of the error-correcting capability of decoders is carried out by the simulation modeling method.

Results. A lemma on the maximum value of the decoder threshold T is formulated and proved. Upper bounds for the number of operations are found for the original and modified decoders. A simulation model that implements a digital noise-immune communication channel has been built. In the model, the initial data is encoded with a given LDPC-code, then it is made noisy by additive uniformly distributed errors, and thereafter, it is decoded in turn by the bit-flipping algorithm with different threshold T parameters, as well as by a modified decoder. Based on the input and output data, the correction capacity of the decoders used is estimated. Experiments have shown that the error-correcting capability of the modified decoder in the range of the real error rate is higher than that of the original decoder, regardless of the selection of its parameters.

Discussion and Conclusions. The lemma, proved in the paper, sets the upper bound on the threshold value in the original decoder, which simplifies its adjustment. The developed modification of the decoder has a better error-correcting capability compared to the original decoder. Nevertheless, the complexity of the modification is slightly increased compared to the original algorithm. It has been pointed out that the decoding quality of a modified decoder develops with a decrease in the number of cycles in the Tanner graph and an increase in the length of the code.

Keywords: LDPC-codes, error-correcting capability, dynamic threshold, binary symmetric channel, experimental research.

For citation: S. S. Gurskiy, N. S. Mogilevskaya. On the modification of bit-flipping decoder of LDPC-codes. Advanced Engineering Research, 2021, vol. 21, no. 1, p. 96–104. <https://doi.org/10.23947/2687-1653-2021-21-1-96-104>

© Gurskiy S. S., Mogilevskaya N. S., 2021



Introduction. In 1963, in [1], R. Gallager first described a class of linear block codes whose check matrix contains a small number of nonzero elements. Such codes are commonly referred to as low-density parity check codes, or LDPC codes. For them, it is possible to build encoders and decoders with low computational complexity. Thus, when using LDPC codes, the data transfer rate is not significantly limited. Many modern studies are devoted to LDPC codes and their decoders [2-5]. LDPC codes are widely used in various digital communication standards, such as Wi-Fi, 5G, and optical communication [6, 7]. However, despite the popularity of these codes, some of the problems associated with them require research and solution. One of them is building new decoders and improving the existing ones.

This work objective is to increase the error-correcting capability of the well-known bit-flipping decoder of LDPC codes (hereinafter referred to as the BF decoder). To do this, a modification of the decoder is built, which enables to dynamically control one of its key parameters, whose selection affects significantly the quality of decoding.

Materials and Methods. The key parameters of binary LDPC codes are length N , dimension K and minimum code distance d . The information words $[N, K, d]$ of the C -code are vectors $\bar{m} = (m_1, m_2, \dots, m_K) \in F_2^K$, where F_2 is the Galois field of cardinality 2, and the codewords are vectors $\bar{c} = (c_1, c_2, \dots, c_N) \in F_2^N$ [8]. It is convenient to set the LDPC codes with the check $(N - K) \times N$ matrix H . Most of its elements are zero [1], so it is more convenient to store it not entirely, but storing only the positions of nonzero elements rowwise.

There are regular [9] and irregular [10] LDPC codes. In regular codes, all rows and columns of the check matrices contain a fixed number of single elements (k and j , respectively), otherwise the code is called irregular. For convenience, check matrices of regular LDPC codes will be called regular matrices, and irregular LDPC codes — irregular.

Regular LDPC codes have a number of advantages: easily evaluated code parameters, easy storage of matrices, low computational complexity of encoding and decoding algorithms, etc. In addition, regular code decoders correct errors evenly, unlike irregular ones, which correct errors in some parts of the codeword worse than in others. However, the problem of generating regular matrices with given properties is complex, and brute-force methods are often used to solve it.

To discuss the properties of the matrix H it is convenient to use the corresponding Tanner graph $G = (V, E)$, where E — a set of edges, and $V = S \cup R$ — a set of vertices, S — a set of rows of the matrix H , and R — a set of its columns [11]. Each nonzero element H_{ij} , standing in the i -th row and the j -th column, defines an edge connecting the i -th vertex of the set S and the j -th vertex of the set R . Fig. 1 shows an example of a regular check matrix 3×6 with parameters $k = 4$ and $j = 2$, and the corresponding Tanner graph.

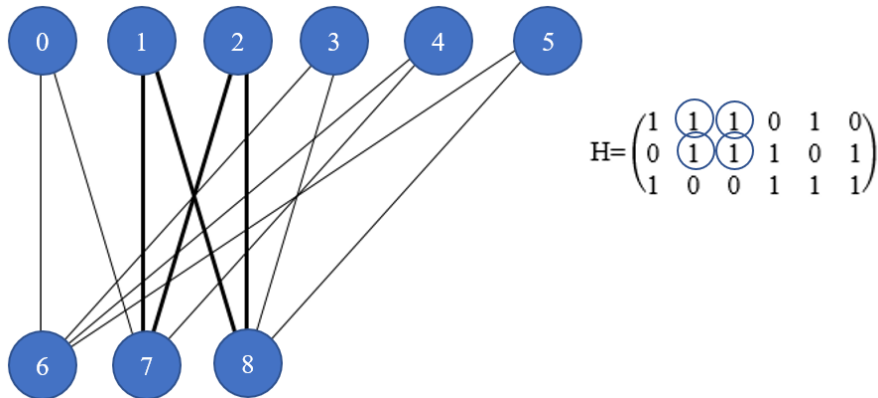


Fig. 1. The cycle in Tanner graph and in the check matrix

The top row of the graph vertices corresponds to the columns of the matrix H , and the bottom row is connected to the rows of H . An important characteristic of the check matrix H of the LDPC code is the presence and type of cycles in the corresponding Tanner graph. A cycle is a sequence of adjacent vertices of a graph in which the first and last vertices coincide. The length of this sequence is called the cycle length. The minimum cycle length in a graph is called the girth. If the graph contains no cycles, its girth is assumed to be infinite. An example of a cycle of length 4 is highlighted in bold lines in the graph (Fig. 1).

The error-correcting capabilities depend not only on the key parameters of the LDPC codes, but also on the structure of the check matrix H . On the one hand, the presence of cycles of small lengths (such as 4 and 6) impairs noticeably the error-correcting capability of the decoder [12]. On the other hand, the code that corresponds to Tanner graph without cycles does not correct errors, since its minimum code distance is 2. Thus, the task of constructing check matrices of regular LDPC codes is multiparametric. When solving it, you need to monitor the key parameters of the code, as well as the cycles in Tanner graph corresponding to the check matrix.

Consider the well-known BF-decoder of the LDPC code C in a convenient form [13].

Input: LDPC code C with parameters $[N, K, d]$, given by the check matrix

$$H = \begin{pmatrix} h_{11} & h_{12} & \dots & h_{1N} \\ h_{21} & h_{22} & \dots & h_{2N} \\ \dots & \dots & \ddots & \dots \\ h_{(N-K)1} & h_{(N-K)2} & \dots & h_{(N-K)N} \end{pmatrix}. \quad (1)$$

Vector $\bar{c}' = \bar{c} + \bar{e}$, $\bar{c} \in C (\subset F_2^N)$, $\bar{e} \in F_2^N$ — error vector; p — the number of iterations of the algorithm; T — threshold value.

Output: code vector $\bar{c} \in C (\subset F_2^N)$.

Step 1. Let the counter r be equal to zero.

Step 2. Calculate the syndrome $\bar{s} = \bar{c}' H^T$. If $\bar{s} = \bar{0}$ or $r = p$, then go to step 5.

Step 3. Select the unit coordinates from the vector $\bar{s} = (s_1, s_2, \dots, s_{N-K})$, i.e., $s_i = 1$, $i = \overline{1, (N-K)}$. Compose the set $L = \{i | s_i = 1\}$. Calculate $\bar{h}' = (h'_1, h'_2, \dots, h'_N)$, where

$$h'_l = \sum_{i \in L} h_{il}. \quad (2)$$

The values h_{il} , $l = 1, \dots, N$ should be assumed to be nonnegative integers. Thus, $\bar{h}' \in \mathbb{N}_0^N$, where $\mathbb{N}_0 = \mathbb{N} \cup \{0\}$.

Step 4. In the vector $\bar{h}' = (h'_1, h'_2, \dots, h'_N)$, we find all the elements $h'_i > T$. Among them, we select random h'_i and invert the bit c'_i of the vector \bar{c} . Add a unit to the counter r and go to step 2.

Step 5. $\bar{c} := \bar{c}'$.

The research carried out in this work allows us to make some observations on the BF-decoder.

Observation 1. The input parameter p sets the maximum number of iterations of the algorithm from the 2nd to the 4th steps, but the decoder can recover the codeword in fewer iterations.

Observation 2. When selecting the parameter T , the following considerations should be taken into account. If the parameter d of the used $[N, K, d]$ -code C is known, then it can be applied to calculate t — the number of reliably recoverable errors, and then the number of decoder iterations is limited to this value:

$$p = t = \left\lfloor \frac{d-1}{2} \right\rfloor. \quad (3)$$

Here, $\lfloor x \rfloor$ — rounding the number x to a smaller integer. If the parameter d is unknown, then it can be estimated using the Singleton bound [5]

$$d \leq N - K + 1$$

and, using (3), we obtain

$$p = \left\lfloor \frac{N-K}{2} \right\rfloor.$$

Observation 3. The structure of the decoder is such that the recovery of the correct codeword is not guaranteed, even if in the noisy word $\bar{c}' = \bar{c} + \bar{e}$, no more than t errors occurred (3).

Observation 4. In the literature, for regular check matrices in the BF decoder, it is recommended to select the threshold T depending on the weight j of the column of the matrix H , namely, $T = \frac{j}{2}$. For irregular matrices, such recommendations are not given in the literature. The error-correcting capability of the BF decoder can be worsened by an unsuccessful selection of threshold T . If its value is large, at step 4 of the decoder, the vector \bar{h}' may not have a coordinate that exceeds the threshold T , therefore, the erroneous bits will not be corrected. If you select a small value of T in step 4 of the BF decoder, several coordinates, whose value exceeds the threshold, may appear in the vector \bar{h}' . Among them, there may be coordinates that do not contain an error. Thus, the selection of the parameter T can significantly affect the decoding quality.

Research Results. We formulate and prove a lemma on the maximum possible value of the threshold T . Then we modify the BF decoder so that the threshold is set dynamically during the decoding process, and conduct a comparative analysis of the original and modified decoding algorithms.

Lemma. Let the binary $[N, K, d]$ -code C be given by the check matrix H having a fixed number of j unit elements in each column. Then the maximum threshold value T for the BF decoder of such LDPC code C cannot be greater than

$$T = j - 1. \quad (4)$$

Proof. Let the vector $\bar{c}' = \bar{c} + \bar{e}$ be obtained from the transmission channel, where $\bar{c} \in C$ — is the correct codeword, $\bar{e} \in F_2^N$ — the error vector with the Hamming weight $w(\bar{e})$. If $w(\bar{e}) = 0$, then, in step 2, the vector-syndrome $\bar{s} = \bar{0}$. Hence, the algorithm will go to step 5 and return \bar{c}' as the answer. In this case, the threshold value is not used. If $w(\bar{e}) > 0$, then the regularity of H implies the validity of the inequality $h'_i \leq j$, where h'_i — the elements of the vector \bar{h}' . The inverting of the bit c_i of the vector \bar{c}' occurs in the algorithm only if $h'_i > T$. Therefore,

$$T < h'_i \leq j.$$

Thus, the formula (4) is correct.

We will make changes to the BF decoder that will allow us to determine the threshold value dynamically, depending on the degree of damage to the code vector in the transmission channel.

Input: $[N, K, d]$ -code C given by the above check matrix (1). Vector $\bar{c}' = \bar{c} + \bar{e}$, where $\bar{c} \in C (\subset F_2^N)$, $\bar{e} \in F_2^N$ — the error vector; p — the number of iterations of the algorithm; T — some threshold value selected in advance.

Output: code vector $\bar{c} \in C (\subset F_2^N)$.

Step 1. Let the counter r be equal to zero.

Step 2. Calculate the syndrome $\bar{s} = \bar{c}' H^T$. If $\bar{s} = (0, \dots, 0)$ or $r = p$, then go to step 7.

Step 3. Select the unit coordinates from the vector $\bar{s} = (s_1, s_2, \dots, s_{N-K})$, i.e., $s_i = 1$, $i = \overline{1, (N-K)}$. Compose the set $L = \{i | s_i = 1\}$. Calculate $\bar{h}' = (h'_1, h'_2, \dots, h'_N)$, where h'_i is the same as in the original decoder (2). When summing the value h_{il} $l = 1, \dots, N$, we should assume nonnegative integers. Thus, $\bar{h}' \in \mathbb{N}_0^N$, где $\mathbb{N}_0 = \mathbb{N} \cup \{0\}$.

Step 4. Initialize the threshold value $T := \max(h'_i)_{i=1, \dots, N} - 1$.

Step 5. If $T \geq 0$

Select an arbitrary element h'_q of the vector \bar{h}' — such as $h'_q > T$.

Invert the bit c'_q .

Step 6. Add a unit to the counter r and go to step 2.

Step 7. $\bar{c} := \bar{c}'$.

Observation 5. The modified algorithm generally performs fewer iterations than the BF decoder since the threshold is selected dynamically in step 4. Therefore, the decoder does not perform useless iterations that do not change the bits of the vector \bar{c}' . The threshold value in the modified decoder depends on the number of errors that damaged the codeword, and is immediately set so that the noisy codeword \bar{c}' is guaranteed to be changed.

Let us estimate from above the number of addition, comparison and assignment operations in both decoders. In the original BF decoder of the $[N, K, d]$ -code C , $p(kK + (N - K)N + 1)$ addition operations, $p(3N - 2K + 2)$ comparison operations and $p((N - K)(k + 1) + 2N + 3) + 1$ assignment operations are performed. In the BF decoder with dynamic threshold, $p(kK + (N - K)N + 3)$ addition operations, $p(5N - 2K + 3)$ comparison operations and $p((N - K)(k + 1) + 2N + 4) + 1$ assignment operations are performed. Here, p — the decoder parameter that sets the maximum number of operations, k — weight of the code check matrix rows. Note that when implementing the algorithm, the multiplication and division operations are not actually used, as long as at the second step, it is convenient to use addition operations instead of multiplication to calculate the syndrome \bar{s} . Recall that the matrix H has a sparse structure, and its rows are conveniently stored as a list of nonzero element numbers. Therefore, instead of multiplying the vector \bar{c}' by the matrix H , it is required to sum the coordinates of the vector \bar{c}' , whose numbers coincide with the numbers of nonzero elements in the corresponding row of the matrix H .

Compared to the original algorithm, the modified BF decoder performs more operations, but moderately: the number of comparison operations has increased by $p(2N + 1)$, assignment operations — by p , addition operations — by $2p$.

For a comparative study of the error-correcting capability of the original and modified decoding algorithms, a software tool has been created that implements a simulation model of a binary symmetric perfectly synchronized noise-immune communication channel according to [14–16]. To provide noise immunity, the model uses LDPC codes and BF decoders (original and with dynamic threshold). Errors in the channel were modeled as independent and uniformly distributed.

The experiments used purposely found check matrices that specify LDPC codes. We describe the key parameters of these matrices using the standard notation of the key parameters of the code, as well as: j and k — the weight of each column and the weight of each row of the check matrix, respectively; ω_4, ω_6 — 4 and 6 cycles in Tanner graph corresponding to the check matrix.

Regular matrix H_1 : $N = 20, K = 5, j = 3, k = 4, d = 6, \omega_4 = 0, \omega_6 = 41$.

Regular matrix H_2 : $N = 28, K = 7, j = 3, k = 4, d = 6, \omega_4 = 0, \omega_6 = 42$.

Regular matrix H_3 : $N = 28, K = 7, j = 3, k = 4, d = 6, \omega_4 = 0, \omega_6 = 29$.

Irregular matrix H_4 : $N = 32, K = 5, j = 3, d = 12, \omega_4 = 0, \omega_6 = 0$.

Using these matrices, LDPC codes were constructed and simulation experiments were conducted. Fig. 2–5 show graphs of the dependence of the error-correcting capability of the constructed LDPC codes on the error probability in the channel. For the rationale for selecting the threshold values $T = 1$ and $T = 2$ in the BF decoder, see Observations 3, 4 and Lemma.

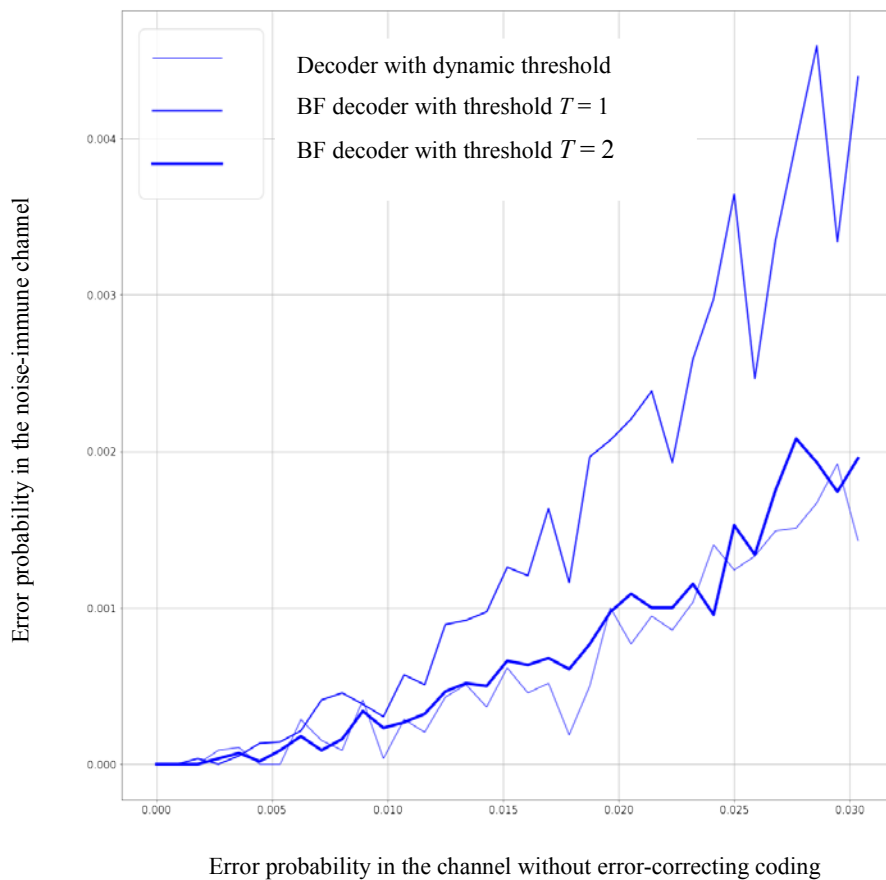


Fig. 2. Graph of the decoder error-correcting capability for LDPC codes given by the matrix H_2

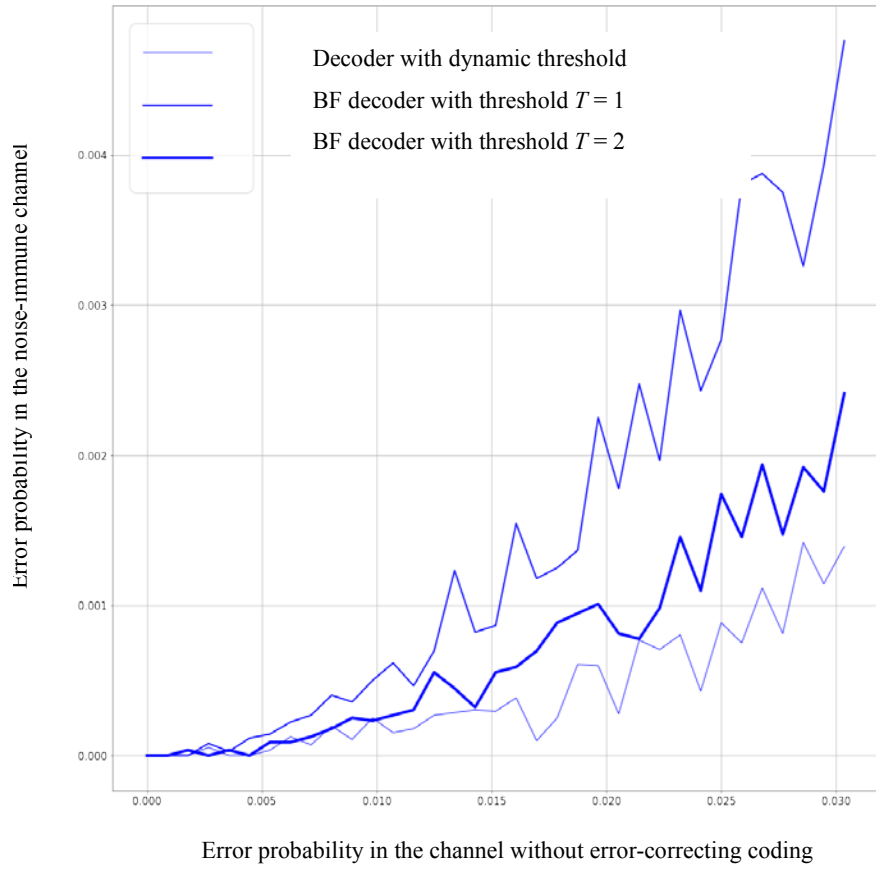


Fig. 3. Graph of the decoder error-correcting capability for LDPC codes given by the matrix H_3

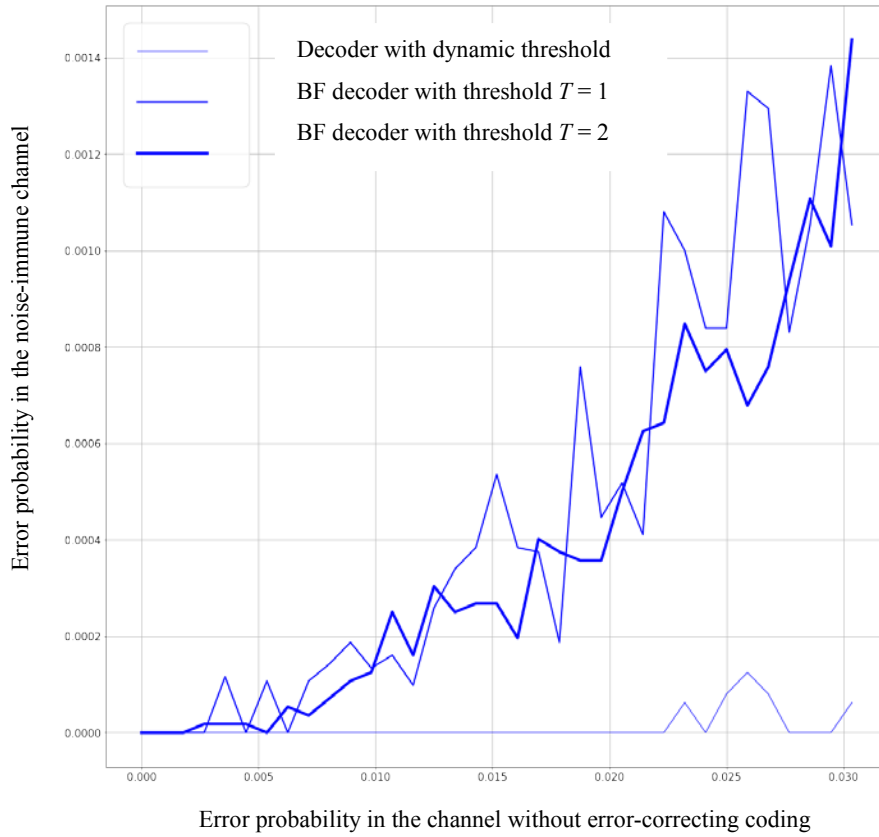


Fig. 4. Graph of the decoder error-correcting capability for LDPC codes given by the matrix H_4

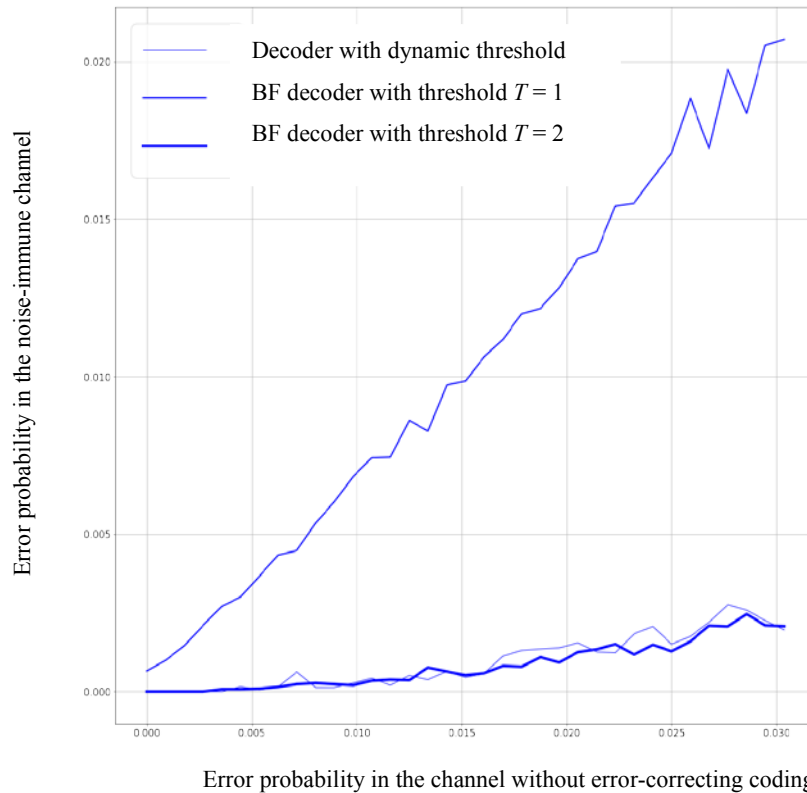


Fig. 5. Graph of the decoder error-correcting capability for LDPC codes given by the matrix H_1

In the range of the real error level [8, 13, 14] in Fig. 2–4, it can be observed that the BF decoder at the threshold value $T = 2$ shows better results than at $T = 1$, and the modified BF decoder has a better error-correcting capability compared to the original one.

The decoders show similar efficiency at small values of the code length, but when it is increased, the modified decoder shows better results. Specifically, if the error probability in the non-noise-immune channel is 0.05, the difference in the error probability in the noise-immune channel when using a BF decoder with the threshold $T = 2$ and $T = 1$, is from 0.005 to 0.03 in favor of using a larger threshold value. If a BF decoder with the threshold $T = 2$ and a modified decoder are used, this difference varies depending on the LDPC code in the range from 0.001 to 0.003. If the error probability in the non-noise-immune channel is 0.1, the error probability in the noise-immune channel when using a BF decoder with the threshold $T = 2$ is less than with the threshold $T = 1$ by the value from 0.001 to 0.02. When using a BF decoder with the threshold $T = 2$ and a modified decoder, this difference varies in the range from 0.002 to 0.01 depending on the LDPC code.

Both decoders are sensitive to the number of cycles in Tanner graph corresponding to the LDPC code check matrix. The greater the ratio of the number of cycles to the total number of elements in the matrix, the worse any BF decoder corrects errors. During the experiments, it was interesting to find out whether it is possible to increase the number of cycles in the matrix so that the modified decoder will show worse results compared to the BF decoder. Experimentally, the matrix H_1 containing 41 cycles of length 6 was found. The results of the study on the error-correcting capability of decoders for this matrix are shown in Fig. 5. Note, however, that the matrix H_2 contains even more cycles of length 6, namely, 42. The fundamental difference between the matrices H_1 and H_2 is in the density of units:

- in H_1 — 60 unit elements per 300 matrix elements,
- in H_2 — 84 units per 588 matrix elements.

Recall that the feature of LDPC codes is the sparse structure of the check matrix, so H_2 is more typical for LDPC codes.

Discussion and Conclusions. The paper considers a bit-flipping decoder for binary LDPC codes. Recommendations on the selection of such input parameters of the decoder as the threshold and the number of iterations

of the algorithm are given. A lemma on the maximum value of the decoder threshold is formulated and proved. A modification of the BF decoder of binary LDPC codes has been developed, in which it is proposed to set the threshold dynamically during the execution of the algorithm depending on the resulting syndrome. For the original and modified decoders, upper estimates of the number of operations are found. These estimates show that the modification complicates the decoder only slightly. The conducted simulation experiments demonstrate better error-correcting capability of the modified decoder in relation to the original one. The experiments also showed the dependence of the decoding quality on the degree of matrix sparsity and the number of cycles of length 6 in the Tanner graph corresponding to the check matrix of the LDPC code. Thus, the problem of constructing check matrices with a small number of short cycles arises, which is the subject of further research.

References

1. Gallager R. Low-density parity-check codes. IRE Transactions on information theory. 1962;1:21–28.
2. Milicevic M, Feng Ch, Zhang LM, et al. Quasi-cyclic multi-edge LDPC codes for long-distance quantum cryptography. NPJ Quantum Information. 2018;4(1):1–9. DOI: 10.1038/s41534-018-0070-6
3. Chen P, Cai K, Zheng S. Rate-Adaptive Protograph LDPC Codes for Multi-Level-Cell NAND Flash Memory. IEEE Communications Letters. 2018;22(6):1112–1115. DOI: 10.1109/LCOMM.2018.2814985
4. Baldi M, Barengi A, Chiaraluce F, et al. A Post-quantum Key Encapsulation Mechanism Based on QC-LDPC Codes. Post-Quantum Cryptography. In: PQCrypto 2018: Lecture Notes in Computer Science. Cham: Springer. 2018;10786:3–24. DOI: 10.1007/978-3-319-79063-3_1
5. Maity RK, Singh RA, Mazumdar A. Robust Gradient Descent via Moment Encoding and LDPC Codes. In: IEEE International Symposium on Information Theory (ISIT). Paris: IEEE; 2019. P. 2734–2738. DOI: 10.1109/ISIT.2019.8849514
6. Li H, Bai B, Mu X, et al. Algebra-Assisted Construction of Quasi-Cyclic LDPC Codes for 5G New Radio. IEEE Access. 2018;6:50229–50244. DOI: 10.1109/ACCESS.2018.2868963
7. Cai Z, Hao J, Tan PH, et al. Efficient encoding of IEEE 802.11n LDPC codes. Electronics Letters. 2006;42(25):1471–1472.
8. Kolesnik VD. Kodirovanie pri peredache i khranении informatsii. [Coding in the transmission and storage of information]. Moscow: Vysshaya shkola; 2009. 550 p. (In Russ.)
9. Tong Zhang, Parhi KK. Joint (3,k)-regular LDPC code and decoder/encoder design. IEEE Transactions on Signal Processing. 2004;52(4):1065–1079. DOI: 10.1109/TSP.2004.823508
10. Yang M, Ryan WE, Yan Li. Design of efficiently encodable moderate-length high-rate irregular LDPC codes. IEEE Transactions on Communications. 2004;52(4):564–571.
11. Malema GA. Low-Density Parity-Check Codes: Construction and Implementation. University of Adelaide; 2007. 160 p. Available from: URL: <https://digital.library.adelaide.edu.au/dspace/bitstream/2440/45525/8/02whole.pdf> (accessed: 07.06.2020).
12. Etzion T, Trachtenberg A, Vardy A. Which Codes Have Cycle-Free Tanner Graphs? IEEE Transactions on Information Theory. 2006;52(9):4219–4223. DOI: 10.1109/TIT.2006.880060
13. Morelos-Zaragoza R. Iskusstvo pomekhoustoichivogo kodirovaniya. Metody, algoritmy, primeneniye [The art of noise-immune coding. Methods, algorithms, and applications]. Moscow: Tekhnosfera; 2006. P. 259–262. (In Russ.)
14. Deundiyak VM, Mogilevskaya NS. Metody otsenki primenimosti pomekhoustoichivogo kodirovaniya v kanalah svyazi [Methods for evaluating the applicability of noise-immune coding in communication channels]. Rostov-on-Don: DSTU Publ. Centre; 2007. 85 p. (In Russ.)
15. Deundiyak VM, Zhdanova MA, Mogilevskaya NS. Reshenie zadachi podbora modeli istochnika oshibok v IS OPSAPK [Solution to error source model selection problem in IS EASECC]. Vestnik of DSTU. 2017;17(4):107–115. DOI: 10.23947/1992-5980-2017-17-4-107-115 (In Russ.)

16. Deundyak VM, Mogilevskaya NS. Imitatsionnaya model' tsifrovogo kanala peredachi dannykh i algebraicheskie metody pomekhoustoichivogo kodirovaniya [The simulation model of digital channel of data transmission and algebraic methods of error-correcting coding]. Vestnik of DSTU. 2001;1(1):98–104. (In Russ.)

Submitted 26.10.2020

Scheduled in the issue 25.01.2021

About the Authors:

Gurskiy, Semen S., undergraduate student of the Algebra and Discrete Mathematics Department, Southern Federal University (8a, Milchakova St., Rostov-on-Don, 344090, RF), ORCID: <https://orcid.org/0000-0002-4738-2363>, nor-ber@list.ru

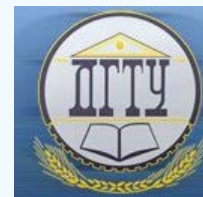
Mogilevskaya, Nadezhda S., associative professor of the Algebra and Discrete Mathematics Department, Southern Federal University (8a, Milchakova St., Rostov-on-Don, 344090, RF), Cand.Sci. (Eng.), associate professor, ORCID: <http://orcid.org/0000-0003-1357-5869>, nadezhda.mogilevskaia@yandex.ru

Claimed contributorship

S. S. Gurskiy: modification of the bit-flipping decoder; software implementation of channel models; conducting computational experiments; text preparation. N. S. Mogilevskaya: academic advising; task formulation; analysis of the research results; the text revision; formulation of conclusions.

All authors have read and approved the final manuscript.

INFORMATION TECHNOLOGY, COMPUTER SCIENCE, AND MANAGEMENT



УДК 621.396.6

<https://doi.org/10.23947/2687-1653-2021-21-1-105-110>

Method for estimating time length using simultaneous phase measurements in the system of simultaneously and independently operating generators

D. D. Gabrielyan¹, A. A. Kostoglotov², O. A. Safaryan², L. V. Cherkesova², O. V. Dvornikov³

¹ Rostov Research Institute for Radio Communication (Rostov-on-Don, Russian Federation)

² Don State Technical University (Rostov-on-Don, Russian Federation)

³ Minsk Research Instrument-Making Institute JSC (Minsk, Republic of Belarus)



Introduction. This paper is devoted to the development of a method for estimating the current time-frequency parameters of each of a set of simultaneously and independently operating generators in the radio electronic system. A general case is considered, in which the deviation of true values of the nominal generator parameters from the assumed values of these parameters is determined not only by random, but also by long-term frequency deviation. The work objective is to generalize the method for estimating the time-frequency parameters of signals (long-term nominal frequency and current frequency deviation from the nominal value) based on the simultaneous measurement of the phases of signals generated in the system of independently functioning generators. The research task is to consider a system of simultaneously and independently operating generators. Each of them generates harmonic signals, whose time-frequency parameters, such as the average frequency, are constant during a certain interval of observation. But herewith, these time-frequency parameters are known with insufficient accuracy due to the influence of external factors (changes in temperature, pressure, supply voltage, etc.). It is required to obtain estimates of the time-frequency parameters of signals (the duration of the measuring interval, values of the long-term frequency and the standard deviation) from the results of measurements of the phases of signals formed by the generators at measuring intervals belonging to the observation interval, within which the average frequency remains constant.

Materials and Methods. A system of simultaneously and independently functioning generators is considered. The long-term value of signal frequency for each of the generators over the observation interval remains constant, but it is known with some margin of error. During the observation interval, several measurements of the signal phase of each of the generators are performed. At the same time, the current values of the signal frequency and the duration of the measuring interval have random deviations from the long-term values, and follow the normal distribution law with zero mathematical expectation and a known variance. The estimation of time-frequency parameters based on the results of measuring the signal phases is carried out using a multidimensional likelihood function. The maximum is found on the base of solving the redefined system of linear algebraic equations.

Results. A new mathematical model and a numerical-analytical method for determining the time-frequency parameters of signals are developed. They take into account both the long-term constant frequency deviation and short-term random deviations.

Discussion and Conclusions. The results obtained can be used under the development and creation of data-measuring and information-telecommunication systems, including geographically distributed systems. The resulting estimates of the time-frequency parameters enable to increase the signal frequency stability and, accordingly, to improve the accuracy of measurements and the quality of information transfer.

Keywords: high-frequency generators, high frequency radio signals, statistical frequency stabilization method, frequency stability, least square method (LS method).

For citation: D. D. Gabrielyan, A. A. Kostoglotov, O. A. Safaryan, et al. Method for estimating a time length using simultaneous phase measurements in the system of simultaneously and independently operating generators. Advanced Engineering Research, 2021, vol. 21, no. 1, p. 105–110. <https://doi.org/10.23947/2687-1653-2021-21-1-105-110>

Funding information: the research is done with the financial support from RFFI (grant no. 19–01–00151/21).

© Gabrielyan D. D., Kostoglotov A. A., Safaryan O. A., Cherkesova L. V., Dvornikov O. V., 2021



Introduction. The constant growth of requirements for audio and video information transmission, for data formation and transmission systems, necessitates an increase in stability of the time-frequency parameters of signals generating in radio-electronic systems (RES) [1]. The information-telecommunication systems and data-measuring ones are typical examples of such systems. One of the components in providing high efficiency of such systems is associated with the formation of signals with highly stable time-frequency parameters. The latter is relevant, in particular, for the systems of information transmission with complex signals, radar and radio navigation systems, and audio and video information transmission systems as well.

Currently, the main approach in the creation of RES is a modular construction principle, which determines the use of functionally completed blocks and devices connected to each other. The application of this approach leads to presence of a large number of high-frequency signal (HF signal) generators in any radio-electronic system. At the same time, functional completeness of each of the devices included in the system enables to consider the HF-signal generators of these devices as units operating simultaneously and independently on a certain time interval.

Despite the fact that signal generators in various devices have different parameters, the presence of a large number of simultaneously and independently functioning generators in the RES provides determining the current values of the time-frequency parameters of these signals through measuring and subsequent processing of the generated signals phases¹ [2–6]. The latter makes it possible to estimate the current values of the time-frequency parameters with higher accuracy. In turn, the obtained values of the time-frequency signal parameters are associated with the parameters of the generators that are forming them. That allows either to stabilize the generators frequency, or to consider its current value during the subsequent signal processing [2–6].

Well-known solutions to the problem of estimating the current time-frequency parameters take into account, as a rule, only random components of the frequency deviation due to the influence of various factors. In this case, the values of such parameter as the nominal (mean) frequency of the generator are considered known. At the same time, in many cases, long-term frequency deviations associated with both the influence of external factors and the technology of generator production are not analyzed in the papers under examination.

Thus, the solution to the problem of estimating the time-frequency parameters of signals, such as the nominal (mean) frequency and random deviations from the average frequency of generators, is a challenge.

The paper objective is the generalization of the method of estimating the time-frequency signal parameters (the long-term nominal frequency and the current frequency deviation from the nominal value) based on the simultaneous measurement of the signal phases forming in the system of independently functioning generators.

As in the paper [3], let us consider the system of $N+1$ generators, each of which forms the harmonic signals, whose time-frequency parameters, such as average frequency ω_n , are constant, but known with insufficient accuracy due to the influence of external factors (changes in temperature, pressure, supply voltage, etc.) during a certain observation interval.

It is required to obtain estimates of the time-frequency parameters of signals (the duration of the measuring interval, frequency values and RMS (root-mean-square, or standard, deviation) of signals) from the results of measurements of the phases of the signals formed by the generators at the measuring intervals belonging to the observation interval, within which the average frequency values remain constant.

Mathematical model and solution method. For the system of $N+1$ generators under consideration, let us present the signals formed by each of the generators, as

$$s_n(t) = A_n \cos(\omega_n \cdot t + \varphi_n), \quad n = 1, \dots, N+1. \quad (1)$$

Using one of the generators (hereinafter the $N+1$ generator), we will form measuring intervals of nominal duration $t_m^{(0)}$ ($m = 1, \dots, M$), such that during all the specified intervals, the average frequency and RMS of the frequency of each of the generators can be considered constant.

We represent the measured values of signals phase $\Phi_{n,m}$ of each of N generators ($n = 1, \dots, N$) on the m -th measuring interval ($m = 1, \dots, M$) as follows:

$$\Phi_{n,m} = (\omega_n + \Delta\omega_{n,m})(t_m^{(0)} + \Delta t_m), \quad n = 1, \dots, N, \quad m = 1, \dots, M, \quad (2)$$

where $\Delta\omega_{n,m}$ – is random deviation of the n -th generator frequency on the m -th measuring interval from the average value ω_n ; $t_m^{(0)}$ and Δt_m are, respectively, nominal duration and deviation from the nominal value of the m -th measuring interval duration.

For the mean value frequency, taking into account the modern production technology of HF-generators, we can write

$$\omega_n = \omega_n^{(0)} + \delta\omega_n, \quad \delta\omega_n \ll \omega_n^{(0)}, \quad n = 1, \dots, N+1, \quad (3)$$

where the values $\omega_n^{(0)}$ are known, and $\delta\omega_n$, with account for the influence of external factors, are unknown.

Taking into account the expressions (3), the relation (2) takes the form

$$\Phi_{n,m} = (\omega_n^{(0)} + \delta\omega_n + \Delta\omega_{n,m})(t_m^{(0)} + \Delta t_m), \quad n = 1, \dots, N, \quad m = 1, \dots, M. \quad (4)$$

After linearization (the terms $\delta\omega_n \cdot \Delta t_m$ and $\Delta\omega_{n,m} \cdot \Delta t_m$, are discarded), the expression (4) enables to estimate the random deviation of the frequency of the n -th generator on the m -th measurement interval as follows:

$$\Delta\omega_{n,m} = \frac{\Phi_{n,m} - \Phi_{n,m}^{(0)} - \delta\omega_n \cdot t_m^{(0)} - \omega_n^{(0)} \cdot \Delta t_m}{t_m^{(0)}}, \quad n = 1, \dots, N, \quad m = 1, \dots, M, \quad (5)$$

where $\Phi_{n,m}^{(0)} = \omega_n^{(0)} \cdot t_m^{(0)}$.

The frequency deviations $\Delta\omega_{n,m}$ ($n = 1, \dots, N, m = 1, \dots, M$) and deviations of measurement interval duration Δt_m ($m = 1, \dots, M$) follow the normal distribution law [7]:

$$p(\Delta\omega_{n,m}) = \frac{1}{\sqrt{2\pi}\sigma_n^{(0)}} \exp\left[-\frac{(\Delta\omega_{n,m})^2}{2(\sigma_n^{(0)} \cdot \omega_n^{(0)})^2}\right], \quad p(\Delta t_m) = \frac{1}{\sqrt{2\pi}\sigma_{N+1}^{(0)}} \exp\left[-\frac{(\Delta t_m)^2}{2(\sigma_{N+1}^{(0)} \cdot t_m^{(0)})^2}\right], \quad (6)$$

where $\sigma_n^{(0)}$ are known values of the relative instability of the frequency of the n -th generator ($n = 1, \dots, N$).

The given relations describe the mathematical model of the system of generators that function simultaneously and independently.

Solution method. Taking into account the relations (5) and (6), we can write the multidimensional logarithmic likelihood function:

$$L(\delta\omega, \Delta t) = -\sum_{m=1}^M \sum_{n=1}^N \left\{ \ln \sqrt{2\pi} + \ln \sigma_n + \frac{(\Phi_{n,m} - \Phi_{n,m}^{(0)} - \delta\omega_n \cdot t_m^{(0)} - \omega_n^{(0)} \cdot \Delta t_m)^2}{2(\sigma_n^{(0)} \cdot \omega_n^{(0)} \cdot t_m^{(0)})^2} \right\}, \quad (7)$$

which includes the vectors $\delta\omega$ and Δt , whose elements are unknown values, respectively, $\delta\omega_n$ ($n = 1, \dots, N$) and Δt_m ($m = 1, \dots, M$).

The estimates $\delta\omega_n$ and Δt_m are found from the maximum condition (7) and correspond to the solution of the system of linear algebraic equations (SLAE).

$$\begin{cases} \frac{\partial L(\delta\omega, \Delta t)}{\partial \delta\omega_n} = 0, & n = 1, \dots, N, \\ \frac{\partial L(\delta\omega, \Delta t)}{\partial \Delta t_m} = 0, & m = 1, \dots, M. \end{cases} \quad (8)$$

The equations in (8) have the form

$$\begin{aligned} \frac{(\Phi_{n,m} - \Phi_{n,m}^{(0)} - \delta\omega_n \cdot t_m^{(0)} - \omega_n^{(0)} \cdot \Delta t_m) \cdot t_m^{(0)}}{(\sigma_n^{(0)} \cdot \omega_n^{(0)} \cdot t_m^{(0)})^2} &= 0, \quad n = 1, \dots, N, \\ \frac{(\Phi_{n,m} - \Phi_{n,m}^{(0)} - \delta\omega_n \cdot t_m^{(0)} - \omega_n^{(0)} \cdot \Delta t_m) \cdot \omega_n^{(0)}}{(\sigma_n^{(0)} \cdot \omega_n^{(0)} \cdot t_m^{(0)})^2} &= 0, \quad m = 1, \dots, M. \end{aligned} \quad (9)$$

In a matrix form, the SLAE (9) can be presented as:

$$\begin{pmatrix} A_{1,1} & A_{1,2} \\ A_{2,1} & A_{2,2} \end{pmatrix} \begin{pmatrix} \delta\omega \\ \Delta t \end{pmatrix} = \begin{pmatrix} B_1 \\ B_2 \end{pmatrix}, \quad (10)$$

where $A_{1,1}$ is the block with dimensions $N \cdot M \times N$ with elements $a_{n,m}^{(1,1)} = (\sigma_n^{(0)} \cdot \omega_n^{(0)})^{-2}$; $A_{1,2}$ is the block with dimensions $N \cdot M \times M$ with elements $a_{n,m}^{(1,2)} = (\sigma_n^{(0)})^{-2} \cdot (\omega_n^{(0)} \cdot t_m^{(0)})^{-1}$;

$A_{2,1}$ is the block with dimensions $N \cdot M \times N$ with elements $a_{n,m}^{(2,1)} = (a_{n,m}^{(1,2)})^T$;

$A_{2,2}$ is the block with dimensions $N \cdot M \times M$ with elements $a_{n,m}^{(2,2)} = (\sigma_n^{(0)} \cdot t_m^{(0)})^{-2}$;

B_1 is the block with dimensions $N \cdot M \times 1$ with elements $b_{n,m}^{(1)} = \frac{\Phi_{n,m} - \Phi_{n,m}^{(0)}}{(\sigma_n^{(0)} \cdot \omega_n^{(0)})^2 \cdot t_m^{(0)}}$;

B_2 is the block with dimensions $N \cdot M \times 1$ with elements $b_{n,m}^{(2)} = \frac{\Phi_{n,m} - \Phi_{n,m}^{(0)}}{(\sigma_n^{(0)} \cdot t_m^{(0)})^2 \cdot \omega_n^{(0)}}$;

T is the sign of the matrix transposition.

The system of equations (9) contains N of the unknown components $\delta\omega_n$ and M of the unknown elements Δt_m . The total number of measured values of signal phase is $N \cdot M$. The estimation of their values, taking into account the measurement errors, should be carried out by the least-square method (LSM) [8-10]. In this case, the condition $N \cdot M > N + M$ must be met, and the number of measurement intervals must satisfy the next condition: the number of measurements M must fulfil the condition $M > N/(N-1)$.

The representation of SLAE using the expressions (9) and (10) defines the numerical-analytical method for the problem solving. All elements of the matrix have an analytical representation. At the same time, when passing to the system of normal equations, as a rule, used in the LSM, obtaining the analytical expressions is also not difficult. However, the inversion of large-dimensional matrix can be performed only using the numerical methods [11–13].

The estimates $(\delta\omega_n)^*$ and $(\Delta t_m)^*$ obtained from the solution to the system of equations, represented by the expressions (9), allow us to determine current time-frequency parameters of the generators and signals forming by them.

Research Results. We propose a mathematical model describing a simultaneous and independent functioning of the generator system, and a numerical-analytical method for determining the time-frequency parameters of the signals with account for both the long-term constant frequency deviation and the short-term deviation of random nature. This approach enables:

- to evaluate, according to the results of measuring the phases of signals formed by simultaneously and independently functioning generators, not only random deviations in the frequency of the generated signals, and to obtain the estimates of the average long-term frequency of each of the generators;
- to exclude an instability influence of the time interval duration of measurements on the resulting estimates of the signal time-frequency parameters [14-16].

Discussion and Conclusions. The results obtained can be used under the development and creation of data-measuring and information-telecommunication systems, including the geographically distributed systems. The resulting estimates of the time-frequency parameters provide increasing the signal frequency stability and, accordingly, improving the accuracy of the measurements and the quality of information transmission.

References

1. Vasilyev AF, Merkulov EA. Programmiruemyi tsifrovoy preselektor dlya sistem radiosvyazi dvoynogo naznacheniya [Programmable digital preselector for dual-purpose radio communication systems]. Vestnik of DSTU. 2012;12(2-1):5–11. (In Russ.)
2. Gabriel'yan DD, Prygunov AA, Prygunov AG, et al. Metod otsenki chastot v sisteme generatorov [Method of estimating frequency generator system]. Physical Bases of Instrumentation 2012;1(2):72–77. (In Russ.)
3. Gabriel'yan DD, Safaryan OA. Proyavlenie svoystva ehmerzhenosti v sisteme nezavisimo funktsioniruyushchikh generatorov pri ispol'zovanii metoda statisticheskoi stabilizatsii chastoty [The emergence property in a system of independently functioning generators using the method of statistical frequency stabilization]. Journal of Radio Electronics. 2019, no. 8. Available from: <http://jre.cplire.ru/jre/aug19/2/text.pdf>. DOI 10.30898/1684-1719.2019.8.2 (In Russ.)

4. Gabriel'yan DD, Safaryan OA. Obobshchennyi metod statisticheskogo otsenivaniya chastoty odnovremenno i nezavisimo funktsioniruyushchikh generatorov [Generalized method for statistical estimation of frequency of simultaneously and independently functioning generators]. Journal of Radio Electronics. 2020, no. 5. Available from: <http://jre.cplire.ru/jre/may20/5/text.pdf>. DOI 10.30898/1684-1719.2020.5.5 (In Russ.)
5. Safaryan OA. Modelirovanie protsessa stabilizatsii chastoty generatorov v infokommunikatsionnykh sistemakh [Simulation of generator frequency stabilization in infocommunication systems]. Vestnik of DSTU. 2016;16(4):150–154. (In Russ.)
6. Safaryan OA, Sakharov IA, Boldyrikhin NV, et al. Method of Reducing Phase Noise in the System Simultaneously and Independently Operating the High-Frequency Signal Generators. Engineering Computations. Emerald Group Publishing Ltd. 2017;34(8):2586–2594.
7. Korn G, Korn T. Spravochnik po matematike dlya nauchnykh rabotnikov i inzhenerov [Handbook of Mathematics for researchers and engineers]. Moscow: Nauka; 1974. 832 p. (In Russ.)
8. Mazmishvili AI. Teoriya oshibok i metod naimen'shikh kvadratov [Error theory and the least squares method]. Moscow: Nedra; 1978. 310 p. (In Russ.)
9. Neydorf RA. Approksimatsionnoe postroenie matematicheskikh modelei po tochechnym ehksperimental'nym dannym metodom «cut-glue» [Approximating mathematical model development according to point experimental data through “cut-glue” method]. Vestnik of DSTU. 2014;14(1):45–59. (In Russ.)
10. Kostoglotov AA, Deryabkin IV, Lazarenko SV, et al. Synthesis of Phase-Locked Loop System Structure with Adaptation Based on Combined-Maximum Principle. MATEC Web of Conferences “2016 3rd International Conference on Mechanics and Mechatronics Research, ICMR 2016”. 2016;77:15002. DOI: <https://doi.org/10.1051/mateconf/20167715002>
11. Demir A, Mehrotra A, Roychowdhury J. Phase noise in oscillators: A unifying theory and numerical methods for characterization. IEEE Trans. Circuits Syst. I. Fundam. Theory Appl. 2000;47(5):655–674.
12. Hati A, Nelson C, Howe DA. Reducing oscillators PM noise from AM-PM correlation. Electronics Letters. 2014;50(17):1195–1197. DOI: 10.1049/el.2014.2210
13. Huang X, Jiao J, Sun F, et al. Prediction, simulation, and verification of the phase noise in 80-MHZ low-phase-noise crystal oscillators. Proc. IEEE Transactions on Ultrasonics, Ferroelectrics, and Frequency Control. 2015;62(9):1599–1604.
14. Cheng Lei, Hongwei Chen, Minghua Chen, et al. Recirculating Frequency Shifting Based Wideband Optical Frequency Comb Generation by Phase Coherence Control. IEEE Photonics Journal. 2015;7(1):1300107.
15. Wei Chen, Qin Liu, Nan Cheng, et al. Joint Time and Frequency Dissemination Network Over Delay-Stabilized Fiber Optic Links. IEEE Photonics Journal. 2015;7(3):7901609.
16. Shu Sun, Rappaport TS, Thomas TA, et al. Investigation of Prediction Accuracy, Sensitivity and Parameter Stability of Large-Scale Propagation Path Loss Models for 5G Wireless Communications. IEEE Transactions on Vehicular Technology. 2016;65(5):2843–2860.

Submitted 14.12.2020

Scheduled in the issue 25.02.2021

About the Authors:

Gabrieli'yan, Dmitriy D., Deputy Head, Rostov Research Institute for Radio Communication (130, Nansena St., Rostov-on-Don, 344038, RF), Dr.Sci. (Eng.), professor, ScopusID: [7004903129](https://orcid.org/0000-0003-4006-2436), d.gabrieljan2011@yandex.ru

Kostoglotov, Andrey A., professor of the Cybersecurity of IT Systems Department, Don State Technical University (1, Gagarin sq., Rostov-on-Don, 344003, RF), Dr.Sci. (Eng.), professor, ResearcherID: [A-5161-2014](https://orcid.org/0000-0002-7508-913X), ScopusID: [6701522218](https://orcid.org/0000-0002-7508-913X), ORCID: <https://orcid.org/0000-0002-7508-913X>, kostoglotov@me.com

Safaryan, Olga A., associate professor of the Cybersecurity of IT Systems Department, Don State Technical University (1, Gagarin sq., Rostov-on-Don, 344003, RF), Cand.Sci. (Eng.), associate professor, ScopusID: [57210832767](https://orcid.org/0000-0002-7508-913X), ORCID: <https://orcid.org/0000-0002-7508-913X>, safari_2006@mail.ru

Cherckesova, Larissa V., professor of the Cybersecurity of IT Systems Department, Don State Technical University (1, Gagarin sq., Rostov-on-Don, 344003, RF), Dr.Sci. (Phys.-Math.), associate professor, ScopusID: [54683534500](https://orcid.org/54683534500), ORCID: chia2002@inbox.ru

Dvornikov, Oleg V., Chief Researcher, Minsk Research Instrument-Making Institute JSC (5-1, 2nd Paveletsky Pr., Moscow, 115114, RF), Dr.Sci. (Eng.), professor, oleg_dvornikov@tut.by

Claimed contributorship:

D. D. Gabrielyan: basic concept formulation; academic advising. A. A. Kostoglotov: research objectives and tasks setting; computational analysis. O. A. Safaryan: the text revision; correction of the conclusions. L. V. Cherckesova: text preparation; formulation of conclusions. O. V. Dvornikov: analysis of the research results.

All authors have read and approved the final manuscript.